Spreading of viscous fluids and granular materials on slopes

Daisuke Takagi

King's College

A dissertation submitted to the University of Cambridge
for the degree of Doctor of Philosophy

June 2010

Declaration of Originality

This dissertation is my own work and contains nothing which is the outcome of work done in collaboration with others, except as specified in the text and Acknowledgements.

The dissertation is based on research conducted from October 2007 to June 2010. I was supervised by Professor Herbert Huppert FRS and Dr. Jim McElwaine as a research student at the Department of Applied Mathematics and Theoretical Physics, University of Cambridge. During the summer of 2009, research was carried out under the supervision of Professor Neil Balmforth as part of the Geophysical Fluid Dynamics Program at the Woods Hole Oceanographic Institution.

No part of the dissertation has been submitted for any qualification other than the Doctor of Philosophy at the University of Cambridge.

Abstract

Materials can flow down a slope in a wide range of geophysical and industrial contexts, including lava flows on volcanoes and thin films on coated surfaces. The aim of my research is to provide quantitative insight into these forms of motion and their dependence on effects of the topography, the volume and the rheology of the flowing structure. Numerous different problems are investigated through mathematical models, which are developed analytically and confirmed by laboratory experiments.

The initial advance of long lava flows is studied by considering the flow of viscous fluid released on sloping channels. A scaling analysis, in agreement with analog experiments and field data, offers a practical tool for predicting the advance of lava flows and conducting hazard analysis. A simple and powerful theory predicts the structure of flows resulting from any time-dependent release of fluid down a slope. Results obtained by the method of characteristics reveal how the speed of the advancing front depends importantly on the rate of fluid supplied at an earlier time.

Viscous flows on surfaces with different shapes are described by similarity solutions to address problems motivated by engineering as well as geophysical applications. Pouring viscous fluid out of a container can be a frustratingly slow process depending on the shape and the degree of tipping of the container. The discharge rate of the fluid is analysed in simple cases, shedding light on how containers can be emptied most quickly in cosmetic and food industries. In a separate study motivated by coating industries, thin films are shown to evolve with uniform thickness as they drain near the top of a horizontal cylinder or sphere. The leading edge eventually splits into rivulets as predicted theoretically and confirmed by experiments.

Debris flows can develop levees and trigger avalanches which are studied by considering dense granular flows down a rough inclined plane. Granular materials released down a

slope can produce a flowing structure confined by levees or trigger avalanches at regular intervals, depending on the steady rate of supply. The experimental results are discussed using theoretical ideas of shallow granular flows.

Finally, materials flowing in long and slender ducts are investigated theoretically to better understand the digestive and urinary systems in biology. The materials are pumped in an elastic tube by translating waves of muscular contraction and relaxation. The deformation of the tube is predicted by solving a free-boundary problem, a similar mathematical exercise to predicting the moving boundaries of materials spreading on slopes.

Contents

Chapter 1

Introduction

1.1 Physical motivation

This thesis is concerned primarily with the dynamic process of materials spreading on slopes. Gravity can drive materials of all kinds to flow, ranging from small-scale coatings in manufacturing processes to large-scale avalanches in mountainous regions. It is of interest to understand quantitatively how the bulk structure evolves in depth and extent. This allows the possibility of predicting where and how quickly the spreading occurs in different situations, as demonstrated in numerous examples below.

Geophysical examples include debris flows, landslides and snow avalanches (figure 1.1) on mountains. They are natural hazards involving the motion of large masses of rock, water and snow. As a consequence, many casualties are produced and properties are severely damaged. The economic cost of repairing the damage is enormous. Despite the risks on mountains, people are attracted by the beautiful scenery and engage in outdoor activities, including climbing and skiing. Natural hazards on mountains not only affect people but also the rich biodiversity and vegetation, which are fundamental to the natural environment.

Figure 1.1: *Photograph of an avalanche initiated by an explosion at the Vallee de la Sionne (WSL Institute for Snow and Avalanche Research SLF, 2006).*

There are additional risks to habitats on volcanoes where lava (figure 1.2) and pyroclastic flows develop. The pyroclastic material can mix with water, after a heavy rainfall, and produce a type of mudflow called lahar. These natural hazards have the potential to destroy anything along their path with catastrophic consequences. Nevertheless, communities settle on volcanoes for numerous reasons, including the availability of geothermal resources of energy and fertile soil containing useful minerals for farming. Researchers spend time on volcanoes studying surface features, such as the deposits of past lava flows as shown in figure 1.3. The deposits reveal how the lava split into branches and flowed in channels confined by levees. These features are footprints of past activities and provide clues to possible consequences of future eruptions.

A quantitative prediction of where materials could spread on land offers both immediate and long-term benefits to society. Infrastructure can be developed in relatively safe areas by identifying and assessing possible areas of future development. Barriers can be constructed accordingly to divert flows like snow avalanches and protect the developed areas. In the event of a natural hazard, such as the advance of long lava flows, it is helpful to update communities with the latest information. Accurate information minimises any fear and supports the mental health of individuals concerned. The trust and cooperation of the general public are essential for evacuating communities from areas at risk. The public demands accurate and reliable information, which requires a quantitative prediction of

Figure 1.2: *Aerial view of Pu'u O'o fountain and lava flows on Kilauea Volcano, Hawaii (J.D. Griggs, U.S. Geological Survey, 1984).*

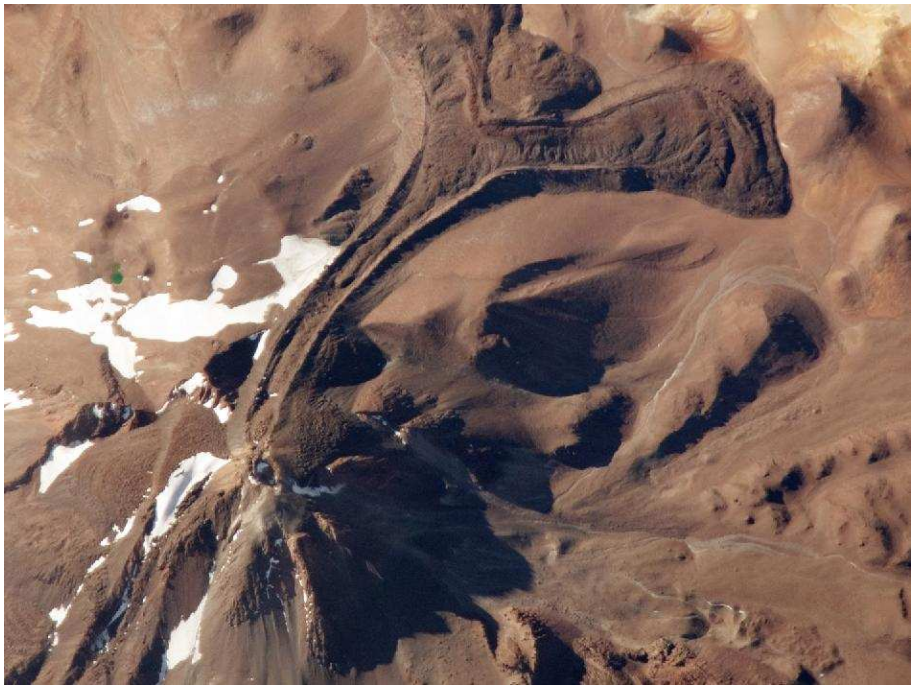

Figure 1.3: *Photograph of Llullaillaco Volcano, at the border of Argentina and Chile, taken from aboard the International Space Station (National Aeronautics and Space Administration, 2010). Several channels of deposited lava extend from the summit, which is elevated 6,739 m above sea level.*

how large masses flow on topography.

The spreading of materials on slopes occurs at smaller scales at home on a daily basis. A familiar example at the dining table is the spreading of sauce on food (figure 1.4). The sauce extends and produces multiple drips like branches of lava on a volcano. Another example at home is the frustratingly slow flow of shampoo in a bottle, which is tipped to discharge the fluid. Emptying the bottle is difficult so the remaining fluid is wasted. The disposal of fluid can pollute the environment with undesirable chemicals. In order to reduce the waste of products, such as food and cosmetics, the shape of their containers could be engineered so that the contents can pour out most effectively.

The spreading of thin liquid films on rigid surfaces is of interest to many industries. An example is the coating process of manufactured products, ranging in scale from small electronic components to large motor vehicles. The coatings are helpful for decorative purposes and protecting surfaces from rusting. In order to control the coatings before they ultimately dry, their motion must be predicted. This requires a quantitative understanding of the moving boundaries of thin liquid films (Oron *et al.*, 1997).

Moving boundaries of materials not only arise on slopes but also in other settings, such as the inside of a flexible duct like the body of a python (figure 1.5). Waves of

Figure 1.4: *Sticky toffee sauce spreading on a pudding. The photograph was taken by Ioanna Vlahou, my office mate at the Institute of Theoretical Geophysics.*

Figure 1.5: *Photograph of a 6m-long python swallowing a pregnant ewe (Reuters, 2006).*

muscular contraction and relaxation can travel down the duct, resulting in deformation of the duct and propulsion of the inner contents. The motion is fundamental to many systems in biology, including the digestive system, which can be studied through mathematical models.

1.2 Mathematical motivation

All of the physical examples presented above can be studied through mathematical models of materials with moving boundaries. This is pursued by formulating and solving problems in a mathematical framework. A major strength of the mathematical approach lies in its general applicability to physical systems of any size within a wide range of length scales. In order to gain a quantitative understanding of the physical systems, the associated challenges in mathematics must be addressed.

There are open problems associated with the mathematical treatment of materials spreading on slopes. An issue that remains unresolved is the dynamics of contact lines, which may play a role at the leading edge of a driven film of fluid. Although the issue can be partly resolved by introducing the notion of a slip velocity (Dussan, 1979) or by considering an extremely thin precursor film (Troian *et al.*, 1989; Spaid & Homsy, 1996), the most effective approach remains debatable. Another challenging issue is the mechanics of granular materials (GDRMiDi, 2004) like sand, which can switch between a flowing state, behaving like fluid, and a jammed state, behaving like a solid. Microscopic effects in the material can result in macroscopic phenomena and entirely change the bulk structure of the flow.

In an attempt to gain a better understanding of these systems, we develop simplified models of viscous fluids and granular materials flowing on slopes. Continuum models are developed by neglecting microscopic effects, which do not influence the dynamics of the bulk structure under specific conditions to be determined. The models are validated by comparing the theoretical solutions with analog experiments in the laboratory. The experiments are helpful for identifying the limitations of the simplified models. The models can then be extended to incorporate additional effects. The power of simplified models is that they provide a foundation for studying more complicated systems in the future.

The models considered here are simplified by the approximation that the flowing structure is long and thin, as in lubrication theory (Acheson, 1990). Solutions, which are obtained analytically by solving the governing equations, provide a fairly complete description of the dependence on physical parameters. We consider numerous different problems to better understand how flowing structures depend on the volume, the topography and the rheology of the material.

1.3 Thesis structure

In chapter 2, the initial advance of long lava flows is considered. A scaling analysis of Newtonian flow in open channels suggests that the initial advance depends importantly on the effusion rate and minimally on topography. Scaling laws for the advancing extent of the flow are compared with field data.

In chapter 3, variations in the supply of fluid from a source down an inclined plane are considered. The speed of the front of the resultant flow depends importantly on the rate of supply at a prior time, as investigated using the method of characteristics. We consider specific examples of releasing fluid at variable rates, including a supply which decays exponentially and a supply which oscillates sinusoidally about a mean flux.

In chapter 4, the effect of introducing a sharp change in the slope of the inclined plane is investigated. This is relevant to the process of pouring fluid out of a tipped container. Flow in two different containers is analysed to show that the discharge rate of the fluid depends importantly on the shape of the container.

In chapter 5, the effect of a slowly-varying angle of inclination of the substrate is studied. This is relevant to the process of coating a curved surface, such as the top of a sphere. When a constant volume of fluid is released rapidly on the surface, the leading edge of the flow can split into a series of rivulets, making it difficult to coat the surface completely. The rivulets develop when the front extends beyond a critical distance, which increases significantly with the fluid volume.

In chapter 6, the effect of a slowly-varying width of a channel with rectangular cross-section is studied. This is relevant to coating a sector of an inclined plane. The leading front of the flow down the channel detaches from the sidewalls when it extends a critical distance, which depends mainly on the fluid volume.

In chapter 7, the steady flow of granular materials down a rough inclined plane is investigated. The flowing structure has features which are not present in Newtonian flows, indicating that changing the rheology can introduce new flow phenomena. These include the formation of levees which confine a continuous stream at large mass flow rates and the development of avalanches at small flow rates.

In chapter 8, avalanches of sand flowing down a rough inclined plane are examined. Laboratory experiments are reported to show how avalanches can be triggered at regular intervals from a steady source. The avalanches retain their shape and size as they travel steadily on an erodible bed down the slope.

In chapter 9, the steady translation of waves of muscular contraction and relaxation down an elastic tube are considered. The resultant deformation of the tube and the propulsion of the inner contents are studied. Different results are obtained by considering the propulsion of a Newtonian fluid, a Bingham plastic and a rigid body immersed in viscous fluid. The motion depends importantly on the type of material.

Chapter 2

Initial advance of long lava flows in open channels

2.1 Abstract

The initial development of long lava flows is investigated using simple theory and field evidence. Order-of-magnitude estimates of the evolving thickness and the extending length of lava are obtained by scaling arguments based on the simplification that the bulk structure can be modelled initially as a Newtonian fluid. A scaling analysis suggests that the rate of advance of the leading front evolves primarily due to temporal variations in the effusion rate and minimally due to topography. The apparent viscosity of the bulk flow increases with time at subsequent stages when effects due to cooling become important. Theoretical results are applied to the study of long lava flows that descended on Etna, Kilauea and Lonquimay volcanoes. We determine that lava flows at Kilauea extended initially like a Newtonian fluid with constant viscosity, implying that thermal effects did not significantly influence the dynamic properties of the bulk flow. In contrast, effects due to cooling played a major role throughout the advance of lava flows at Etna and Lonquimay.

We show that the increasing length and volume of an active emplacement field can be monitored to estimate its evolving viscosity, which in turn allows the further advance of the lava to be predicted.

2.2 Introduction

Lava flows occur when molten rock is extruded from a volcanic vent. A long channel of lava may develop down a slope, where the flow is driven by gravity and confined laterally by elevations in topography. The lava quickly cools and solidifies at the margins of the flow, where levees form and further confine the flow (Hulme, 1974; Sparks *et al.*, 1976). The upper surface of the lava may also solidify to form a lava tube system whereby the lava continues to flow inside a completely enclosed passage (Greeley & Hyde, 1972; Hallworth *et al.*, 1987; Calvari & Pinkerton, 1999). The confinement may insulate the interior of the channel, allowing the lava to flow efficiently, without much loss of heat, towards its leading front (Keszthelyi, 1995). The front of the flow may propagate, branch into different lobes and stagnate in a complex series of processes (e.g., Lipman & Banks, 1987), before the entire structure of the emplaced lava solidifies.

One of the motivations for understanding the morphology of lava flows is to predict and evaluate the consequences of an effusive eruption. The resultant flow of hot and destructive lava can reach distant areas, threatening lives and damaging properties (Blong, 1984). An accurate prediction of the evolution of active lava flows is helpful for identifying danger zones and assessing risks posed to areas on volcanoes. For the purposes of effective forecasting, it is useful to be able to predict the extent of lava based on conditions that can be measured prior to or during the early stages of lava emplacement.

Previous studies obtained empirical relationships showing that the final lava length is correlated to a number of factors, including the mean effusion rate at the vent (Walker, 1973), the total erupted volume (Malin, 1980) and the rheology of the lava (Pinkerton & Wilson, 1994). An idea has been put forward that the flow is either cooling-limited when it reaches a maximum length attainable for a given supply of lava from the vent or volume-limited when a considerable decline in the effusion rate prevents the flow front from reaching the maximum length (Guest *et al.*, 1987). In either case, the final length of the lava is controlled by dynamic processes involving heat loss and depends importantly on the effusion rate (Harris & Rowland, 2009). We complement previous studies by examining dynamically how the various input factors, including variations in the effusion rate and effects due to cooling, influence the lava flow before it ultimately stops.

The dynamic processes leading to the final solidified state require understanding of the fluid dynamics of the lava (Griffiths, 2000). Of particular importance is the development

of lava flows during their early stages, when the flow front advances rapidly and reaches a large proportion of its final extent. A quantitative formulation of the initial advance of long lava flows forms an important foundation for studying subsequent stages of the evolving morphology of lava. The use of scaling arguments, which are applied to the early stages, could be developed further to study other problems including the prediction of the final lava extent, which is beyond the scope of the current investigation.

During the early stages, an open channel develops down a slope and directs the flow towards its advancing front (Hulme, 1974; Kerr *et al.*, 2006). The resultant flow during the early stages is commonly modelled as Newtonian and laminar (Tallarico & Dragoni, 1999; Sakimoto & Gregg, 2001). There is a rich class of mathematical problems relevant to the prediction of lava flows (Baloga & Pieri, 1986; Bruno *et al.*, 1996). The apparent viscosity of the bulk structure of the lava is expected to remain constant until the flow is influenced by thermal effects, which change the dynamical properties of the lava in two important ways. First, crystals may nucleate due to degassing and grow in the flow, effectively increasing the viscosity of the lava (Sparks *et al.*, 2000). Second, a crustal layer may develop on the surface due to cooling (Griffiths & Fink, 1993), effectively introducing an additional resistance to flow. Both mechanisms reduce the flow speed considerably until the flow stagnates altogether.

Here, we consider the initial advance of lava flows supplied down open channels of different shapes. The aim is to provide theoretical insight into natural lava flows by simplifying the analysis as much as possible while including the most fundamental mechanisms. For simplicity, the lava is modelled as Newtonian and we study the effects on the bulk flow due to given variations in the topography, the effusion rate and the apparent viscosity. Theoretical results obtained are applied to describing lava flows that descended the volcanic slopes of Etna, Kilauea and Lonquimay. The theoretical treatment is presented first in section 2.3, followed by applications to field data in section 2.4. We demonstrate how increases in the viscosity of the lava and further advance of the flow front can be predicted solely based on prior measurements of the cumulative volume and the length of an evolving emplacement field.

2.3 Theory

Consider an open channel of lava flowing down a slope. The channel may represent topography confining the entire length of lava that has been extruded from a volcanic vent, as long as the flow does not split into different branches. The following analysis applies equally well to lava that has branched off from another channel and extends thereafter as a single lobe. We are concerned with the temporal evolution of the dimensions of a single

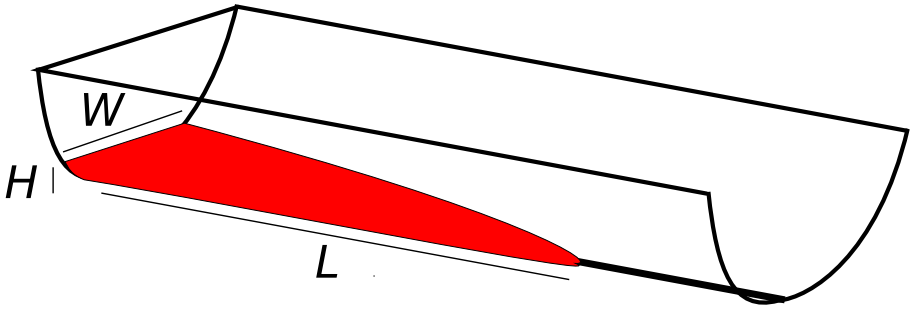

Figure 2.1: *A sketch of lava of typical length L, width W and height H flowing inside a channel of cylindrical shape.*

channel of lava. Of interest are the characteristic height $H(t)$, width $W(t)$ and length $L(t)$ of the flow at time t. The flow is primarily along the channel, provided that the dimensions of the flow satisfy $H \ll W \ll L$.

The exact shape of the channel confining the flow of lava will depend on a number of factors, which include the pre-existing topography and the development of levees at the margins of the flow. However, as we discuss later, the details of the channel do not significantly influence the flow. Consider a general relationship between the width and thickness of the flow of the form

$$H/w_* \sim (W/w_*)^n, \tag{2.1}$$

where $\sim$ denotes a relationship of proportionality, w_* is a measure of the size of the channel and n is a prescribed constant that describes the shape of the channel. For example, the limit as $n \to \infty$ is equivalent to $W \sim w_*$ and corresponds to a shallow layer of lava flowing down a flat channel of constant width w_*. Channels confining lava are approximately described by n taking some finite value greater than 1. For instance, $n = 2$ corresponds to a thin layer of lava flowing inside a channel of cylindrical shape whose radius of curvature, w_*, is much larger than the characteristic flow thickness, as shown in figure 2.1. The case of $n = 1$ describes flow along a wedge. Deep and narrow flows, described by $n < 1$, are not considered here because they are sheared predominantly across fractures of width $W \ll H$ and do not apply to natural lava flows.

The exact velocity varies within the lava but has a common characteristic magnitude denoted by $U(t) \sim L/t$ because L is the only characteristic length scale associated with the direction of flow along the channel. In particular, U is the characteristic rate of advance of the flow front, which is estimated by considering the governing equation of Newtonian and laminar flow. The driving force of gravity must balance the resistive forces due to the viscosity of the lava, provided that inertial effects are negligible. The component of gravity in the direction of the flow is given by $\rho g \sin\theta$, where ρ is the density of the lava, g the

acceleration due to gravity and θ the angle of inclination of the channel to the horizontal. The lava is sheared predominantly across its thickness because the resistive forces exerted at the sides of the flow are negligible, since $H \ll W$. The flow is sheared at the base, where we impose the condition of no slip. Shear stresses exerted by the ambient or any development of a crustal layer on the free surface are considered to be small initially. Given that the flow is sheared across its thickness, the viscous forces scale like $\mu U/H^2$, where μ is the dynamic viscosity of the lava. By balancing gravity with viscous forces and rearranging, we obtain the characteristic speed of the flow

$$U \sim \rho g \sin\theta H^2/\mu. \tag{2.2}$$

Note that (2.2) is consistent with an equation quantifying the surface velocity of flow down a channel with rectangular cross-section, often referred to as the Jeffreys equation (Jeffreys, 1925). The flow speed depends importantly on H, the thickness of the flow, which is set by the supply of lava into the channel.

The supply of the lava into the channel from upstream depends on the effusion rate at the vent and generally varies with time. The effusion rate corresponds to the rate of change of the cumulative volume of extruded lava. Typically, the effusion rate increases initially during a waxing phase and then decreases slowly during a waning phase (Wadge, 1981). To illustrate the effects of the lava supply on the resultant flows down open channels, we consider a simple power-law dependence of the effusion rate with time, which is expected to fit field data during the initial stages of an effusive eruption. Let the effusive activity at the vent begin at time $t = 0$ such that the cumulative volume of extruded lava is given by

$$V = V_*(t/T_*)^\alpha, \tag{2.3}$$

where T_* is some fixed time scale at which the volume erupted is $V = V_*$. The exponent $\alpha \geq 0$ is a prescribed constant and describes the temporal evolution of the effusion rate at the vent. For example, $\alpha = 0$ corresponds to a fixed volume V_* of lava extruded rapidly at time $t = 0$ and no further extrusion subsequently. Another example of importance is $\alpha = 1$, which corresponds to a continuous supply of lava with a steady effusion rate at the vent. A more general situation, where the effusion rate at the vent declines continuously with time, is described by α taking some value between 0 and 1. Note that the volume of extruded lava for general $\alpha > 0$ in (2.3) grows indefinitely, which does not model the effusion rate at large times. Nevertheless, (2.3) provides useful insight into the development of long lava flows during the early stages of the propagation, as we investigate below.

The cumulative volume of lava in the channel given by (2.3) must scale like

$$V \sim HWL. \tag{2.4}$$

By eliminating W, H and V from the coupled relationships (2.1)-(2.4) and the relationship $U \sim L/t$, the scaling for the extent of the flow at time t is given by

$$L \sim t^{(2\alpha n+n+1)/(3n+1)}. \tag{2.5}$$

The exponent $c = (2\alpha n + n + 1)/(3n + 1)$ depends only on the evolving nature of the effusion rate at the vent described by α in (2.3) and the shape of the channel described by n in (2.1). The exponent c does not depend on the viscosity of lava or the slope angle of the channel, as long as they remain approximately constant.

The scaling of the flow length given by (2.5) is consistent with a more detailed theoretical analysis and agrees well with data from a series of laboratory experiments (Takagi & Huppert, 2007; 2008). The experiments were conducted by supplying glycerine inside a wedge or a semi-circular channel either instantaneously or continuously with a steady flux, verifying the validity of (2.5) when $n = 1, 2$ and $\alpha = 0, 1$. The special case of $\alpha = 0$ not only describes the flow of an idealized situation of an instantaneous release of fluid into an inclined channel, it also describes the flow of a more general situation where the fluid is supplied from the upstream end of an inclined channel over a duration that is much shorter than the time scale of the resultant flow. In the context of a brief effusive eruption, where a considerable volume of lava is extruded during a relatively short period, the resultant flow does not depend on the details of the effusive activity and extends like (2.5), with $\alpha = 0$.

The numerical value of the exponent c, previously introduced so that the flow extends with time like t^c, provides an important insight into the evolving nature of lava flows in open channels. Depending on whether $c < 1$, $c = 1$ or $c > 1$, the position of the front decelerates, progresses steadily or accelerates, respectively, with time. A close inspection of the dependence of the exponent c on n in (2.1) and α in (2.3) reveals that the shape of the topography is not as important as the nature of the temporal variations in the effusion rate. This is illustrated by a stronger dependence of c on α than n, as shown in figure 2.2 for $\alpha = 0$, 1 and 2. In fact, in the special case of a steady effusion rate at the vent ($\alpha = 1$), the flow front advances steadily in open channels of any shape.

Given that the shape of the channel does not significantly influence the exponent c, a representative shape of a channel with rectangular cross-section will be considered in all the analysis to follow. The flow is effectively two-dimensional, independent of the cross-stream direction. By taking the limit as $n \to \infty$ in (2.5), we determine the extent of the flow down a flat channel of characteristic width a to be given by

$$L \sim \left(\rho g \sin\theta A_*^2 T_*/\mu\right)^{1/3} (t/T_*)^{(2\alpha+1)/3}, \tag{2.6}$$

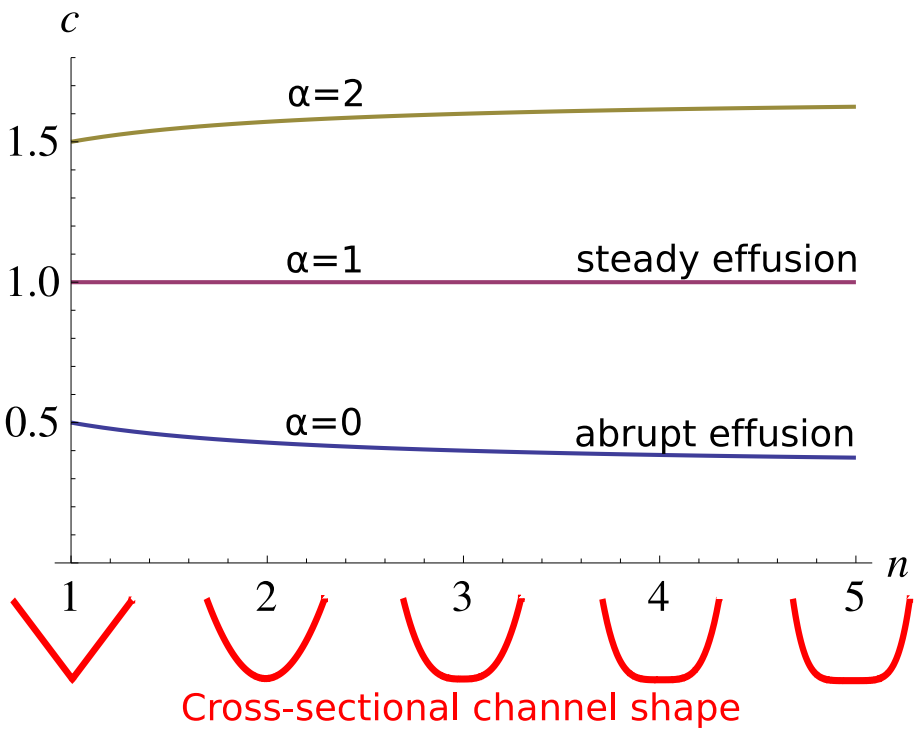

Figure 2.2: *Plot of c against n for three different values of α, where a cumulative volume $\sim t^{\alpha}$ results in a lava flow of length $\sim t^{c}$. The number n describes the cross sectional shape of the channel, as sketched beneath corresponding integer values of n.*

where $A_* = V_*/w_*$ is the characteristic area of lava extruded in time T_* per unit cross-stream width w_*. The extent of the flow advances at least like $t^{1/3}$, provided that the lava descends down the channel like a Newtonian fluid of constant viscosity. Note that L in (2.6) does not change much as a result of minor variations in θ and w_*, reinforcing the idea that topographic variations play a minor role in governing the length scale of the flow. By coupling relationships (2.3) and (2.6), we determine the characteristic thickness of the flow to be given by

$$H \sim [\mu A_*/(\rho g \sin\theta T_*)]^{1/3} \, (t/T_*)^{(\alpha-1)/3} \, . \tag{2.7}$$

A declining supply of lava into the channel with $\alpha < 1$ in (2.3) leads to a decreasing thickness of the lava with time, as expected. The scalings (2.6) and (2.7) are consistent with the mathematical solutions obtained by a more detailed analysis (Lister, 1992).

When the length and thickness of lava flowing down an inclined channel scale like (2.6) and (2.7) respectively for some common value α, the implication is that the lava is flowing like a Newtonian fluid of constant viscosity. If the temporal variations of either (2.6) or (2.7) disagree with α in (2.3), which can be measured independently by monitoring the cumulative volume of lava, then the theoretical assumptions made so far need to be revised. The obvious source of the problem lies in the simplifying assumption so far that the viscosity remains constant. As the lava cools, its viscosity may increase by orders of magnitude.

It is helpful to consider the effects on the flow due to a time-dependent viscosity of the form $\mu \sim t^\beta$ for some β. Although this power-law is not the end result of an explicit theoretical development, a similar analysis has provided insight into the growth of lava domes (Sakimoto & Zuber, 1995). This approach has the advantage of simplifying the analysis without considering the details of the temperature-dependent viscosity (Shaw, 1969). The specific viscosity of lava may vary in position but the bulk structure is simplified to flow with an apparent viscosity, whose order of magnitude depends only on time. By setting $\mu \sim t^\beta$ in (2.6), the characteristic thickness of the flow evolves in the form

$$H \sim t^{(\beta+\alpha-1)/3} \tag{2.8}$$

behind an advancing front of the flow, extending a distance

$$L \sim t^{(2\alpha+1-\beta)/3}. \tag{2.9}$$

Relationships (2.8) and (2.9) indicate that an increase in the viscosity with time, represented by $\beta > 0$, results in a channel of thicker lava, which advances at a slower rate compared to the corresponding flow without any increase in viscosity. For example, a

significant rise with time in the level of lava inside a channel, which is being supplied at a steady rate, can be explained by setting $\alpha = 1$ in (2.8) and deducing that the viscosity of the lava is increasing considerably with time.

Another possibility that gives rise to a considerable decline in the speed of the flow is the additional force resisting the motion due to the formation of a crustal layer on the upper surface of the flowing lava. Effects on the lava flow due to the development of a surface crust are presented below for the propagation down a slope, which is different from a growing lava dome on a horizontal surface (Griffiths & Fink, 1993). The idea is that cooling is assumed to be confined to a thin thermal boundary layer of characteristic thickness δ near the crust, below which the interior flow of lava remains isothermal. The approximation holds for a sufficiently large Peclet number $UH/\kappa \gg 1$, where κ is the thermal diffusivity of the lava flowing under the crust. Thermal conduction is assumed to be most significant across the depth so that the crustal thickness grows diffusively like

$$\delta \sim (\kappa t)^{1/2}. \tag{2.10}$$

The crust is approximated to have a thickness proportional to the thermal boundary layer and exert a shear stress $\sigma_c \delta$ on the flowing lava per unit surface area, where σ_c is the effective shearing strength. Under these assumptions, the driving force due to gravity is no longer balanced by viscous forces at the base of the channel and within the flowing lava but instead by $\sigma_c \delta / H$, the retarding force per unit volume due to the surface crust. By setting $\rho g \sin\theta \sim \sigma_c \delta / H$ and coupling with (2.3) and (2.4), we determine the characteristic thickness of the bulk flow to grow like $t^{1/2}$ behind an advancing front, which extends a distance

$$L \sim t^{\alpha - 1/2}. \tag{2.11}$$

Note that (2.11) is equivalent to (2.9) with $\beta = 5/2 - \alpha$, suggesting that the bulk flow with a surface crust extends like a fluid with apparent viscosity that grows in time like $t^{5/2-\alpha}$. Note also that an advancing flow front requires a continuous supply of lava with $\alpha > 1/2$. The scaling given by (2.11) does not hold for a cumulative volume of lava described by $\alpha \leq 1/2$, suggesting that the entire structure of the flow cools and comes to rest when there is insufficient supply of lava driving the flow in the insulated interior under the crust. Ultimately, the downslope acceleration due to gravity must be countered by static rather than viscous forces.

The applicability of the scaling laws introduced in this section is best assessed by testing against data of natural lava flows. The theory predicts the characteristic thickness of lava to scale like (2.8) and the extending length like t^c as in (2.9), provided that the cumulative volume scales like t^α and the apparent viscosity of the lava like t^β. The scaling relationships are useful for estimating any variation with time in the viscosity of the lava,

Location	Start date	Reference
Etna	18 Jul 2001	LFS1, Coltelli *et al.* (2007)
Kilauea	13 Jun 1983	Episode 4, Wolfe *et al.* (1988)
Kilauea	22 Jul 1983	Episode 6, Wolfe *et al.* (1988)
Kilauea	30 Mar 1984	Episode 17, Wolfe *et al.* (1988)
Lonquimay	27 Dec 1988	Naranjo *et al.* (1992)

Table 2.1: *Table of selected lava flows investigated in this article.*

which is difficult to measure directly in the field. When the cumulative volume of lava is plotted against time on logarithmic scales, the slope of the line of best fit is α. Similarly, c can be obtained by finding the slope of the line of best fit through data of the flow extent plotted against time on logarithmic scales. The theory predicts the apparent viscosity to have scaled like t^{β}, where $\beta = 1+2\alpha-3c$. In the following section, we demonstrate how the evolving viscosity and the morphology of natural lava flows can be explained using simple ideas that have been developed. It is not possible at this stage to conduct a complete test of the model partly due to the lack of data showing changes in the bulk viscosity of the flowing lava. Variations in the viscosity are inferred and remain to be tested against further data in future studies.

2.4 Natural lava flows

Many natural lava flows have been observed and studied extensively. Well-documented sets of field data are available in the literature describing the evolving morphology of long lava flows. We select representative sets of data to examine how a single channel of lava advances down a slope. The width of the flow and the slope do not change considerably with time or distance downstream, as assumed in the model. Lengths of the flow recorded at different times were compiled to investigate several different lava flows, as presented in table 2.1. The selected data provide us with an excellent opportunity to test the theoretical ideas developed in section 2.3.

A series of eruptive events occurred on the Kilauea Volcano of Hawaii starting in 1983. Episodes of vigorous fountaining at central vents resulted in basaltic lava flows, some of which extended several kilometers. Detailed narratives and graphical representations of lava flows during the first 20 episodes in 1983-1984 are available in Wolfe *et al.* (1988). We take a representative sample of episodes in which one major flow of lava extended from the central vent of Pu'u O'o.

A cone of Pu'u O'o marked the locus of major fountaining and lava discharge soon after the start of episode 4 during the late morning of 13 June 1983. The cone enclosed a

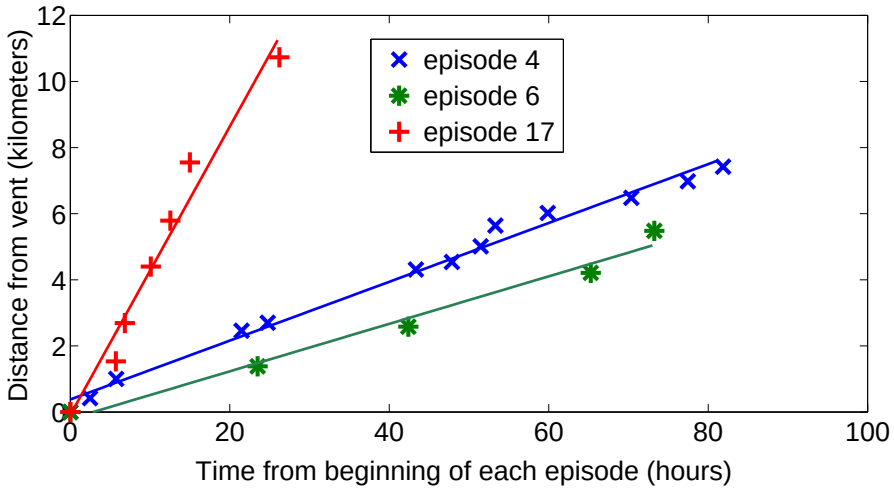

Figure 2.3: *Extent of the advancing front of lava plotted against time during three representative episodes of the Pu'u O'o eruption in Kilauea, 1983-1984. Data points are reproduced from figures presented on the plates of Wolfe* et al. *(1988).*

crater partly filled with lava, which overflowed and fed a well-developed channel. The lava flow advanced in the southeastern direction and extended a distance of 5.7 km by 16:00 on 15 June 1983. During this time, a time-lapse camera at the vent recorded low bursts of fragmented spatter rather than sustained fountains, which caused large fluctuations in velocity and thickness of the major flow. However, variations in fountain height in episode 4, as plotted in figure 1.24 of Wolfe *et al.* (1988), are not significant over the time scale of tens of hours during which the flow front advanced. This suggests that the major channel was fed with lava at an approximately steady rate (Wolfe *et al.*, 1988). The advancing position of the flow front is plotted against time in figure 2.3. Although the flow is reported to have experienced fluctuations in speed, the general trend is an approximately steady advance of the flow front until the afternoon of 16 June 1983. Both the discharge rate at the vent and the rate of advance of the major flow were approximately steady during the course of about three days so $\alpha = 1$ and $c = 1$. We deduce $\beta = 1 + 2\alpha - 3c = 0$, meaning that the major channel of lava flowed initially like a Newtonian fluid of constant viscosity.

Some subsequent episodes also featured a steady discharge rate of lava at the Pu'u O'o vent which resulted in a steady advance of a major flow. In episode 6, after a series of minor lava flows, one major channel of lava developed and extended to the north east. Figure 2.3 shows how the length of the flow initially extended. The rate of advance of the major flow remained steady from the early afternoon of 23 July 1983, when the channel began to extend, until the night of 24-25 July 1983, when the flow front divided into two parallel lobes. During this period, a steady and sustained discharge of lava supplied the major channel, while the flow front advanced at an average rate of 80m/h, suggesting that the viscosity remained constant.

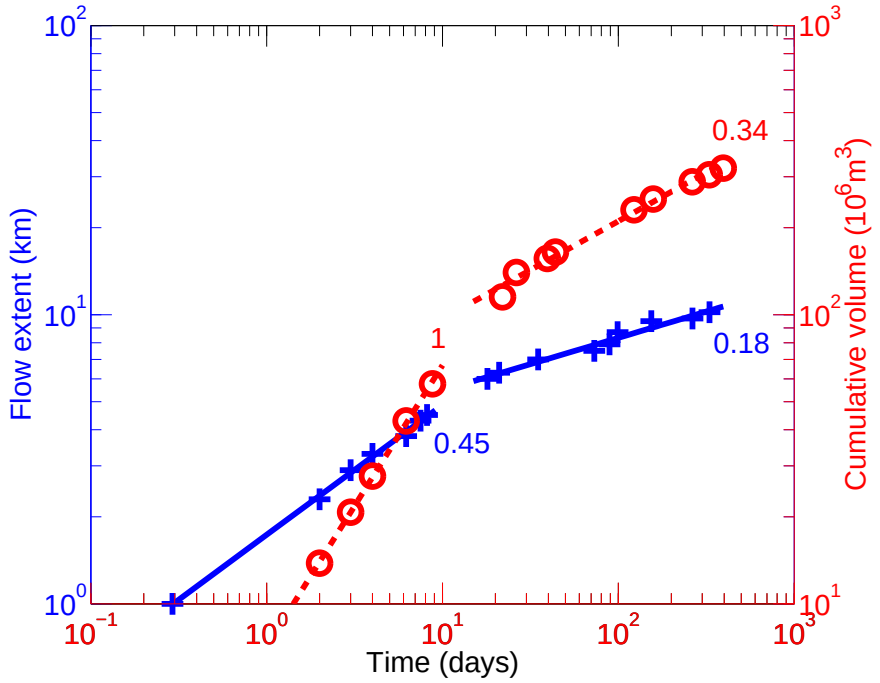

Figure 2.4: *Extent of the advancing front (+) and the cumulative volume (o) plotted against time on logarithmic scales for the main flow on Lonquimay, 1988-1989. Numbers represent the slope of the corresponding line of best fit. The cumulative volume scaled like t initially and $t^{0.34}$ subsequently, resulting in flow extending a distance proportional to $t^{0.45}$ initially and $t^{0.18}$ subsequently. Data points are from figure 3 and table 3 of Naranjo* et al. *(1992).*

In episode 17, a major channel of lava extended eastwards at an approximately steady rate of 490m/h from a distance 2km away from the base of Pu'u O'o, from the late morning until the evening of 30 March 1984. During the day, the fountain height remained at approximately 100m, suggesting that the discharge rate of lava was steady. The discharged lava was supplied primarily to the main eastern flow and minimally to its minor subordinate flow, as shown graphically on the map of episode 17 on plate 2 of Wolfe *et al.* (1988). The considerably faster flow in episode 17 compared to other episodes on Kilauea has been attributed partly to confinement of the flow (Wolfe *et al.*, 1988). However, the average width of the flow was 220m in episode 17, not much less than the widths of 230m and 260m in episodes 4 and 6 respectively. An increase of the effusion rate by a factor of almost four and a minor decrease in the flow width, which would increase $A_*^{2/3}$ in (2.6) by approximately 2.5, do not account for the increase in the flow speed by a factor of approximately six. The fast flow in episode 17 is primarily due to an order-of-magnitude decrease in the viscosity of the lava. This is consistent with Wolfe *et al.* (1988) who argue that increasing lava temperature, decreasing phenocryst content and changing lava composition may have been related to this apparent change in viscosity compared to earlier episodes.

On 27 December 1988, a major flow of andesite lava developed on Lonquimay Volcano in Chile which can be studied as follows. The main flow moved north-northeast down the Rio Lolco valley and extended to 10.2 km after 330 days. It has been observed that the lava of thickness $\sim 20\,\mathrm{m}$ and width $\sim 500\,\mathrm{m}$ extended in length $\sim 10^4\,\mathrm{m}$ within months by order of magnitude. Using these values in the scaling relationship (2.4), we obtain an order-of-magnitude estimate of the cumulative volume of extruded lava $\sim 10^8\,\mathrm{m}^3$, which is consistent with the measurement of the final volume of extruded lava, $2.3 \times 10^8\,\mathrm{m}^3$ (Naranjo *et al.*, 1992). The position and thickness of the continuously advancing flow front at different stages are presented in table 3 of Naranjo *et al.* (1992). A plot of the flow length against time on logarithmic scales is shown in figure 2.4. By calculating the slopes of the lines of best fit, we determine that the flow extended like $t^{0.45}$ for approximately the first 8 days and like $t^{0.18}$ thereafter, before the flow stopped. The cumulative volume of the flow increased approximately linearly with time at a rate of $6.9\times10^6\mathrm{m}^3$ per day for the first 8 days according to figure 3 of Naranjo *et al.* (1992). Given that the cumulative volume scaled like t and the flow extent like $t^{0.45}$, the theory developed previously predicts that the apparent viscosity increased with time like $t^{1.65}$ initially. Equation 2.11 with $\alpha = 1$ predicts $c = 0.5$, which is in reasonable agreement with the field data indicating $c = 0.45$, suggesting that the initial lava flow on Lonquimay was resisted by the development of a surface crust. At subsequent stages, the cumulative volume increased like $t^{0.34}$, where the exponent corresponds to the slope of the line of best fit through the corresponding data in figure 2.4. Setting $\alpha = 0.34$ and $c = 0.18$, we obtain $\beta = 1.14$ and deduce that the apparent viscosity increased with time like $t^{1.14}$. The theory shows that the viscosity of the lava increased with time throughout the course of the flow, which is consistent with the increase in the viscosity of the flow front as it advanced downstream (Naranjo *et al.*, 1992).

Detailed measurements of a long lava flow on Mount Etna in 2001 can be analysed in a similar fashion. A fissure close to Monte Calcarazzi between 2100 m and 2150 m above sea level, referred to as LFS1 in Coltelli *et al.* (2007), opened at 2:20 on 18 July 2001. The main lava flow continuously descended from the LFS1 vent and attained its lowest elevation of 1040 m on 25 July 2001, when the lava flow extended a distance of 6.4 km with a maximum width of 545 m. The major channel of lava was supplied predominantly from the LFS1 vent and minimally from a minor flow extending from another vent, LFS2. The cumulative volume of lava in the main LFS1 flow is presented in table 8 of Coltelli *et al.* (2007), which is approximated by (2.3) with $\alpha = 1.27$. Likewise, the extending length of the flow is found to scale like $t^{0.50}$. Given that $\alpha = 1.27$ and $c = 0.50$, the theory developed previously predicts $\beta = 2.04$. The apparent viscosity of the lava increased like $t^{2.04}$, suggesting that the flow decelerated considerably due to thermal effects.

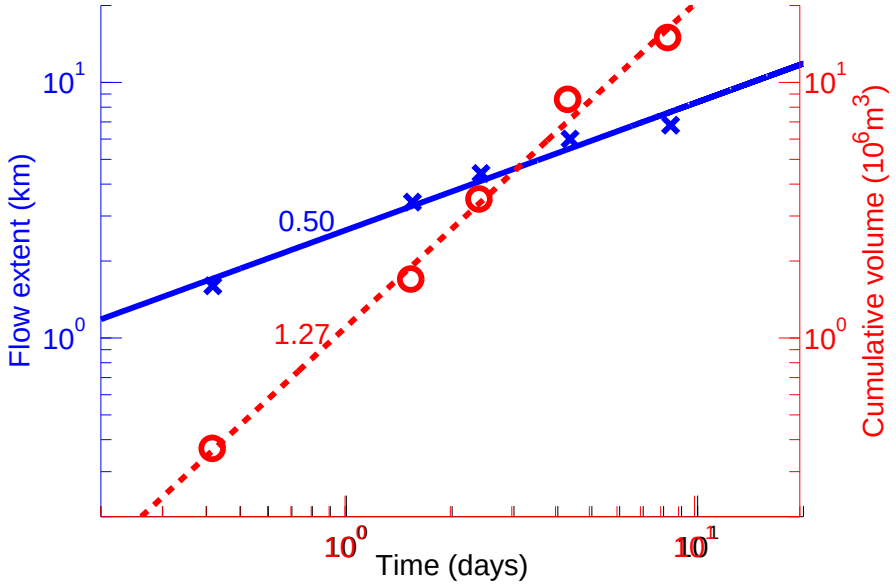

Figure 2.5: *Extent of the advancing front (x) and the cumulative volume (o) of lava both plotted against time on logarithmic scales during the early stages of the LFS1 flow on Etna in 2001 (Coltelli* et al.*, 2007). Numbers indicate the slope of the corresponding line of best fit.*

2.5 Summary

The initial advance of long lava flows was investigated quantitatively using scaling arguments. The extending length of the lava was shown theoretically to depend importantly on the supply from upstream and minimally on the shape of the channel. Thermal effects on the bulk flow were examined to play a major role at subsequent stages when the flow front decelerates considerably. The use of scaling arguments, as drawn out in this paper, can be extended to incorporate additional effects or even investigate new problems, including ones for which it is very difficult to write down the governing equations completely.

The theoretical predictions were applied to explain the initial development of natural lava flows on the volcanoes of Etna, Kilauea and Lonquimay. We determined that selected lava flows on Kilauea extended initially like a Newtonian fluid of constant viscosity, while lava flows on Etna and Lonquimay increased considerably in viscosity throughout the course of their propagation. This suggests that thermal effects due to cooling played a major role at all times as the flows advanced on Etna and Lonquimay but only after the flows nearly attained their maximal extent on Kilauea.

Our analysis of field observations demonstrates how the morphology of long lava flows can be studied readily using quick and simple techniques. The relationship $\beta = 1+2\alpha-3c$ allows one of the three parameters (α, β, c) to be calculated given the other two, where

the cumulative volume $\sim t^{\alpha}$ and viscosity $\sim t^{\beta}$ of the lava extends a distance $\sim t^{c}$. This relationship enables any variation in the apparent viscosity of the lava, a useful indicator of the role of heat loss, to be estimated solely by monitoring the growth rates of the cumulative volume and the flow extent. Values of α and β characterising active lava flows in the early stages provide an estimate of c, helpful for predicting any further advance of the lava.

Chapter 3

Variable flux of materials flowing down a slope

3.1 Abstract

Geophysical flows, including lava flows and ice streams, are supplied at a rate that naturally evolves in time. In order to investigate effects due to flux variations, we consider a time-dependent release of viscous fluid from a fixed source. The free surface of the resultant gravity-driven flow down a slope is described by a kinematic wave equation, based on the simplification that effects due to inertia and surface tension are negligible. Analytic expressions for both the thickness and the extent of the flow are obtained by the method of characteristics, given the flux at the source. The dimensionless speed of the front depends only on the source flux at a prior time, which jumps discontinuously when an internal shock reaches the front of the current. The theory is applicable to a wide range of problems as demonstrated in numerous examples. An exponentially decaying flux at the source results in a flow that initially resembles the flow from a steady supply and subsequently tends to the flow following an instantaneous release of a constant volume of fluid. A source flux that oscillates sinusoidally about a mean flux perturbs the extent of the flow but the perturbations decay at large times.

3.2 Introduction

Geophysical flows driven by gravity along a slope are often supplied from sources at variable rates. A molten rock of lava exudes from vents and fissures on volcanoes and descends down slopes (Griffiths, 2000). Glacier ice grows with snowfall and flows down a sloping valley (Nye, 1960). Debris flow of mud propagates down a sloping channel (Takahashi, 1981). A thin layer of water develops on growing icicles (Short *et al.*, 2006) and stalactites (Short *et al.*, 2005).

In simplified models of materials flowing primarily down a slope, the downstream flux at any position is proportional to some power of the local thickness. For example, the numerical value of the exponent is approximately 3 to 7/2 for glacial flows (Nye, 1960) and 5/2 for dense granular flow down a rough inclined plane (Pouliquen, 1999). The exponent depends on the rheology and also on topography, as shown for Newtonian flows in channels and fractures (Takagi & Huppert, 2008).

The evolution of the flow structure is unknown a priori and must be determined by solving a kinematic wave equation (Whitham, 1974). Solving the kinematic wave equation subject to a prescribed flux at a source is equivalent to solving a signaling problem (Whitham, 1974). This is relevant to a wide area of subjects, including flood waves (Lighthill & Whitham, 1955*a*) and traffic flow (Lighthill & Whitham, 1955*b*).

Analytic solutions obtained previously have been limited to a special class of problems. The volume per unit breadth of Newtonian fluid on a slope was considered to be of the form $V = qt^{\alpha}$, where t is time and q and α are non-negative constants (Huppert, 1982b; Lister, 1992). The special case of $\alpha = 0$ corresponds to releasing instantaneously a constant volume q of fluid from a line source. The case of $\alpha = 1$ corresponds to a continuous supply of fluid at a steady rate q.

Here, the volume of fluid on an incline is considered to grow as a general function of time. The objective is to determine the profile of the thickness and the extent of the resultant flow, given any prescribed flux at a fixed source. Of particular interest is the speed of the advancing front as a function of the variable flux at the source. Although the current focus is mainly directed towards the specific problem of predicting Newtonian flow down a slope, the theory is generally applicable to a wider range of problems involving kinematic waves.

In section 3.3, the governing equations are formulated and solved by the method of characteristics. In section 3.4, the theory is applied to specific examples, including a source flux that either decays exponentially or oscillates sinusoidally.

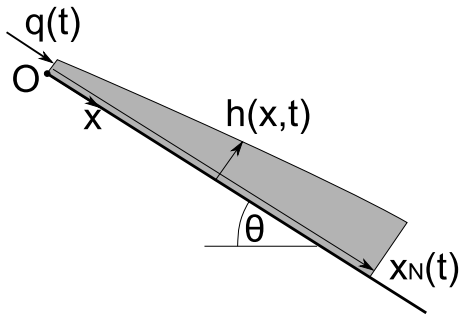

Figure 3.1: *Sketch of a thin film flow down a rigid slope. The fluid is supplied with a prescribed flux $q(t)$ from the origin.*

3.3 Theory

Although the theory can be readily generalized to predicting a large class of flowing materials, as outlined in the Appendix, we consider an incompressible Newtonian fluid of viscosity ν as a representative example. It is driven by gravity on a rigid slope of angle θ to the horizontal. Consider the source of fluid to be at the origin and denote the coordinate down the slope by x. A general flux $q(t)$ of fluid is supplied onto the slope at time $t \geq 0$. The resultant flow has a thickness denoted by $h(x,t)$ and an extent $x_N(t)$, as shown in Figure 3.1.

The flow is driven by gravity and resisted by viscous forces. Effects due to inertia of the fluid, any motion in the ambient fluid, surface tension at the free interface and dynamics near the contact line at the front of the current are all neglected. The flow is predominantly along the slope because its characteristic thickness, h, is much smaller than its length, x_N. The assumption that the characteristic variation of the flow thickness along the flow, $\partial h/\partial x$, is negligible compared to the slope of the incline, $\tan\theta$, ensures that the flow is driven only by the component of gravity along the slope. Under these conditions, lubrication theory with no-slip on the rigid slope gives rise to a nonlinear kinematic wave equation (Huppert, 1982b)

$$\frac{\partial h}{\partial t} + \frac{g\sin\theta}{3\nu}\frac{\partial h^3}{\partial x} = 0. \tag{3.1}$$

Laboratory experiments have verified that (3.1) describes the bulk region of the flow until an instability develops at the front, even though the assumption of $\partial h/\partial x$ may not hold near the front (Huppert, 1982b).

If the characteristic flux at the source is Q and the time scale of the flow is T, then the thickness and extent of the current can by scaled by H and X respectively, where

$$H \equiv \left(\frac{3\nu Q}{g\sin\theta}\right)^{1/3} \tag{3.2}$$

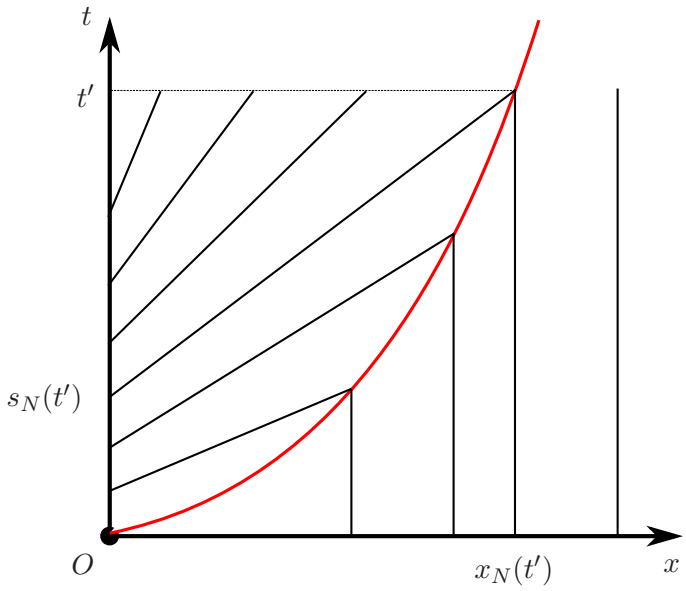

Figure 3.2: *Sketch of characteristic lines along which the thickness of the flow remains constant in the (x,t) plane. A shock forms at the front of the current, which is represented by the red curve. The characteristic line that leaves the source at time $s_N(t')$ reaches the front of the current $x_N(t')$ at time t'. Note that the characteristic lines leaving the x axis are vertical according to (3.5) and (3.7).*

and

$$X \equiv T \left(\frac{Q^2 g \sin\theta}{3\nu} \right)^{1/3}. \tag{3.3}$$

The dimensionless form of (3.1) reduces to

$$\frac{\partial h}{\partial t} + \frac{\partial h^3}{\partial x} = 0, \tag{3.4}$$

which must be solved subject to the initial condition

$$h(x, 0) = 0 \tag{3.5}$$

on the slope, $x > 0$, and the flux condition at the origin,

$$q(t) = h(0, t)^3. \tag{3.6}$$

Equation (3.4) implies that h remains constant along characteristics given by

$$\frac{dx}{dt} = 3h^2. \tag{3.7}$$

This corresponds to the wave speed at which information propagates downstream. By integrating (3.7), we obtain the equation for the characteristic line that leaves the source

at time s,

$$x = 3q(s)^{2/3}(t - s), \tag{3.8}$$

which is straight in the (x,t) plane. The characteristic line that reaches the front of the current x_N at time t is given by

$$x_N(t) = 3q[s_N(t)]^{2/3}(t - s_N(t)), \tag{3.9}$$

where $s_N(t)$ is the prior time when the line begins at the source, $x = 0$.

Consider first the case where a shock forms only at the front of the current, where a characteristic line from the t axis intersects a vertical characteristic line from the x axis. A representative set of characteristic lines is sketched in figure 3.2 along with the position of the current, which evolves along the red curve. Characteristic lines originating from the t axis in the (x, t) plane do not intersect each other before intersecting a characteristic line originating from the x axis because no shock forms internally in the current. In this case, for a given time t and extent x behind the front of the current, a single characteristic line reaches x at time t. Denote the time when this line leaves the source by $s(x, t)$. The thickness of the flow is

$$h(x, t) = q[s(x, t)]^{1/3}, \tag{3.10}$$

where $s(x, t)$ is an implicit expression given by (3.8).

By conservation of mass across a shock, the speed of the shock is given by

$$\frac{h_+^3 - h_-^3}{h_+ - h_-}, \tag{3.11}$$

where h_+ and h_- are respectively the thickness immediately behind and ahead of the shock. Note with $h_+ > h_-$ that the shock moves faster than the characteristic lines immediately ahead but slower than those behind the shock. In particular, $h_- = 0$ for the front of the current which advances at speed

$$\frac{dx_N(t)}{dt} = q[s_N(t)]^{2/3}. \tag{3.12}$$

The speed of the front at time t depends only on the source flux at the prior time of $s_N(t)$. In addition, the structure of the current at time t is independent of the source flux prior to time $s_N(t)$.

By differentiating (3.9) and equating with (3.12), we obtain an evolution equation for s_N,

$$\frac{ds_N(t)}{dt} = \frac{2q(s_N)}{3q(s_N) - 2(t - s_N)[dq/ds]_{s=s_N}}, \tag{3.13}$$

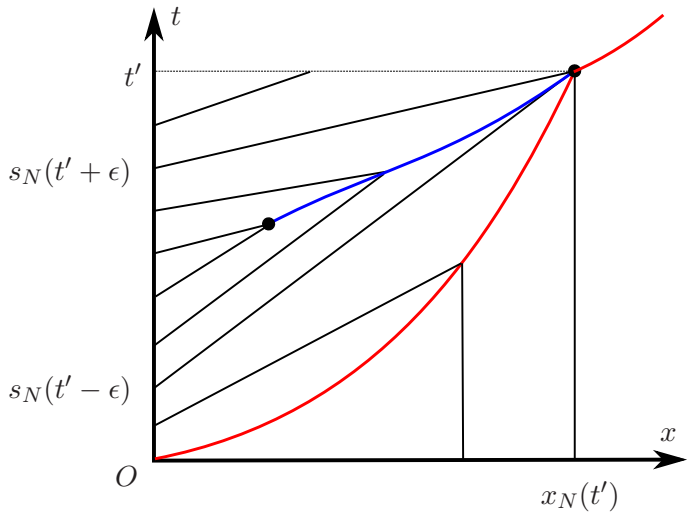

Figure 3.3: *Sketch of characteristic lines along which the thickness of the flow remains constant in the (x,t) plane. A shock forms at the front of the current, which is represented by the red curve. An internal shock is represented by the blue curve. The function $s_N(t)$ jumps discontinuously when the internal shock reaches the front of the current at time t'.*

which must be solved subject to the initial condition $s_N(0) = 0$. A continuous increase in s_N with time ensures a continuous advance of the flow front according to (3.12) without the development of internal shocks in the current. We obtain

$$3q(s_N) - 2(t - s_N)[\frac{dq}{ds}]_{s=s_N} > 0, \tag{3.14}$$

as the condition for no internal shock to form. An alternative derivation of the governing equations (3.12) and (3.13) is given in the Appendix.

Now consider the case when (3.14) no longer holds so an internal shock develops. Physically, a sharp change in the thickness of the flowing structure arises. In the (x, t) plane, characteristic lines originating from the source intersect each other as shown in figure 3.3. An internal shock forms at $x < x_N$ where $\partial x/\partial s = 0$. The shock propagates downstream at a speed given by (3.11), which can be challenging to compute in practice because h_+ and h_- in (3.11) may depend on the evolution of the shock in a nontrivial manner. Nevertheless, we can obtain the salient features by noting that the shock moves faster than the characteristic lines immediately ahead but slower than those behind the shock, as demonstrated in the example below of a film driven by an oscillating flux at large times. When an internal shock reaches the front of the current, s_N jumps discontinuously to the greatest value of s such that $x_N = 3q^{2/3}(t - s)$. Otherwise s_N evolves according to (3.13). The speed of the flow front is always governed by (3.12) and increases discontinuously when an internal shock reaches the flow front.

3.4 Examples

The theory is applied to specific examples with various different functions $q(t)$. In each case, given the prescribed flux at the source, the extent of the flow is determined.

3.4.1 Power-law flux

The method presented here is verified by considering the area of the fluid to obey a power-law in time,

$$A(t) = t^{\alpha}. \tag{3.15}$$

The problem can be solved by an alternative method of seeking similarity solutions (Lister 1992). These solutions provide a useful basis against which solutions obtained here can be tested.

By differentiating (3.15) with respect to time, we determine the flux at the origin to be

$$q(t) = \alpha t^{\alpha-1}. \tag{3.16}$$

By substituting (3.16) into (3.13) and rearranging, we obtain

$$s_N(t) = \frac{2\alpha\, t}{2\alpha + 1}. \tag{3.17}$$

The condition (3.14) with q given by (3.16) and s_N given by (3.17) reduces to the condition $\alpha \geq -1/2$ for no internal shock to form behind the front of the current.

Equations (3.16) and (3.17) are substituted into (3.10) and (3.12) to determine that the thickness of the flow at the front is given by

$$h(x_N(t), t) = \alpha^{\alpha/3}(\alpha + 1/2)^{(\alpha-1)/3} t^{(\alpha-1)/3}, \tag{3.18}$$

where the extent of the flow is given by

$$x_N(t) = 1.5\alpha^{2\alpha/3}(\alpha + 1/2)^{-(2\alpha+1)/3} t^{(2\alpha+1)/3}. \tag{3.19}$$

Equations (3.18) and (3.19) agree with the solutions that are obtained in terms of a similarity variable (Lister 1992).

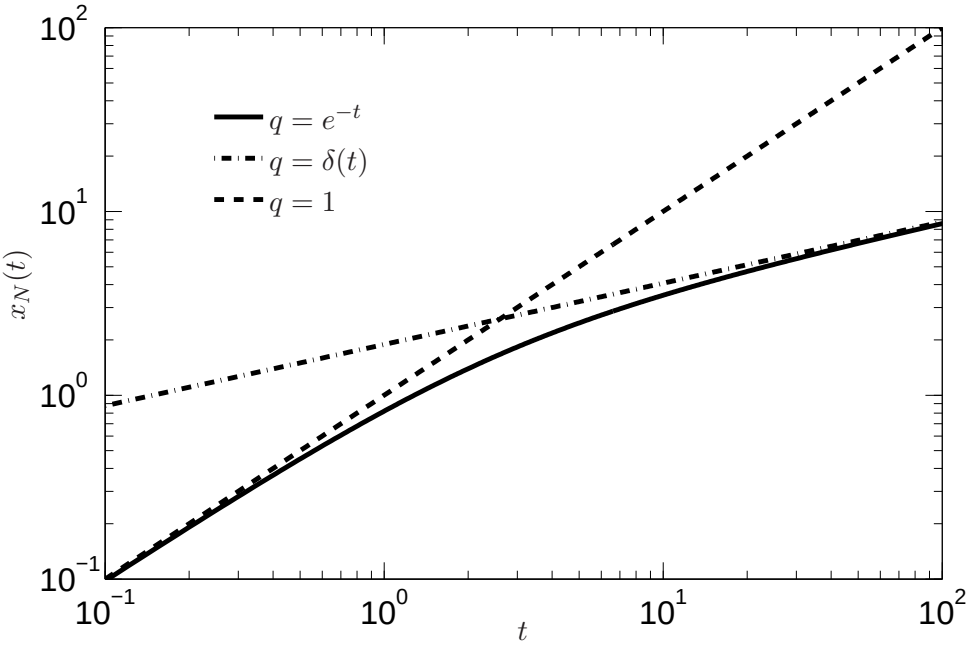

Figure 3.4: *Plots on logarithmic scales of three different dimensionless flow extents x_N in (3.22) against time. The flow results either from an instantaneous constant-volume release, a steady flux at the source or an exponentially decaying flux given by (3.20).*

3.4.2 Exponentially decaying flux

The effusion rate of lava at a volcanic vent is often believed to decay exponentially. Consider the flux of fluid at the source to be given by

$$q(t) = e^{-t}. \tag{3.20}$$

In the limit of small time, $t \ll 1$, the source flux remains approximately constant by (3.20). The source flux is effectively described by (3.16) with $\alpha = 1$ at early times. In the limit of large time, $t \gg 1$, the total volume of fluid asymptotes to a constant value. The flow corresponds to that initiated by releasing instantaneously a constant volume of fluid. The extent of the flow is expected to tend to (3.19) with $\alpha = 0$ as $t \to \infty$.

By substituting (3.20) into (3.13) and rearranging, we determine that s_N satisfies

$$2t = e^{s_N(t)} + 2s_N(t) - 1. \tag{3.21}$$

Condition (3.14) with q given by (3.20) and s_N satisfying (3.21) reduces to the condition that $2 + e^{s_N} > 0$, which holds for all time. No internal shock forms behind the front of the current when the flux is of the form (3.20).

By substituting (3.20) into (3.12), we determine that the extent of the flow is given by

$$x_N(t) = 3(t - s_N(t))e^{-2s_N(t)/3}. \tag{3.22}$$

Figure 3.4 shows the relationship between $x_N(t)$ and t on logarithmic scales for three different flows supplied with an exponentially decaying flux, steady flux or an instantaneous release of a constant volume. In the limit of small time, $t \ll 1$, the flow from an exponentially decaying flux resembles the flow from a steady flux. The flow extent increases linearly with time, as predicted by (3.19) with $\alpha = 1$. In the limit of large time, $t \gg 1$, the flow from an exponentially decaying flux resembles the flow following an instantaneous release of a constant volume of fluid, $q = \delta(t)$, where δ is the Dirac delta function. The flow extent scales like $t^{1/3}$, as predicted by (3.19) with $\alpha = 0$.

Equation (3.22) along with the corresponding curve of x_N in Figure 3.4 is welcoming for describing lava flows supplied with an exponentially decaying effusion rate. Unlike the method of seeking similarity solutions, which is unable to describe the flow at intermediate time scales when $t \sim 1$, the method presented here allows the extent of the flow to be determined at all times.

3.4.3 Oscillating flux

Here, we study the effects on the resultant flow of perturbing a constant flux of fluid at the source. Consider a source flux given by

$$q(t) = 1 + \beta \sin t, \tag{3.23}$$

where $\beta < 1$ is the amplitude of the perturbation.

No internal shock forms in the current at early times. The condition of no shock (3.14) is satisfied when $t - s_N \ll 3/2\beta$, which reduces to $t \ll 9/2\beta$ because $s_N \sim 2t/3$ and $x_N \sim t$ to leading order.

If $\beta \ll 1$, then the source flux may oscillate with small amplitude many times without producing internal shocks behind the front of the current. In that case, we obtain

$$s_N = \frac{2t}{3} + \frac{\beta}{3}\left(\frac{2t}{3}\sin\frac{2t}{3} + \cos\frac{2t}{3} - 1\right) + O(\beta^2). \tag{3.24}$$

The front of the current is given by

$$x_N = t + \beta\left(1 - \cos\frac{2t}{3}\right) + O(\beta^2). \tag{3.25}$$

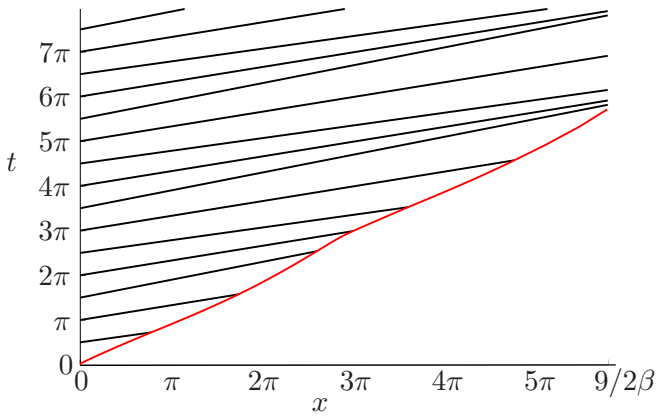

Figure 3.5: *Representative characteristic lines plotted in the (x,t) plane, where q is given by (3.23) with $\beta = 1/4$. The red line represents the position of the front of the current.*

Equation (3.25) indicates that the the front of the current oscillates at the same amplitude as that of the flux at the source. The frequency of the oscillating front of the current is 50% larger than that of the oscillating flux at the source. The speed of the front takes longer to complete a periodic cycle than the source flux because the front of the current is moving away from the source.

A representative plot of the characteristic lines is shown in figure 3.5 for the case of an oscillating flux of the form (3.23) with a specific value of $\beta = 1/4$. The position of the front is given by (3.9), where s_N is computed using a built-in Matlab function, ode15s, by solving (3.13) subject to the initial value $s_N = 0$ at $t = 0$. Characteristic lines are given by (3.8) with s taking values which are multiples of $\pi/2$. The lines leaving the source at s near $2n\pi$, with integer n, approach each other downstream because the temporal gradient of the flux at the source is maximal at time $2n\pi$. The lines leaving the source at s near $(2n+1)\pi$ move slowly away from each other downstream.

At large times, $t \gg 9/2\beta$, internal shocks form behind the front of the current at $x \sim 9/2\beta$. Characteristic lines leaving the source near $s = 2n\pi$ intersect each other as implied in figure 3.5 and sketched in figure 3.6. The internal shocks do not coalesce downstream because the flux at the source is 2π-periodic in time. At any given position down the point where internal shocks form, a shock arrives periodically with the same speed. The exact evolution of each internal shock and the characteristic lines truncated at the shock in the (x,t) plane remain a challenge to compute. Instead, an asymptotic analysis at large times is presented below to highlight the salient features of internal shocks.

The advancing speed of internal shocks is given by

$$\frac{q(2n\pi+\delta_+) - q(2n\pi-\delta_-)}{q(2n\pi+\delta_+)^{1/3} - q(2n\pi-\delta_-)^{1/3}}, \tag{3.26}$$

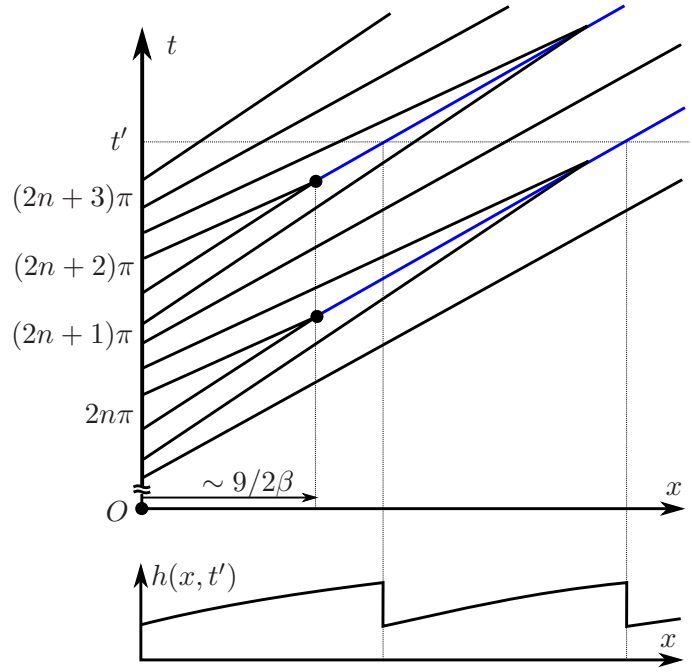

Figure 3.6: *The top sketch shows characteristic lines along which the thickness of the flow remains constant in the (x,t) plane, where q is given by (3.23). At large times, internal shocks form at a distance* $\sim 9/2\beta$ *away from the source and propagate along the blue curves. The thickness of the flow at time* t' *is sketched at the bottom.*

where $2n\pi \pm \delta_\pm$ correspond to the maximum and minimum values of s such that h is constant along the characteristic line given by (3.8), with x representing the shock position. By considering $x = x_N \sim t$ and $s = 2n\pi \pm \delta \sim 2t/3$, and considering the slope of the characteristic lines that reach the front of the current at time t, we determine $\delta_\pm \sim \pi - 27\pi/4\beta t$. Substituting $\delta_\pm$ into (3.26) we deduce that each internal shock moves approximately three times faster than the speed of the front. When an internal shock arrives at the front of the current, the thickness of the front increases instantaneously from $1 - 9\pi/2t$ to $1 + 9\pi/2t$ and the speed of the front from $1 - 9\pi/2t$ to $1 + 9\pi/2t$. Otherwise, the thickness and the speed of the front decrease extremely gently for a period of 3π. Note that as $t \to \infty$, $x_N \to t$ so surface deformations decay at large times. Internal shocks may diminish more quickly by effects due to surface tension and flow driven by a hydrostatic pressure gradient, which were neglected.

3.5 Conclusion

A general theory has been developed to predict flows supplied at a prescribed rate down a rigid slope. For any given flux $q(t)$ at the origin, both the profile of the thickness and the position of the front of the current can be determined by the method of characteristics.

The profile of the thickness of the flow is given by (3.10), where $s(x,t)$ satisfies (3.8). The extent of the flow is given by (3.12), where $s_N(t)$ satisfies (3.31).

The theory has been applied to specific examples, where the prescribed flux at the source is given. The techniques developed here could be helpful particularly for studying flows driven by gravity in geophysical contexts, where the flux of fluid at the source may vary with time in a non-trivial manner.

Appendix 3.A Alternative formulation

The governing equations (3.12) and (3.13) can be obtained alternatively as follows. First, we introduce the area of fluid on the slope at any given time t,

$$A(t) = \int_0^{x_N(t)} h(x',t)\,dx', \tag{3.27}$$

which is equal to the cumulative flux from the origin,

$$A(t) = \int_0^t q(t')\,dt'. \tag{3.28}$$

By differentiating both (3.27) and (3.28) and equating, we immediately obtain (3.12).

The evolution equation for (3.13) can be obtained by further steps as follows. By substituting (3.10) into (3.27) and representing the thickness of the fluid as a function of t and s rather than t and x, the area of the fluid can be expressed alternatively as

$$A(t) = \int_t^{s_N(t)} h(0,s)\frac{\partial x}{\partial s}\,ds, \tag{3.29}$$

where

$$\frac{\partial x}{\partial s} = 2(t-s)q^{-1/3}(s)\frac{dq}{ds} - 3q^{2/3}(s) \tag{3.30}$$

is obtained by differentiating (3.8) with respect to s, keeping t fixed. Integrating (3.29) by parts, using (3.6) and equating with (3.28), we obtain an equation for $s_N(t)$,

$$\int_0^{s_N(t)} q(t')\,dt' = 2(t-s_N(t))q[s_N(t)]. \tag{3.31}$$

Differentiating (3.31) gives (3.13) as required.

Appendix 3.B General case

Materials flowing down a slope are generally described by a kinematic wave equation of the form

$$\frac{\partial h}{\partial t} + k\frac{\partial h^n}{\partial x} = 0, \tag{3.32}$$

where

$$q = kh^n \tag{3.33}$$

is the downstream flux that is prescribed at the source, $x = 0$. For dense granular flow down a rough slope, $n = 5/2$ and k is proportional to $\sqrt{g}/h_{\rm stop}$, where $h_{\rm stop}$ is the thickness of the layer that is naturally deposited on the slope (Pouliquen, 1999). For glacial flow, n is approximately 3 to 7/2 (Nye, 1960). For a non-Newtonian flow with a power-law rheology, $n = 2 + 1/m$ and $k = m\left(\rho g \sin\theta/\mu_m\right)^{1/m}/(1+2m)$, where m is the flow index and μ_m is the viscosity coefficient (Whitham, 1974). The special limit of $m = 1$ corresponds to a Newtonian fluid, $0 < m < 1$ a shear-thinning fluid and $m > 1$ a shear-thickening fluid.

The evolution equations for x_N and s_N,

$$\frac{dx_N}{dt} = k^{1/n} q(s_N)^{1-1/n} \tag{3.34}$$

and

$$\frac{ds_N}{dt} = \frac{(n-1)q(s_N)}{nq(s_N) - (n-1)(t-s_N)[dq/ds]_s = s_N}, \tag{3.35}$$

are obtained by the same methods as before. The choice of n and k may affect the quantitative details but should not change the qualitative features of materials supplied at a time-dependent rate down a slope, as investigated here for Newtonian flows.

Chapter 4

Pouring viscous fluid out of a tipped container

4.1 Abstract

Emptying a container partially filled with viscous fluid can be a frustratingly slow process. Tipping the container develops a draining film on the interior surface and allows the fluid to pour out slowly. The time required for the fluid to begin discharging is predicted theoretically in two simple geometries and compared with experiments. At subsequent times, the volume of the fluid yet to be discharged is predicted to scale with time like $t^{-1/2}$ or t^{-1} for flow driven along a plane or corner respectively. We discuss how fluid pours out most quickly, keeping the size of the system fixed, by tipping a container of equal height and width at 45^o to the horizontal and directing the flow along a right-angled corner.

4.2 Introduction

Viscous fluids in a wide range of contexts are stored and transported in containers. Bottles of shampoo, buckets of detergent, cans of paint, jars of honey and tanks of oil represent frequent examples in the cosmetic, cleaning, coating, food and petroleum industries respectively. One of the simplest and most common methods of retrieving fluids from containers is by tipping. However, the process can be slow, particularly when there is little fluid remaining in the container. The difficulty of dispensing viscous fluids completely from containers is associated with the development of a thin film coating on the interior surface.

Relevant problems involving thin films have been studied extensively. The drainage on a vertical plate (Jeffreys, 1930) and scraping a viscous fluid on a plane surface (Taylor, 1962) are pioneer problems. At smaller scales, where effects due to surface tension play an important role, the rise of a bubble inside a capillary tube (Bretherton, 1961) and the film that is left behind as a viscous fluid is blown from an open-ended tube (Taylor, 1961) are relevant. Further examples of thin films have been studied and reviewed (Ruschak, 1985; Oron *et al.*, 1997; Batchelor *et al.*, 2000).

The objective here is to determine the optimal shape and tipping angle of a container which maximises the cumulative proportion of fluid retrievable at any given time. There are practical benefits of minimising the time required to retrieve the first drip of fluid. Furthermore, there are economic advantages to minimising the remaining fluid in the container, which is usually disposed as waste. We study how a desirable proportion of fluid can be poured out in the shortest possible time.

In section 4.3, we consider tipping a rectangular container partially filled with Newtonian fluid. The fluid eventually pours out of an edge of the container as investigated theoretically. In section 4.4, we consider pouring fluid out of a corner of a different container in order to study the effects of the geometry. Theoretical predictions for the time required to begin discharging after tipping the container, and the subsequent decrease in volume of fluid remaining in the container, are compared with experiments in section 4.5. The implications of the current study are discussed in section 4.6.

4.3 Flow out of an edge

Consider a rectangular container of vertical height H, width W and breadth B, partially filled with viscous fluid of volume $V_0 \ll HWB$. A corner on the base is represented by the origin, where the x axis initially points vertically and the y and z axes extend horizontally

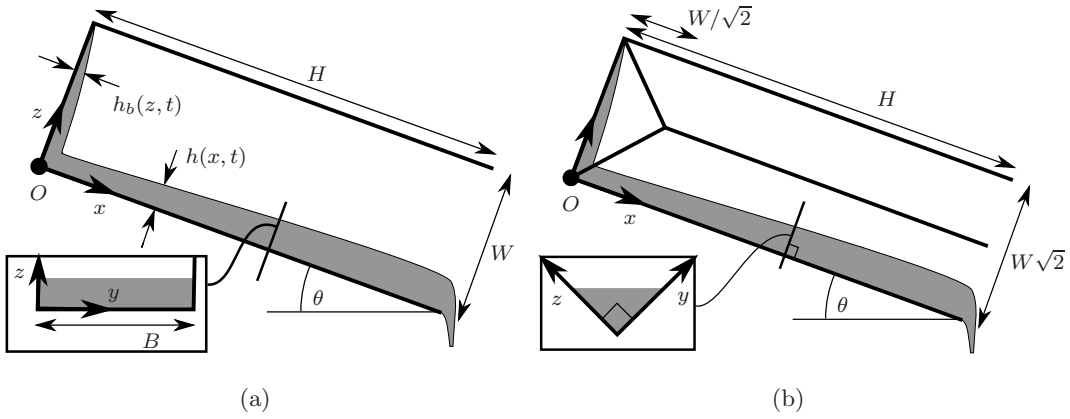

Figure 4.1: *Sketch of a tipped container of rectangular cross-section such that the bulk flow is along two planes (left) and a square container with a wedged base such that the flow is along two corners. Each inset figure shows a cross-section of the flow.*

along the breadth and width respectively. When the container is rotated rapidly about the y axis and tipped at an angle θ beyond the horizontal, the fluid is driven by gravity and eventually pours out of the container, as sketched in figure 4.1(a). The flow inside the container is primarily in the direction of the $-z$ axis followed by the x axis, provided that effects due to walls confining the current and the upstream end of the flow on the base are negligible.

When the fluid thickness is much smaller than any length scale of the container, the volumetric flow rate per unit cross-stream width is given by $q = g_* h^3/3\nu$, where g_* is the component of gravity g along the flow, h the flow thickness and $\nu = \mu/\rho$ the kinematic viscosity of the fluid (Batchelor, 2000). This holds provided that effects due to fluid inertia and surface tension are neglected in the dynamical regime of low Reynolds number $Re = UL/\nu$ and high Bond number $Bo = \rho g L^2/\sigma$, where ν is the viscosity, ρ is the density, σ is the surface tension, U is a characteristic scale for the velocity and L is a suitable length scale of the flow. The relevant dimensionless parameters are

$$Re = \frac{g V_0^3}{W^3 B^3 \nu^2} \ll 1 \tag{4.1}$$

and

$$Bo = \frac{\rho g B^2}{\sigma} \gg 1, \tag{4.2}$$

where $V_0/(WB)$ is the initial thickness of fluid and sets the viscous length scale and B is the cross-flow length scale relevant to the Bond number.

The local conservation of mass in the $-z$ direction, $\partial h/\partial t - \partial q/\partial z = 0$, subject to the approximate condition that the film thickness is negligible after the fluid has drained

sufficiently at $z = W$, is solved using the method of characteristics (Whitham, 1974) to obtain the fluid thickness on the base of the container,

$$h_b(z,t) = \left(\frac{\nu(W-z)}{g\cos\theta\, t}\right)^{1/2}. \tag{4.3}$$

The solution (4.3) holds provided that the plane forming the base is not too deviated from the vertical such that the fluid drains without dripping, as considered further in the Appendix. The fluid thickness along the x axis,

$$h(x,t) = \left(\frac{\nu(x + W\tan^{1/3}\theta)}{g\sin\theta\, t}\right)^{1/2}, \tag{4.4}$$

is obtained by conserving mass in the x direction, $\partial h/\partial t + \partial q/\partial x = 0$, subject to the condition that the flow rate is continuous in the limits as $z \to 0$ and $x \to 0$. The region at the corner, where the flow is two-dimensional and possibly influenced by capillary effects, is small based on the assumption that the film thickness is much smaller than any length scale of the container. The neglect of this small region is justified by the agreement between the theory and the experiments. Note that the fluid thickness along the x axis is equivalent to that on an inclined plane where the fluid is released at a virtual origin, $x_0 = -W\tan^{1/3}\theta$.

The front of the current reaches the open end of the container at time $\bar{T}$, which is determined by the condition $\int_0^H h(x,\bar{T})\,dx + \int_0^W h_b(z,\bar{T})\,dz = V_0/B$. The front of the current remains stable before this time as long as it travels a distance less than a critical length proportional to $(V_0/B)^{1/2}$ (Huppert, 1982b). The fluid begins to pour out of a flat edge after a dimensionless time

$$\bar{T}\left(\frac{\nu B^2 H^{3/2} W^{3/2}}{g V_0^2}\right)^{-1} = \frac{4}{9\sin\theta}\left(a^{1/2} + a^{-1/2}\tan^{1/3}\theta\right)^3, \tag{4.5}$$

where $a = H/W$ is the aspect ratio of the container. The expression in brackets on the left hand side is a time scale of the problem and is reduced by swapping the values of B and W if $B > W$, suggesting that the discharge of fluid from a given container is enhanced by directing the flow on a plane of minimal area. For a given container of aspect ratio a, the dimensionless function on the right hand side of (4.5) attains a minimum at $\theta = \arctan(a^{3/7})$. A global minimum of $2^{11/2}/3^2$ is attained at $a = 1$ and $\theta = \pi/4$, indicating that fluid is retrieved most rapidly, holding all quantities other than a and θ fixed, from a container of identical height and width and tipping it at 45^o to the horizontal.

Once the fluid has started to pour out, the volume of the fluid remaining on the interior

planes of the container is given by

$$\bar{V} = V_0(t/\bar{T})^{-1/2}. \tag{4.6}$$

Note that $\bar{T} \sim V_0^{-2}$ so the functions $\bar{V}(t)$ for different V_0 fall on a curve, independent of V_0 for times $t > \bar{T}$. The volume of the fluid yet to be discharged scales like the flow thickness and evolves with time like $t^{-1/2}$ because the characteristic width of the flow remains steady in time. A different scaling is expected when the width, in addition to the thickness of the flow, varies as demonstrated in a container of different shape.

4.4 Flow out of a corner

Consider a configuration where fluid drains from a container such that the bulk flow is along a wedge. This can be set up, for example, using a square container of vertical height H and width W with a right-angled corner constructed along a diagonal of the base. Figure 4.1(b) shows flow along two successive channels of V-shaped cross-section, which arises after tipping the tank initially filled with a small volume of fluid V_0. The free surface remains approximately flat across the flow as the fluid depth declines in time, provided that the contact line recedes over a time scale shorter than the time scale associated with the main flow. The volumetric flow rate along a wedge is given by $Q_x = Kg_*h^4/\nu$, where K is a dimensionless function of the angle at the vertex that attains a maximum of $K \approx 0.68$ when the wedge is right-angled (Takagi & Huppert, 2007). The relevant length scale for both the Reynolds number and the Bond number is given by the initial thickness of the fluid, which scales like $(V_0/W)^{1/2}$. This means that the dynamical regime of interest is characterised by

$$Re = \frac{gV_0^{3/2}}{W^{3/2}\nu^2} \ll 1 \tag{4.7}$$

and

$$Bo = \frac{\rho g V_0}{W\sigma} \gg 1. \tag{4.8}$$

The fluid begins to pour out of a corner at dimensionless time

$$\check{T}\left(\frac{\nu HW}{gV_0}\right)^{-1} = \frac{1}{4K\sin\theta}\left(a^{1/2} + a^{-1/2}\sqrt{2}\tan^{1/2}\theta\right)^2, \tag{4.9}$$

which is obtained using the same methods as before in section 4.3. The time $\check{T}$ required for the fluid to reach the end of the corner and begin discharging after tipping the container scales like ϵ^{-1}, where $\epsilon \ll 1$ is defined as the proportion of the container initially occupied by the viscous fluid, V_0/V_c, with $V_c = W^2(H - W/3\sqrt{2})$. The time is shorter than $\bar{T}$,

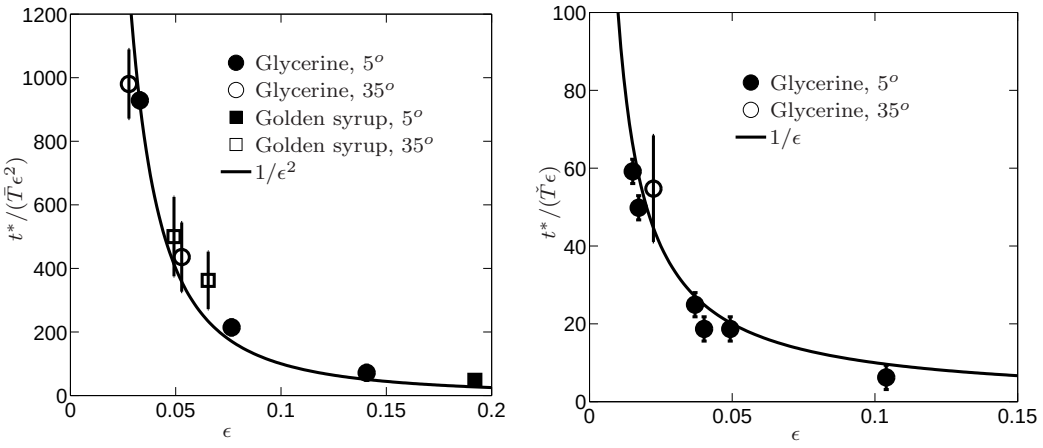

(a) (b)

Figure 4.2: *Rescaled time when fluid begins to pour out of a flat edge of a square container (left) and a corner of a square container with a wedged base (right), plotted against the proportion of the container initially occupied by the fluid.*

the corresponding time for the same fluid along a flat edge of a rectangular container of similar dimensions, which scales like ϵ^{-2} in (4.5). The volume of the fluid remaining inside corners is either V_0 for $t \leq \check{T}$ or

$$\check{V} = V_0(t/\check{T})^{-1} \tag{4.10}$$

for $t > \check{T}$. At large times, the volume of the fluid remaining along the corners decreases more rapidly than that along flat edges of a rectangular container.

4.5 Experiments

Experiments were conducted to test the theoretical predictions of the time required for the fluid to begin discharging and the subsequent decline in the volume of the fluid remaining inside different containers. A perspex tank of height $H = 300\,\text{mm}$ with a square cross-section of width $W = 100\,\text{mm}$ was initially vertical and partially filled with different volumes of either glycerine of viscosity $\nu = 890 \pm 30\,\text{mm}^2/\text{s}$ or golden syrup of viscosity $\nu = 38000 \pm 8000\,\text{mm}^2/\text{s}$, the uncertainty attributed to fluctuations in room temperature $20.5 \pm 1\,\text{C}^o$. The viscosities were measured using U-tube viscometers. A right-angled corner was constructed along a diagonal of the base by inserting a pair of aluminium plates, as required. The tank was rapidly tipped at either $\theta = 5$ or 35^o to the horizontal and held fixed on clamp stands. Any fluid discharged from the tipped container was collected inside a beaker on a weight balance. The mass of the discharged fluid was recorded to an accuracy of 0.1 g every third of a second approximately.

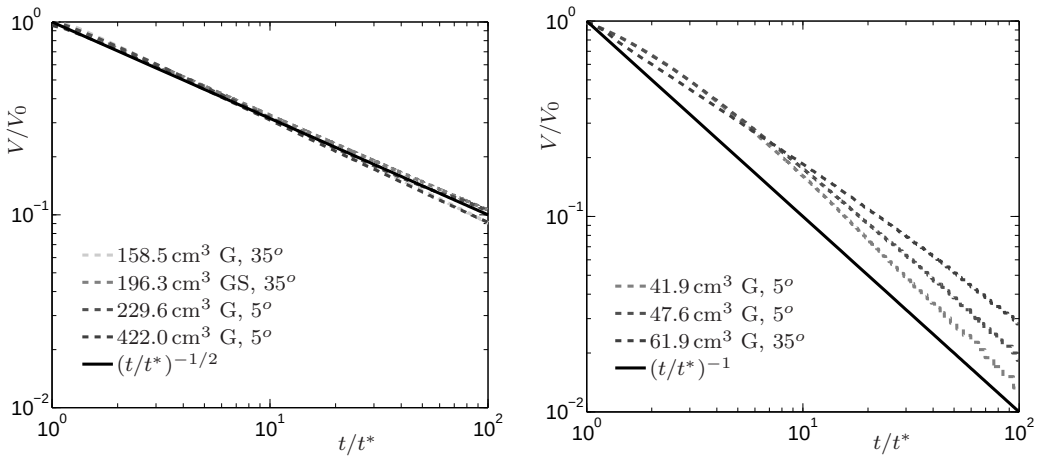

(a) (b)

Figure 4.3: *Proportion of glycerine (G) and golden syrup (GS) remaining along flat edges of a square container (left) and corners of a square container with a wedged base (right), plotted on logarithmic scales against rescaled time.*

Figure 4.2(a) shows the interval t^* between the moment when the container is rapidly tipped and when the fluid starts discharging from a flat edge of the tank, as a function of the proportion of the container initially occupied by the fluid, $\epsilon = V_0/V_c$, where $V_c = W^2H$. The interval is rescaled by $\bar{T}\epsilon^2$, which is independent of the fluid volume. Figure 4.2(b) shows the corresponding plot of the time, rescaled by $\check{T}\epsilon$, required for the fluid to begin discharging from a corner of the tank with a wedged base, where $V_c = W^2(H - W/3\sqrt{2})$. In both cases, the experimental data agree with the theoretical predictions of the dimensionless times, which scale like ϵ^{-1} and ϵ^{-2} depending on the geometry.

Figure 4.3(a) shows the proportion of fluid discharged out of an edge in different experiments, conducted by varying the tipping angle, the initial volume and the viscosity of the fluid. The fluid pours out in the form of threads and then droplets, the details of which do not influence the bulk flow inside the container, as suggested by the excellent agreement between the theoretical curve and the experimental data. The collapse of experimental data onto the theoretical line of the form (4.6) is also obtained with golden syrup in different containers, including a perspex tank of circular cross-section and along a corner of a square tank, with and without a wedge on the base. The volume of golden syrup decreases like $t^{-1/2}$ rather than t^{-1} along corners (not shown), possibly because the characteristic width of the flow remains steady. This is attributed to the contact line that appears pinned on the perspex over the time scale of the main flow. The contact line does not recede and maintain a flat free surface across the flow as assumed in the theory.

Figure 4.3(b) shows the remaining proportion of glycerine inside a corner of a square

tank with a wedged base. The experimental data do not collapse onto the theoretical curve, possibly due to effects of the receding contact line and surface tension that are not incorporated into the model. Nevertheless, the volume of glycerine scales approximately like t^{-1} along a corner as predicted, which declines more rapidly than $t^{-1/2}$ on a flat edge of the square container.

4.6 Discussion

The cumulative volume of fluid poured out of a tipped container depends importantly on the shape of the container. A concept of relevance to the problem is the hydraulic radius, a measure of the efficiency of the flow. The hydraulic radius is proportional to the cross-sectional area of the flow divided by the wetted perimeter. The wetted perimeter of the flow down a rectangular channel approaches the width of the channel as the fluid drains. In contrast, the wetted perimeter of the flow down a V-shaped channel is $2\sqrt{2A/\sin\beta}$, where A is the cross-sectional area of the flow and β is the internal angle at the vertex of the channel. As A decreases sufficiently with time, the resistive forces acting on the wetted perimeter are minimised by setting $\beta = \pi/2$. This indicates that a right-angled wedge, amongst the shapes considered here, is the optimal shape of the channel which allows fluid of ever-thinning depth to be transported most efficiently. This holds provided that the free surface of the flow is flat across the channel, as expected when the contact line recedes rapidly.

Considerable variations in the elevation of the free surface may arise across the channel, for example due to effects of the contact line pinning on the sides of the channel. The effects of the contact line on the bulk flow down a wide rectangular channel are negligible. However, the effects may significantly influence the bulk structure of the flow down a wedge. This is consistent with the observation that the agreement between the simplified theory and the experiments for flow down a wedge is not as good as for flow down a rectangular channel.

Appendix 4.A Draining and dripping of a thin film under an inclined plane

The condition for fluid to drain and not drip inside a tipped container is estimated as follows. First, component of the momentum equation along a plane inclined at angle θ to the horizontal is given by

$$-\frac{\partial p}{\partial x} + \rho g \sin\theta + \mu \frac{\partial^2 u}{\partial z^2} = 0, \tag{4.11}$$

where x is down the slope and z is normal to the slope. Imposing the boundary conditions that $u = 0$ on $z = 0$ and $\partial u/\partial z = 0$ on $z = h$, we obtain the velocity profile

$$u = \frac{\rho g \sin\theta - \partial p/\partial x}{2\mu} z(2h - z), \tag{4.12}$$

where

$$\frac{\partial p}{\partial x} = -\rho g \cos\theta \frac{\partial h}{\partial x} - \gamma \frac{\partial^3 h}{\partial x^3} \tag{4.13}$$

and γ is the surface tension. The depth-integrated version of mass conservation, $\partial h/\partial t + \int_0^h u\, dz = 0$, leads to a nonlinear partial differential equation,

$$\frac{\partial h}{\partial t} + \frac{g \sin\theta}{3\nu} \frac{\partial h^3}{\partial x} + \frac{g \cos\theta}{3\nu} \frac{\partial}{\partial x}\left(h^3 \frac{\partial h}{\partial x}\right) + \frac{\gamma}{3\mu} \frac{\partial}{\partial x}\left(h^3 \frac{\partial^3 h}{\partial x^3}\right) = 0. \tag{4.14}$$

In order to study the possible Rayleigh-Taylor instability of the fluid, we conduct a linear stability analysis by seeking normal mode solutions of the form

$$h = h_0 \left(1 + \epsilon e^{\sigma t + ikx}\right), \tag{4.15}$$

where $\epsilon \ll 1$. By substituting (4.15) into (4.14) and linearising, we obtain the growth rate

$$\sigma = \frac{g \cos\theta h_0^3}{3\nu} k^2 - \frac{\gamma h_0^3}{3\mu} k^4 \tag{4.16}$$

for each wave number k. The most unstable mode,

$$k_{\max} = \sqrt{\frac{\rho g \cos\theta}{2\gamma}}, \tag{4.17}$$

is obtained by setting $d\sigma/dk = 0$. The associated growth rate is given by

$$\sigma_{\max} = \frac{\rho^2 g^2 \cos^2\theta h_0^3}{12\mu\gamma}. \tag{4.18}$$

The time scale of dripping is

$$T_{\text{drip}} \sim \frac{1}{\sigma_{\max}} \sim \frac{\mu\gamma}{\rho^2 g^2 \cos^2\theta h_0^3} \sim \frac{\nu L^2}{g \cos\theta h_0^3}. \tag{4.19}$$

The time scale of draining is

$$T_{\text{drain}} \sim \frac{\nu L}{g \sin\theta h_0^2}, \tag{4.20}$$

where L is the length of the inclined plane. There is no dripping provided that $T_{\text{drain}} \ll$

T_{drip}. This reduces to the condition that a film of thickness

$$h_0 \ll \frac{\gamma \sin\theta}{L\rho g \cos^2\theta} \tag{4.21}$$

inside a container tipped at angle $\pi/2-\theta$ beyond the horizontal is linearly stable and does not drip. Identifying the exact condition for the film not to drip requires further work to study the nonlinear regime, where the Rayleigh-Taylor instability may saturate by effects due to flow shear and surface tension (Babchin *et al.*, 1983). Nevertheless, the simple scaling analysis presented here captures the basic idea that fluid drains without dripping on the base of the container provided that the tipping angle beyond the horizontal is small.

Chapter 5

Flow and instability of thin films on a cylinder and sphere

5.1 Abstract

We investigate the dynamics of thin films driven by gravity on the outer surface of a cylinder and sphere. The surface is rigid, stationary and the axis of the cylinder horizontal. An instantaneous release of a constant volume of fluid at the top of the cylinder or sphere results initially in a two-dimensional or axisymmetric current respectively. The resultant flow of a thin film of fluid is described using lubrication theory when gravity and viscous forces govern the dynamics. We show that the thickness of the flow remains uniform in space and decreases in time like $t^{-1/2}$ near the top of both the cylinder and sphere. Analytic solutions for the extent of the flow agree well with our experiments until the advancing front splits into a series of rivulets. We discuss scalings of the flow at the onset of the instability as a function of the Bond number, which characterises the relative importance of gravity and surface tension. The experiments, conducted within an intermediate range of Bond numbers, suggest that the advancing front becomes unstable after

it has propagated a critical distance, which depends primarily and monotonically on the volume of fluid and not on the viscosity of fluid. Releasing a sufficiently large volume of fluid ensures that rivulets do not develop on either a cylinder or sphere.

5.2 Introduction

Many problems in industrial and natural settings involve the flow of thin liquid films, some of which are driven by gravity on a rigid surface (Oron *et al.*, 1997). These include the application of coatings on manufactured products and the spreading of sauce on food. A naturally occurring example is the flow of water on stalactites that hang from the ceilings of limestone caves (Short *et al.*, 2005). At larger scales, the ascent of buoyant magma below solid rocks and the spreading of lava on volcanoes are further examples of geological problems. The recurring feature in all these examples is that fluid is in contact with, and driven along, a rigid boundary due to the action of gravity. Effects due to inertia are negligible in the bulk region of the flow, where gravity and viscous forces dominate.

The flow of thin films driven by gravity has received considerable attention within the scientific community largely because the leading edge of the flow gives rise to the fascinating phenomenon of a fingering instability. Laboratory experiments have shown that a thin film of Newtonian fluid flowing down an inclined plane can become unstable at the front and split into a series of rivulets (Huppert, 1982b; Silvi & Dussan, 1985). Rivulets develop in a similar manner when a thin film is driven by a centrifugal force (Melo *et al.*, 1989; Fraysse & Homsy, 1994; Wang & Chou, 2001) or by a spatial gradient in surface tension (Cazabat *et al.*, 1990). The instability has been studied by incorporating effects due to surface tension in a small region near the advancing front of the flow, where a capillary ridge develops before splitting into rivulets (Troian *et al.*, 1989; Goodwin & Homsy, 1991). A cross-flow perturbation of the flow front develops thicker regions that advance more rapidly, a possible mechanism of the fingering instability (Spaid & Homsy, 1996). Macroscopic perturbations can be caused by microscopic corrugations in the contact line (Bertozzi & Brenner, 1997), suggesting that minor variations in topography, in addition to thermal effects, may influence the development of candle wax drips and branches of lava flows on volcanoes.

We extend previous studies of thin films to consider driven films featuring a moving contact line on curved surfaces. Lubrication theory has been applied to describe thin films flowing in between curved gaps (Stone, 2005) and on curved substrates with a free surface (Roy *et al.*, 2002). It is fruitful to assess the applicability of the theory to thin films featuring a moving contact line (Davis, 1983), which may not influence the bulk flow. Thin films on the outer surface of a cylinder and sphere are considered as two special

cases where the slope of the substrate changes slowly in the direction of flow (Takagi & Huppert, 2010). The theory is based on the following three conditions. First, the front of the flow is assumed to have extended a distance much longer than the characteristic film thickness. Second, the component of gravity is approximated to increase linearly in the flow direction, which holds near the top of the cylinder and sphere. Third, surface tension is considered to be negligible everywhere except possibly near the leading front of the flow. We examine the effect of a curved substrate on the flow and its possible instability of thin films in two specific cases.

In the first case, we consider the instantaneous release of a constant volume of viscous fluid from a line source at the top of a cylinder. We stress that the cylinder does not rotate about its horizontal axis. The resultant flow is initially two-dimensional; an analytic solution describing its form and extent is obtained in § 5.3 using lubrication theory. Related problems that have been investigated theoretically include thin films on a rotating cylinder (Moffatt, 1977) and steady rivulet flows on a stationary cylinder (Duffy & Moffatt, 1995). We note that once the rotation of the cylinder, or the supply of fluid, has stopped, the film draining at the top of the cylinder is expected to be identical at large times, independent of the initial conditions.

In the second case, we consider the instantaneous release of a constant volume of viscous fluid from a point source at the top of a sphere. The initial spreading of fluid near the source is the axisymmetric counterpart of the two-dimensional flow in our first case. The problem on the sphere falls in the same category of axisymmetric spreading as flow from the top of a cone, which is presented as mathematical exercise 7.12 in the introductory textbook by Acheson (1990). In § 5.4, we develop theoretical results and show that the spreading on a stationary sphere is closely related to spin coating, where a drop of fluid spreads and develops a fingering instability on a rotating plane (Melo *et al.*, 1989; Fraysse & Homsy, 1994; Wang & Chou, 2001). Consequently, the spreading on a sphere is expected to develop a fingering instability at the leading edge in a similar manner to a spinning drop.

In § 5.5, corresponding experiments are reported and shown to agree well with our theoretical predictions until the advancing front splits into a series of rivulets. The rivulets continue to extend until they eventually detach, before they have reached the bottom of the cylinder or sphere. The detachment of fluid from the underside of the cylinder and sphere is similar to dripping from the underside of an inclined plane (Rothrock, 1968; Indeikina *et al.*, 1997). We note that the development of rivulets at the flow front and the detachment of fluid before reaching the bottom prevent the fluid from completely coating the cylinder or sphere.

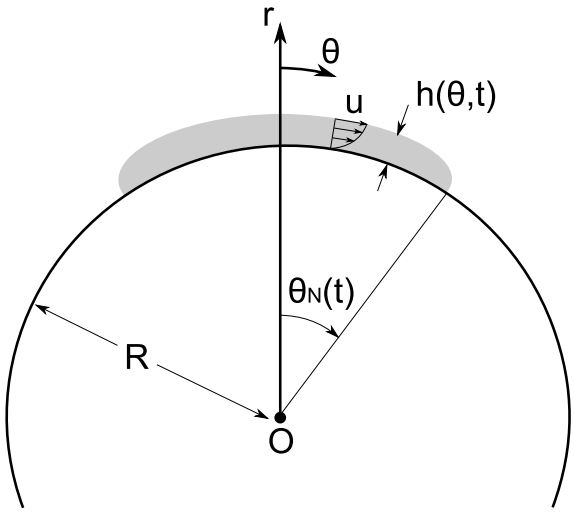

Figure 5.1: *Sketch of a thin film driven by gravity at the top of a cylinder. Flow is denoted to have thickness $h(\theta, t)$ and extend an arc length $R\theta_N(t)$ from the vertical line of symmetry.*

Finally, in § 5.6, the fingering instability at the leading front of the flow is discussed. A scaling analysis of the governing equations suggests that the non-dimensional flow length at the onset of the instability depends on the Bond number of the flow, as defined below. The ideas are partly based on the scalings obtained previously for flow down an inclined plane at a small Bond number (Troian *et al.*, 1989; Goodwin & Homsy, 1991). We obtain approximate conditions at the onset of a fingering instability on a cylinder and sphere in the two limits of small and large Bond numbers. The results suggest that rivulets do not develop on a cylinder or sphere when a sufficiently large volume of fluid is released.

5.3 Two-dimensional flow on a cylinder

A theoretical framework for describing flow on the outer surface of a cylinder of radius R is developed in polar coordinates (r, θ), where $r = R$ represents the surface and the azimuth angle θ is measured from the vertical, as in figure 5.1. We consider the instantaneous release of a constant volume of viscous fluid from a line source at the top of the cylinder such that the resultant flow is initially two-dimensional, independent of the direction normal to the (r, θ) plane. By the vertical line of symmetry, we restrict attention to flow on the right half of the cylinder. A constant cross-sectional area A of fluid is considered to have depth $h(\theta, t)$ and extend an arc length $R\theta_N(t)$ along the surface of the cylinder from the vertical, as shown in figure 5.1.

A long wave approximation is adopted, provided that the fluid depth is much smaller

than its extent,

$$h \ll R\theta_N. \tag{5.1}$$

The approximation is expected to hold soon after the fluid is released on a cylinder of sufficiently large radius R. Since flow is predominantly tangential to the surface of the cylinder, the pressure in the fluid is given by

$$p = p_0 + \rho g(R + h - r)\cos\theta - (\gamma/r^2)\partial^2 h/\partial\theta^2, \tag{5.2}$$

where ρ is the density of fluid, g gravity, p_0 atmospheric pressure and γ surface tension. The θ-component of the momentum equation is given by

$$\nu\partial^2 u/\partial r^2 = (1/\rho r)\partial p/\partial\theta - g\sin\theta, \tag{5.3}$$

where ν is the kinematic viscosity of the fluid and u is the θ-component of the flow velocity. The pressure given by (5.2) remains approximately uniform in the bulk region of the flow given the following two conditions. First, the depth of fluid must vary slowly along the substrate and satisfy

$$\partial h/\partial\theta \ll R\tan\theta. \tag{5.4}$$

Condition (5.4) is expected to hold everywhere except possibly near the flow front and ensures that contribution to (5.3) from the $\rho g(R + h - r)\cos\theta$ term on the right hand side of (5.2) is negligible. The solution to be obtained for small θ indeed satisfies (5.4). Second, effects due to surface tension must be small everywhere except possibly near the flow front, requiring that the final term of (5.2) does not play a role in the equation of motion given by (5.3). By comparing the magnitude of the first and second terms on the right hand side of (5.3), we obtain the corresponding condition

$$\gamma\,\partial^3 h/\partial\theta^3 \ll \rho g R^3 \sin\theta. \tag{5.5}$$

Importantly, we note that the bulk structure of the flow is relatively unaffected by the specific dynamics of the small region near the flow front (Huppert, 1982b; Troian *et al.*, 1989). Under these conditions, the bulk region of the flow is governed primarily by viscous forces and the component of gravity along the flow. The solution satisfying (5.3) with the first term on the right hand side neglected, along with the no-slip condition on the rigid surface and vanishing tangential stress on the free surface, is given by

$$u = \frac{1}{2}y(2h - y)g\sin\theta/\nu, \tag{5.6}$$

where $y = r - R$ is the radial coordinate measured from the surface of the cylinder. The velocity profile is parabolic in y and identical to that arising on an inclined plane with a

constant slope θ to the horizontal (Huppert, 1982b). The local flow on a sufficiently large cylinder does not experience the curvature in the substrate. The depth-integrated velocity of the flow,

$$Q = \int_0^h u \, dy, \tag{5.7}$$

does not depend on the curvature of the substrate, R.

The governing equations for the unknown free surface $h(\theta, t)$ are formulated by conserving the mass of fluid, both locally and globally. Substituting (5.6) into (5.7) followed by the local conservation of mass in cylindrical polar coordinates, $\partial h/\partial t + R^{-1}\partial Q/\partial\theta = 0$, we obtain

$$\frac{\partial h}{\partial t} + \frac{g}{3\nu R}\frac{\partial}{\partial\theta}(\sin\theta h^3) = 0. \tag{5.8}$$

The total cross-sectional area of fluid is independent of time and expressed as

$$A = R\int_0^{\theta_N(t)} h(\theta, t)\, d\theta, \tag{5.9}$$

which ensures that mass is conserved globally. This completes the formulation of the problem.

The length and time scales of the flow initially near the top of the cylinder can be determined by considering the scaling factors of the governing equations (5.8) and (5.9). For small θ such that $\sin\theta \approx \theta$ to leading order, the two terms in (5.8) scale as h/t and $gh^3/\nu R$ respectively. Meanwhile, equation (5.9) indicates that $A \sim hx$, where $x = R\theta$ is a characteristic length of the current. The only dimensional groups appearing in the governing equations for h in terms of x and t are therefore $g/\nu R$ and A, provided that x rather θ is used to represent the coordinate along the flow. The equations can be non-dimensionalised by scaling all lengths by

$$L \equiv A^{1/2} \tag{5.10}$$

and time by

$$T \equiv \nu R/gA. \tag{5.11}$$

The radius of the cylinder, R, only appears in the time scale and not in the length scale of the bulk flow.

The system of equations (5.8) and (5.9) is solved near the top region of the cylinder, where $\theta \ll 1$, as follows. Given that the characteristic length and time scales are given by (5.10) and (5.11) respectively, it is natural to seek solutions to (5.8) with $\sin\theta \approx \theta$ of the form

$$h = A^{1/2} f(t/T). \tag{5.12}$$

The function f to be determined is independent of θ because θ does not appear in the scalings of the two terms in (5.8) when $\sin\theta \approx \theta$ or in (5.9), provided that the coordinate along the flow is represented by x rather than θ. By substituting (5.12) into (5.8), we obtain $f' + f^3/3 = 0$, which can be immediately integrated to give

$$f(s) = [3(s+c)/2]^{-1/2} \tag{5.13}$$

for some constant c. If the fluid has uniform thickness h_0 initially when it is released at time $t = 0$, then the starting time is offset by $c = 2(A^{1/2}/h_0)^2/3$ for the similarity form (5.12) to satisfy the initial condition. However, the required offset c is negligible when the initial thickness is not too small, $h_0 > A^{1/2}$, or equivalently when the flow front is close to the top of the cylinder at the time of release of fluid, as was the case in all our experiments. At large times, $t \gg cT$, the solution (5.13) in dimensional form reduces to

$$h(t) = \left(\frac{3R\nu}{2g}\right)^{1/2} t^{-1/2}, \tag{5.14}$$

which indicates that the thickness is independent of θ and decreases with time like $t^{-1/2}$. The subsequent term of order ϵ in the expansion about the leading-order solution (5.14), where $\theta = O(\epsilon)$, is also independent of the spatial coordinate. The solution (5.14) is independent of θ to order ϵ^2 because of the symmetry of the problem.

We note that the solution of uniform film thickness is related to the boundary layer thickness of a stagnation-point flow towards a flat boundary (Acheson, 1990). Both gravity-driven flow near the top of a cylinder and two-dimensional straining flow along the flat boundary increase linearly with distance. It follows by mass conservation that in both cases the thickness of the flow is uniform along the boundary.

The length of the current is obtained by imposing the condition that the total cross-sectional area of fluid is conserved and given by (5.9). By substituting (5.14) into (5.9) and rearranging, we determine the length of the current

$$R\theta_N(t) = \left(\frac{A^2 g}{6R\nu}\right)^{1/2} t^{1/2}. \tag{5.15}$$

We note that the dependence on the amount of fluid released, A, only appears in the expression for the length and not in the expression for the depth of the flow. The flow near the top of the cylinder takes a similarity form and is independent of the initial conditions. By substituting solutions (5.13) and (5.15) into conditions (5.1) and $\theta_N \ll 1$, we determine that the solution for the flow length given by (5.15) is valid for

$$1 \ll t/T \ll R^2/A. \tag{5.16}$$

The first condition, $t \gg T$, ensures that the thickness of the current is small compared to its length. The second condition, $t/T \ll R^2/A$, arises because the solution given by (5.14) is limited to the region near the top of the cylinder.

We now discuss the small region at the flow front, which we have neglected so far. By eliminating time from solutions (5.14) and (5.15), we determine that the flow has a sharp leading front of thickness

$$h_N = A/R\theta_N. \tag{5.17}$$

The unphysically sharp front is expected to be resolved by a thin boundary layer with length scale $l \ll R\theta_N$, which is small under the following conditions. When effects due to surface tension are neglected, lubrication theory breaks down near the front of the current (Goodwin & Homsy, 1991). The velocity normal to the substrate is no longer small in the region at the flow front. In that case, the length of the boundary layer at the front of the current is expected to scale like $l \sim h_N$, which is always smaller than the bulk flow by condition (5.1).

When surface tension plays a role, in addition to viscous forces and gravity, the left and right hand sides of (5.5) are of the same order of magnitude in the region near the flow front. By considering the scaling factors of (5.5), we obtain $l \sim (\gamma h_N/\rho g \sin\theta_N)^{1/3}$, which is consistent with the corresponding scaling for the length scale of the tip of the current down an inclined plane (Huppert, 1982b; Troian *et al.*, 1989). This can be written as

$$l \sim h_N(Ca)^{-1/3}, \tag{5.18}$$

where Ca is a capillary number of the flow in the region near the front given by

$$Ca \equiv \rho g \theta_N h_N^2/\gamma. \tag{5.19}$$

The capillary number measures the relative importance of viscous forces, which are exactly balanced by gravity, compared to surface tension near the flow front. By substituting (5.15) and (5.17) into (5.19), we determine that the capillary number evolves like $t^{-1/2}$. Instead of working with the capillary number, it is convenient to introduce a Bond number defined as

$$Bo \equiv \rho g A^{3/2}/\gamma R, \tag{5.20}$$

which is expressed in terms of input parameters that do not vary in time. By setting l in (5.18) to be much smaller than $R\theta_N$ and eliminating h_N using (5.17), we determine that the region of the flow front influenced by surface tension remains small compared to the bulk flow as long as

$$\theta_N \gg Bo^{-1/5} A^{1/2}/R. \tag{5.21}$$

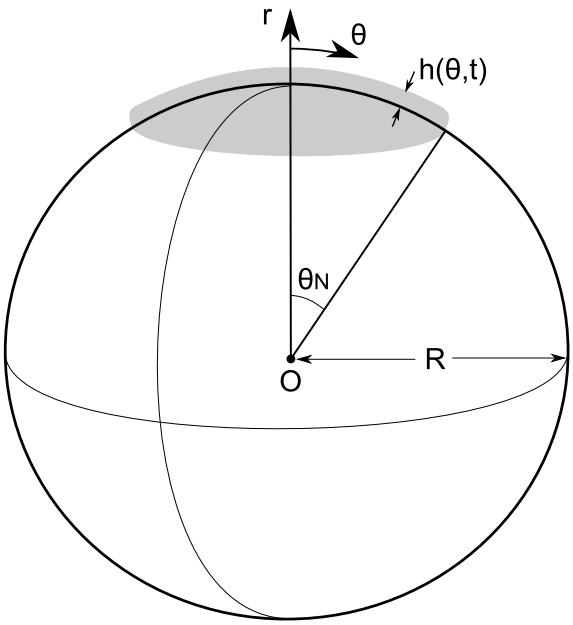

Figure 5.2: *Sketch of a thin film of fluid spreading axisymmetrically at the top of a sphere.*

Equivalently, by substituting (5.15) into (5.21), we obtain

$$t \gg Bo^{-2/5}T \tag{5.22}$$

as the condition when surface tension plays a negligible role in the bulk region of the flow.

In summary, the bulk structure of the flow has uniform thickness given by (5.14) behind an advancing front given by (5.15). The prediction for the flow length is given by (5.15) provided that conditions (5.16) and (5.22) hold. We now present corresponding results for the axisymmetric spreading of fluid at the top of a sphere, before comparing our theoretical predictions with data from laboratory experiments.

5.4 Axisymmetric flow on a sphere

The methods presented in § 5.3 for the two-dimensional flow around a cylinder can be readily applied to the axisymmetric flow on a sphere. Consider the outer surface of a rigid sphere represented by $r = R$ in spherical polar coordinates, where θ is the usual zenith angle from the vertical axis. A constant volume V of viscous fluid is released instantaneously at the top point of the sphere such that the resultant flow is initially axisymmetric as sketched in figure 5.2. When the extent of the flow, denoted by $R\theta_N(t)$, is much greater than the film thickness denoted by $h(\theta, t)$, the flow velocity $u(r, \theta, t)$ is predominantly along the surface of the sphere, in the θ direction. Assuming that conditions

(5.1), (5.4) and (5.5) hold in the bulk region of the flow as in § 5.3, and using lubrication theory as before, we obtain the same velocity profile as for viscous spreading on a cylinder. Thus, the depth-integrated velocity is again given by

$$Q = \frac{1}{3} g \sin\theta \, h^3/\nu. \tag{5.23}$$

Substituting (5.23) into the local mass conservation in spherical polar coordinates given by $\partial h/\partial t + (R\sin\theta)^{-1}\,\partial(\sin\theta Q)/\partial\theta = 0$, we obtain

$$\frac{\partial h}{\partial t} + \frac{g}{3\nu R\sin\theta}\frac{\partial}{\partial\theta}(\sin^2\theta h^3) = 0. \tag{5.24}$$

The total volume of fluid is independent of time and expressed as

$$V = 2\pi R^2 \int_0^{\theta_N(t)} h\sin\theta \, d\theta. \tag{5.25}$$

The governing equations given by (5.24) with $\sin\theta \approx \theta$ and (5.25) can be non dimensionalised by scaling all lengths by

$$L_V \equiv V^{1/3} \tag{5.26}$$

and time by

$$T_V \equiv \nu R/gV^{2/3}. \tag{5.27}$$

The curvature of the substrate only appears in the time scale and not in the length scale of the flow, just like the flow on a cylinder in § 5.3.

The system of equations (5.24) and (5.25) is solved in the region at the top of the sphere, where $\theta \ll 1$, using the same methods as before, to obtain

$$h(t) = \left(\frac{3R\nu}{4g}\right)^{1/2} t^{-1/2}. \tag{5.28}$$

The solution given by (5.28) indicates that the thickness of the bulk structure remains uniform near the top of the sphere. Note that the thickness of fluid on a sphere of radius R given by (5.28) is identical to the thickness of fluid on a cylinder of radius $R/2$, as can be verified using (5.14). The expression (5.28) is also identical to the thickness of a constant volume V of fluid rotated at angular velocity ω about its centre of mass on a plane, where $\omega^2 = g/R$ (Melo *et al.*, 1989). The mathematical reason is that the governing equations for fluid spreading near the top of a sphere, (5.24) and (5.25), where $\sin\theta \approx \theta$ and $g/R = \omega^2$, reduce to corresponding equations for a spinning volume of fluid. Physically, fluids spreading both on the top of a stationary sphere and on the rotating plane experience a body force that increases linearly with distance away from the point of release. The body force is gravity on the sphere or centrifugal on the rotating plane.

By substituting (5.28) into (5.25), we determine that the length of the current is given by

$$R\theta_N(t) = \Big(\frac{4V^2 g}{3\pi^2 R\nu}\Big)^{1/4} t^{1/4}. \tag{5.29}$$

The radius of the leading edge of the flow increases like $t^{1/4}$ as long as effects on the bulk flow due to surface tension are small.

An analysis similar to the previous one indicates that the capillary region, where capillary forces are important near the flow front, is small compared to the bulk flow provided that

$$\theta_N \gg Bo_V^{-1/6} V^{1/3}/R, \tag{5.30}$$

where Bo_V is a Bond number defined as

$$Bo_V \equiv \rho g V/\gamma R. \tag{5.31}$$

The capillary region becomes relatively small after the flow front has extended sufficiently far. By substituting (5.29) into (5.30), we determine that surface tension plays a negligible role in the bulk region of the flow when

$$t \gg Bo_V^{-2/3} T_V. \tag{5.32}$$

The regime of validity of solutions (5.28) and (5.29) is further constrained by

$$1 \ll t/T_V \ll R^4/V^{4/3}, \tag{5.33}$$

which can be investigated experimentally by releasing fluid on a sphere of sufficiently large radius R. The volume of fluid must be sufficiently large that the Bond number is not too small to satisfy (5.32) and sufficiently small that it spreads as a thin film near the top of the sphere to satisfy (5.33).

5.5 Experiments

The theoretical predictions derived in § 5.3 and § 5.4 were tested against a suite of laboratory experiments. In particular, equations (5.15) and (5.29) were compared with flow lengths on a cylinder and sphere respectively. Experimental set ups and results are presented first for flows on a cylinder followed by flows on a sphere.

5.5.1 Flow on a perspex cylinder

A perspex cylinder of radius 15.0 cm and width 11.0 cm was fixed between two parallel and vertical plates, perpendicular to the axis of the cylinder. The cylinder resembled the structure of a wheel, fixed and confined laterally by sidewalls. At the top of the cylinder, a constant volume of either pure glycerine or golden syrup was held behind a removable lock-gate, 2.0 cm away from a rigid and vertical wall. Flow down the outer surface of the cylinder was initiated by a near-instantaneous lift of the gate.

A standard digital camera pointed in the direction parallel to the axis of the cylinder and recorded images of the resultant flow at 15 frames per second. The flow was observed both directly from its side and in plan form through a mirror as shown in the images of figure 3. The flow near the sidewalls was observed to shear laterally with the leading edge of the flow deforming accordingly. This is possibly due to contact line pinning on the sides and the curvature of the substrate, which allows fluid further along the flow to be driven by a larger body force. However, the central region of the flow appeared to be two-dimensional and unaffected by the sidewalls, as indicated by a flat leading front in figure 5.3(b). The flow front, after advancing some distance, split into a pair of rivulets. The rivulets continued to flow as shown in figure 5.3(c) until they reached some extent on the underside of the cylinder, where they dropped as viscous threads (figure 5.3(e)). The point of detachment advanced approximately 5 cm further along the underside of the cylinder and appeared to remain stationary thereafter.

The viscosity and volume of the released fluid were varied in a series of experiments on the cylinder. Representative values of the kinematic viscosity of golden syrup and glycerine were taken to be $\nu = 4.5 \times 10^2\,\mathrm{cm}^2/\mathrm{s}$ and $\nu = 5.1\,\mathrm{cm}^2/\mathrm{s}$ respectively, based on measurements using U-tube viscometers. Although the viscosity of fluid may have fluctuated slightly as a result of minor temperature variations in the laboratory, the flow lengths recorded in every experimental run are relatively insensitive to minor variations in viscosity. The flow length on a cylinder or sphere scales like $\nu^{-1/2}$ in (5.15) or $\nu^{-1/4}$ in (5.29) respectively.

Figure 5.4 shows a plot of non-dimensional flow extents against non-dimensional time on logarithmic scales for different experiments on the cylinder. The data for the initial flow extending with a single front collapse onto the theoretical curve given by (5.15). Minor discrepancies between the theory and experiments conducted by releasing a cross-sectional area $A = 10.5\,\mathrm{cm}^2$ of golden syrup and $A = 5.2\,\mathrm{cm}^2$ of glycerine are attributed to the shear stress on the sidewalls, which may have retarded the flow. Experiments conducted by releasing $A = 4.2\,\mathrm{cm}^2$ and $A = 6.3\,\mathrm{cm}^3$ of golden syrup are in excellent agreement with the theoretical predictions until the front of the flow split into a pair of rivulets. Once

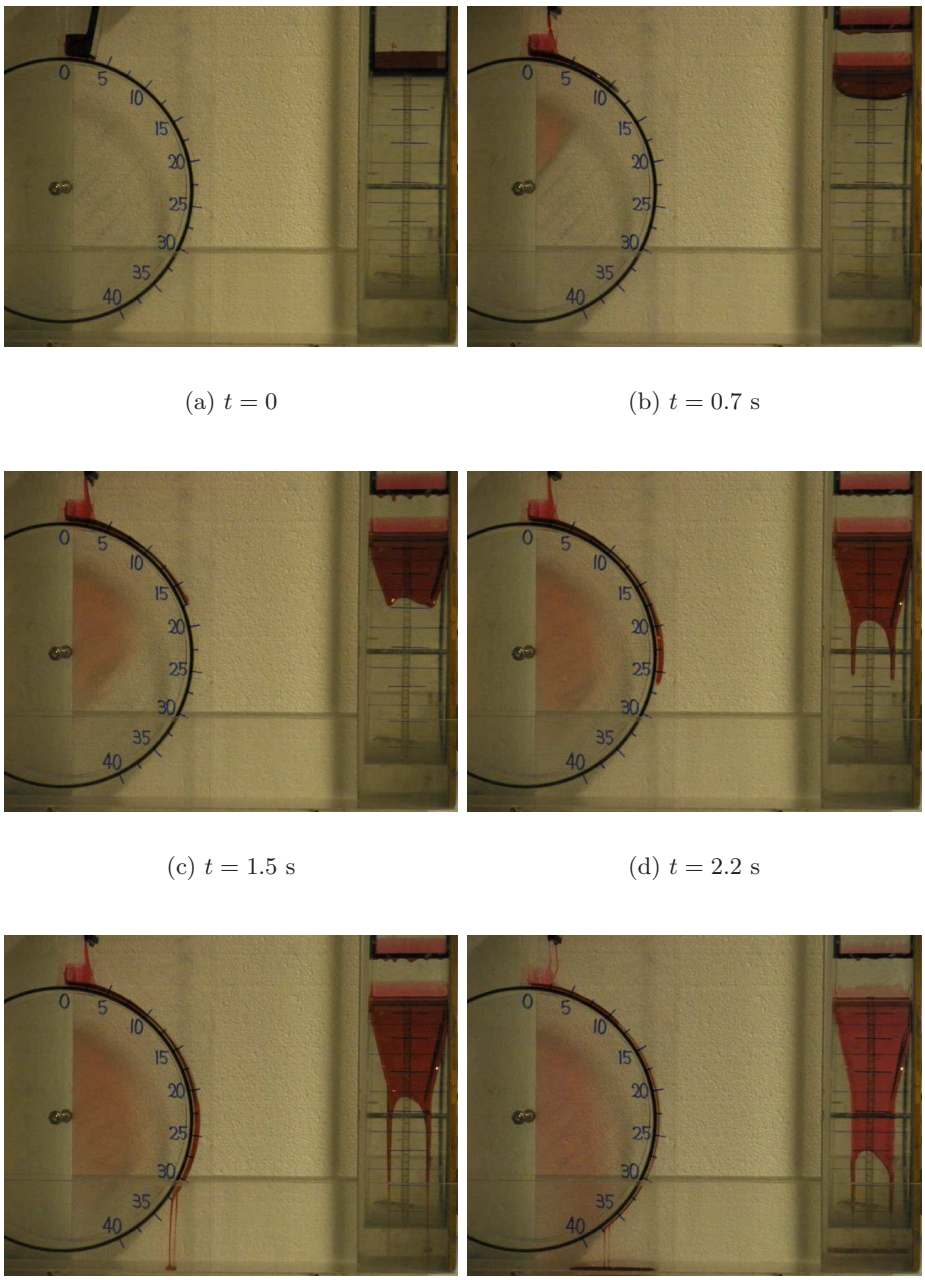

(a) $t = 0$ (b) $t = 0.7$ s

(c) $t = 1.5$ s (d) $t = 2.2$ s

(e) $t = 2.7$ s (f) $t = 30$ s

Figure 5.3: *Sequence of snapshots of an experiment conducted by releasing* $57.5\,\mathrm{cm}^3$ *of pure glycerine on a cylinder, where the resultant flow is viewed directly from the side and in plan form through a mirror on the right. The numbers on the cylinder indicate the perimeter in centimetres from the top of the cylinder. (a) Glycerine is behind the lock-gate, before initiation of the current. (b)* $0.7\,s$ *after release, the bulk flow is approximately two-dimensional, except near the sidewalls confining the flow. (c)* $1.5\,s$ *after release, wave patterns appear at the leading edge of the flow. (d)* $2.2\,s$ *after release, the flow front has split into a pair of rivulets. (e)* $2.7\,s$ *after release, the rivulets continue to extend until they drop from the underside of the cylinder. (f)* $30\,s$ *after release, the points of detachment of fluid have extended along the underside of the cylinder. The experimental parameters are: cross-sectional area of fluid* $A = 5.2\,\mathrm{cm}^2$*; kinematic viscosity* $\nu = 5.1\,\mathrm{cm}^2/\mathrm{s}$*; surface tension* $\gamma = 64\,\mathrm{mN/m}$*; and radius of the cylinder* $R = 15\,\mathrm{cm}$*.*

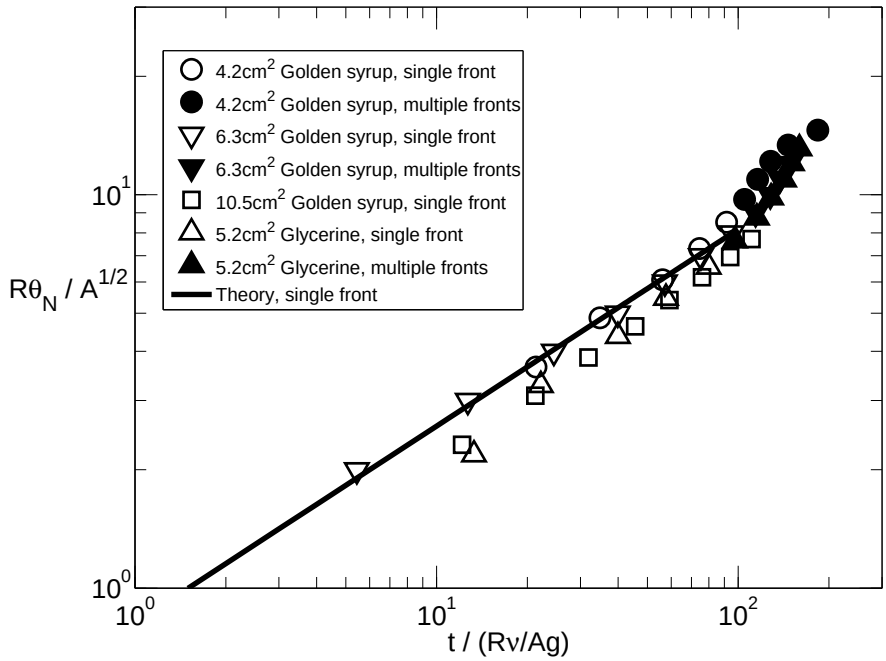

Figure 5.4: *Plot of non-dimensional flow extents on a cylinder against non-dimensional time using logarithmic axes. Different symbols correspond to different experiments. The symbols are either open or closed, with the latter indicating that rivulets have developed at the front of the flow. The black line is the theoretical relationship given by (5.15).*

the front developed a fingering instability, the subsequent leading fronts extended further along the cylinder than predicted by (5.15).

5.5.2 Flow on a vinyl beach ball

Experiments were conducted to investigate viscous flow on a sphere. A vinyl beach ball of radius 23.5 ± 0.5 cm was secured at its base. The surface of the beach ball was reasonably spherical and rigid. A cylindrical lock was positioned carefully at the top of the beach ball using a spirit level such that its axis pointed vertically. A constant volume of golden syrup was poured inside the lock, which could be swiftly raised by guiding it along a vertical rail to release the syrup. The radius of the gate was either 2 cm or 5 cm and made little difference to the resultant flow.

The near-instantaneous release of golden syrup resulted initially in an axisymmetric current from the top of the sphere as shown in figure 5.5(b). The structure of the flow extended with a circular plan form and then slowly started to deform in shape (figure 5.5(c)). Modulations then developed at the leading edge of the flow, as shown in figure 5.5(d). Soon after, a series of rivulets developed at the front (figure 5.5(e)). The rivulets are similar to those produced at the front of an initially axisymmetric spreading on a rotating plane (Melo *et al.*, 1989; Fraysse & Homsy, 1994). The rivulets continued to flow down the sphere until they reached some extent on its underside, where they detached and dropped in the form of threads.

The flow lengths along six representative directions were recorded at different intervals. Figure 5.6 shows that the mean flow lengths agree well with the theoretical curve before the leading edge of the flow developed a fingering instability. We now discuss scaling laws of the flow at the onset of the instability.

5.6 Discussion

It is widely accepted that a capillary ridge near the flow front plays an important role at the onset of the instability. Numerous other possible factors are believed to play a minor role. For example, the viscosity of fluid appears only to set the time scale and not the length scale of the flow resulting from the release of a constant volume of fluid (Huppert, 1982b). Experiments suggest that effects due to the contact angle at the flow front do not influence the onset of the instability either (Silvi & Dussan, 1985). Conjecturing that the onset of the instability is determined by the length scale l of the small capillary region near the flow front, we develop dimensional arguments to suggest scalings of the flow at

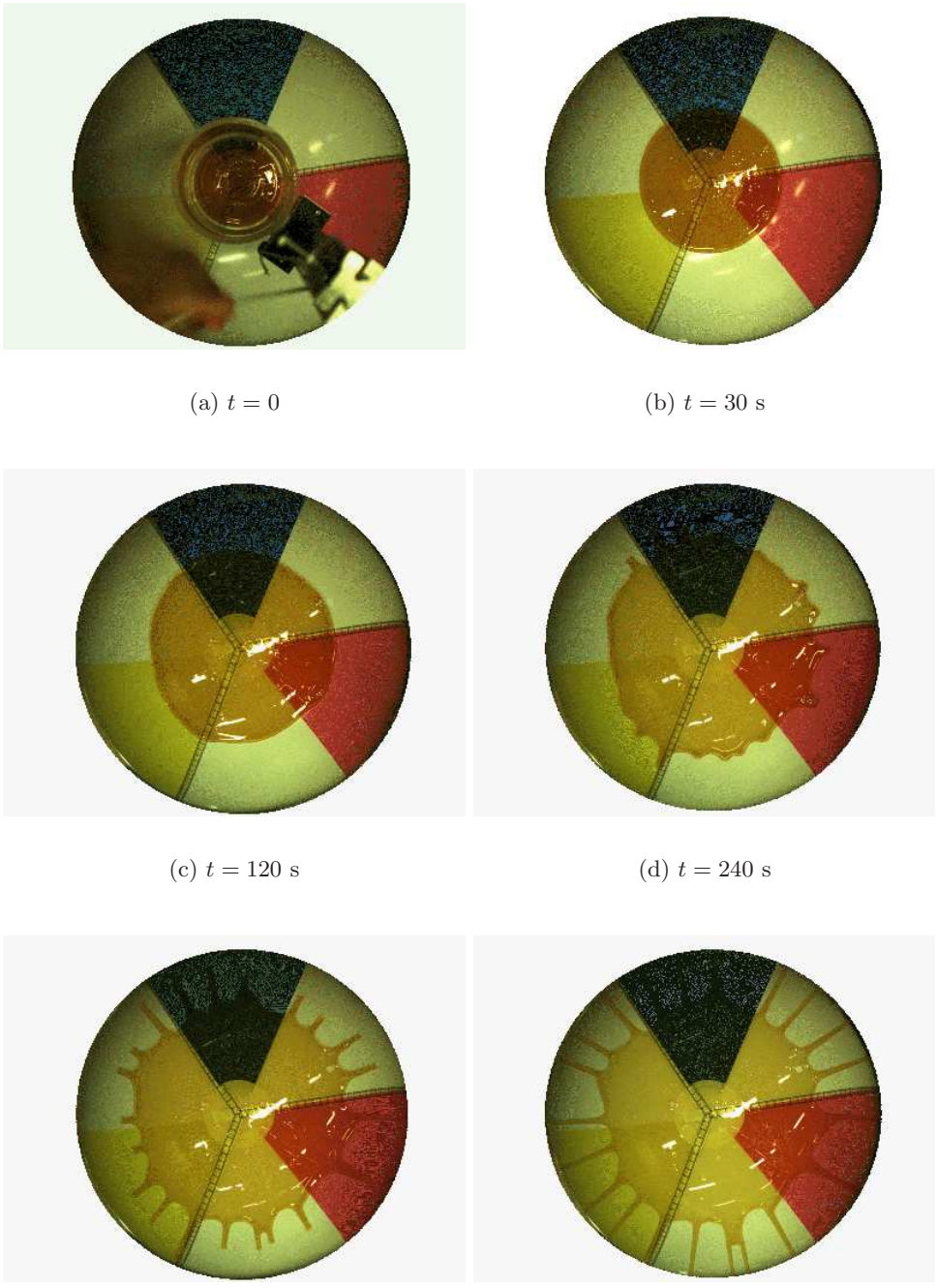

(a) $t = 0$ (b) $t = 30$ s

(c) $t = 120$ s (d) $t = 240$ s

(e) $t = 360$ s (f) $t = 900$ s

Figure 5.5: *Sequence of snapshots taken from above a six-sector beach ball of radius* $R = 23\,\mathrm{cm}$*, on which* $123\,\mathrm{cm}^3$ *of golden syrup was released. (a) Golden syrup is released by rapidly lifting a cylindrical gate. (b)* $30\,s$ *later, the structure of the flow continues to take a circular plan form. (c)* $120\,s$ *after release, the flow remains approximately axisymmetric. (d)* $240\,s$ *after release, wave patterns begin to develop at the leading edge of the flow. (e)* $360\,s$ *after release, the amplitude of the instability at the flow front grows and develops a series of rivulets. (f)* $900\,s$ *after release, the rivulets continue to flow down the beach ball, eventually detaching from the underside (not shown). The experimental parameters are kinematic viscosity* $\nu = 4.5 \times 10^2\,\mathrm{cm}^2/\mathrm{s}$ *and surface tension* $\gamma = 78\,\mathrm{mN/m}$ *(Llewellin* et al.*, 2002).*

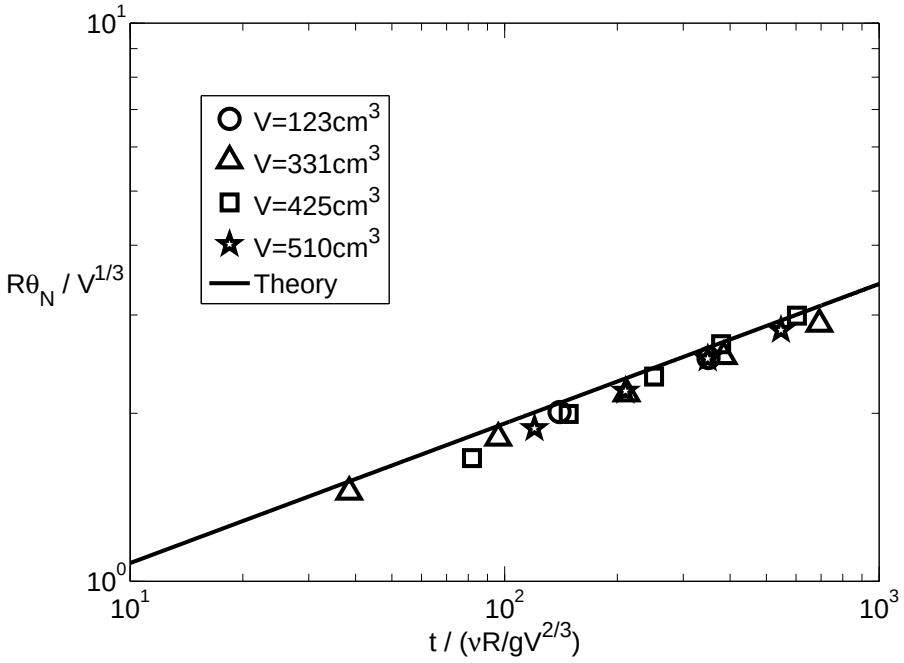

Figure 5.6: *Non-dimensionalised average flow lengths against non-dimensional time on the top of a sphere before rivulets developed. Different symbols correspond to experiments conducted by releasing different volumes of golden syrup. The black line is the theoretical relationship given by (5.29).*

the onset. The two important regimes of small and large Bond numbers will be treated separately, using ideas that have been developed in the well-studied context of flow down an inclined plane.

In the regime of small Bond numbers, surface tension initially plays a role not only at the tip of the current but also in the bulk region of the flow. It has been proposed that the bulk structure of the flow is stable until the flow extends a distance $x_c \sim l$ (Troian *et al.*, 1989). The current at the onset of the instability must extend sufficiently to develop a capillary ridge near the flow front ahead of a region where gravity dominates. Numerical simulations of a thin film flowing down an inclined plane (Schwartz, 1989) support the idea that gravity drives the fingering instability with a characteristic wavelength set by surface tension. The condition that gravity dominates in the bulk flow at the onset of the instability suggests that the critical distance x_c, scaled by the length scale of the bulk flow, increases in the limit of small Bond numbers.

In the regime of large Bond numbers, surface tension is initially negligible everywhere, including the region near the flow front. The flow front features a recirculating nose, which has been shown experimentally to extend initially without any development of a fingering instability (Ancey *et al.*, 2009). The apparent contact angle of the advancing

front is initially obtuse because gravity pushes the nose further than the contact line. It has been suggested that the fingering instability develops when the contact angle and the capillary number of the flow front have decreased sufficiently (Veretennikov *et al.*, 1998). Effects due to surface tension begin to play a role at the tip of the current when its thickness decreases and approaches the capillary length scale, l_c. We therefore conjecture that $h_N \sim l_c$ at the onset of the fingering instability of a current initially unaffected by surface tension everywhere. The condition that the length scale of the tip of the current must decrease to its capillary length scale before the front splits into rivulets suggests that the critical distance x_c, scaled by the length scale of the bulk flow, increases again in the limit of large Bond numbers.

The ideas developed above can be applied to the flow and instability of thin films on a cylinder and sphere. By balancing the magnitude of the bulk flow length in (5.15) with the capillary length scale of the front in (5.18) and coupling the result with (5.17), we obtain the length of the current on a cylinder for small Bond numbers at the onset of the instability,

$$x_c \sim A^{1/2} Bo^{-1/5}. \tag{5.34}$$

The critical length increases in the limit of small Bond numbers, as expected. By balancing the magnitude of the flow thickness in (5.17) with the capillary length scale of the front in (5.18), we obtain the length of the current on a cylinder for large Bond numbers at onset,

$$x_c \sim A^{1/2} Bo. \tag{5.35}$$

This indicates that the critical length increases in the limit of large Bond numbers. Note that x_c is a monotonically increasing function of A for all Bond numbers. Corresponding results are obtained for the length of the current at the onset of instability on a sphere,

$$x_c/V^{1/3} \sim \begin{cases} Bo_V^{-1/6} & \text{small } Bo_V \\ Bo_V^{1/3} & \text{large } Bo_V. \end{cases} \tag{5.36}$$

The critical length at the onset is a monotonically increasing function of the volume of fluid, V. For fixed V, the critical length increases both in the limits of small and large Bond numbers.

Given that the dimensionless length of the current at the onset of the instability increases both in the limits of small and large Bond numbers, there must be an intermediate range of Bond numbers where the dimensionless length is minimal. This is consistent with the dimensionless radius of a spinning drop at the onset of the fingering instability, which is minimal for Bond numbers $\rho\omega^2 V/\gamma \sim 50$ (Wang & Chou, 2001). Figure 5 in the paper

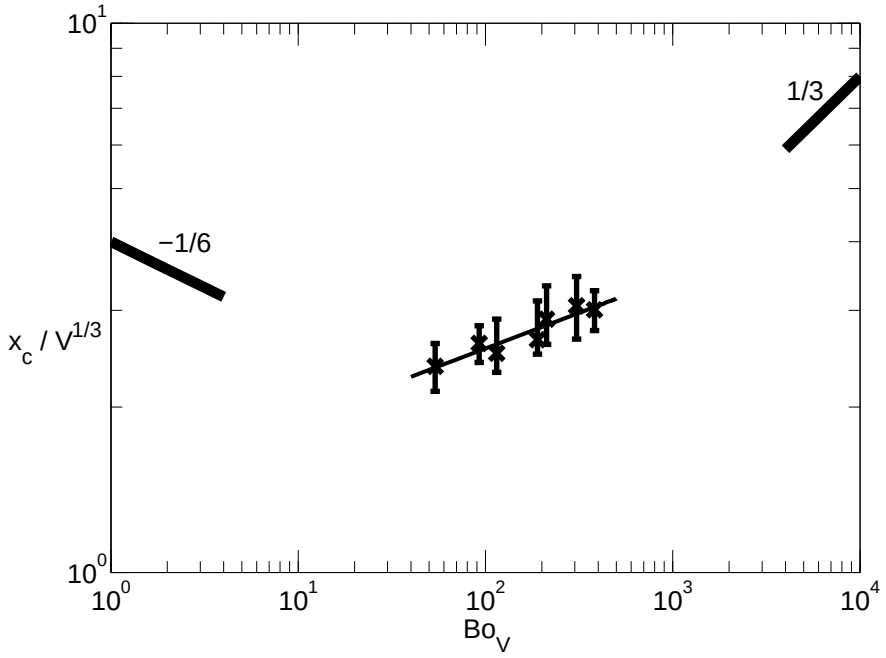

Figure 5.7: *Log-log plot of the lengths of golden syrup spreading on a sphere at the onset of the fingering instability against the Bond number given by (5.31), where representative values of* $\rho = 1.4\,\mathrm{kg/m^3}$, $g = 9.8\,\mathrm{m/s^2}$, $\gamma = 78\,\mathrm{mN/m}$ *and* $R = 0.24\,\mathrm{m}$ *were fixed. The Bond number was varied in different runs by releasing different volumes of fluid. The average flow lengths at the onset of instability are represented by crosses with associated error bars indicating the maximum and minimum flow lengths for each experiment. The line of best fit through the experimental data has a slope of* 0.13*, which lies between the two limits of* $-1/6$ *and* $1/3$ *as predicted by (5.36) for small and large Bond numbers.*

by Wang and Chou (2001) shows that the dimensionless radius of spinning drops at the onset depends weakly on the Bond number, when it is neither too small or large.

Our experiments on both the cylinder and the sphere were conducted over an intermediate range of Bond numbers. Consequently, the length of the current at the onset of the instability is expected to depend weakly on the Bond number. This is consistent with figure 5.4, which shows that rivulets on a cylinder developed when the flow front advanced $\simeq 8A^{1/2}$ in experiments, independent of the Bond number. Figure 5.7 plots the mean radius of flows spreading on a sphere at the onset of the fingering instability, as a function of the Bond number given by (5.31). The critical length of the flow increases slowly and depends weakly on the Bond number. A least-square fit to the data yields $x_c/V \simeq 1.4Bo_V^{0.13}$ within an intermediate range of Bond numbers, intermediate between scalings for small and large Bond numbers given in (5.36).

The wavelength of the fingering instability was estimated by dividing the circumference of the plan form at the onset of the instability by the number of rivulets observed sub-

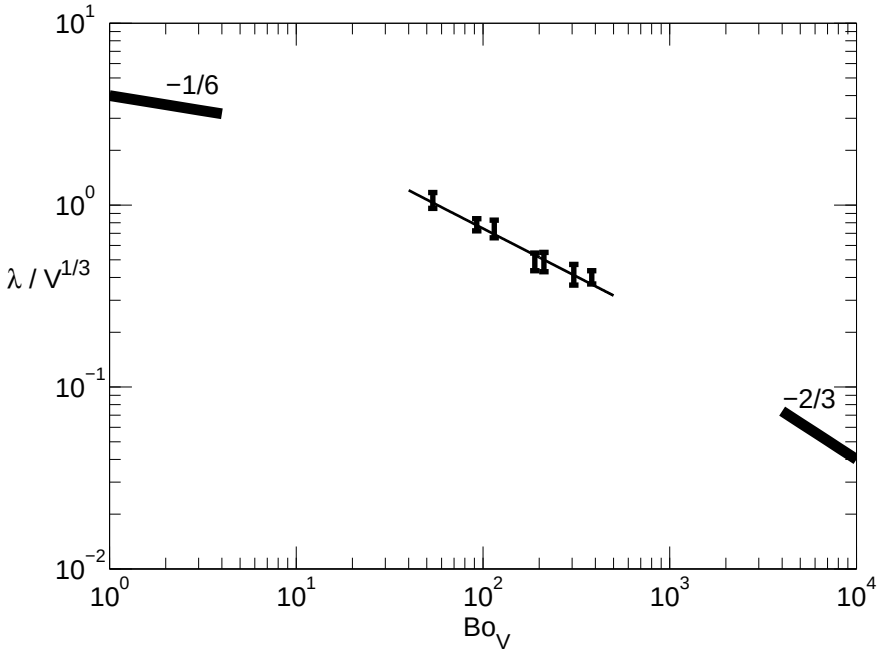

Figure 5.8: *Wavelengths of the fingering instability of golden syrup spreading on a sphere as a function of the Bond number given by (5.31), where* $\rho = 1.4\,\mathrm{kg/m^3}$, $g = 9.8\,\mathrm{m/s^2}$, $\gamma = 78\,\mathrm{mN/m}$ *and* $R = 0.24\,\mathrm{m}$. *Wavelengths were estimated by dividing the circumference of the leading edge of the flow at the onset of instability by the number of rivulets observed subsequently. Error bars are associated with the maximum and minimum flow lengths recorded at the onset of the instability for each experiment. The line fitting the average wavelengths has a gradient of* -0.52, *which lies between the two limits of* $-2/3$ *and* $-1/6$ *as predicted in (5.37) for large and small Bond numbers.*

sequently. The dimensionless wavelength is plotted against the Bond number Bo_V on logarithmic scales in figure 5.8. The line of best fit shown in figure 5.8 scales like $Bo_V^{-0.52}$ and indicates that the dimensionless wavelength decreases with Bond number. Conjecturing that the wavelength is set by the length scale of the tip of the current l in (5.18) (Huppert, 1982b), the wavelength scales like

$$\lambda/V^{1/3} \sim \begin{cases} Bo_V^{-1/6} & \text{small } Bo_V \\ Bo_V^{-2/3} & \text{large } Bo_V. \end{cases} \tag{5.37}$$

The exponent of -0.52 obtained from the experiments for an intermediate range of Bond numbers lies between the limiting exponents of $-1/6$ and $-2/3$ for small and large Bond numbers respectively.

The number of rivulets produced at the top of a sphere is given by

$$N = 2\pi x_c/\lambda, \tag{5.38}$$

when a sufficiently small volume of fluid is released such that $x_c \ll R$. By substituting (5.36) and (5.37) into (5.38), we estimate the number of rivulets to remain constant, or increase linearly with Bond number, in the limits of small and large Bond numbers respectively. This is consistent with the trend of the number of fingers produced on a rotating plane shown in Figure 12 of the paper by Wang and Chou (2001). Rivulets are not expected to develop on a cylinder or sphere when a sufficiently large volume of fluid is released.

5.7 Concluding remarks

We conclude that thin films spreading at the top of a cylinder and sphere result in a succession of events. Initially, both flows on the cylinder and sphere evolve with uniform thickness. The leading edge of the flows, after extending a critical distance, splits into a series of rivulets. The critical distance was shown experimentally to depend primarily on the volume of fluid released, for Bond numbers that are not too small or large. The relevant length scale is set by either the square root of the cross-sectional area of fluid or the cube root of the volume released for two-dimensional or axisymmetric spreading respectively. Experiments further showed that the rivulets extend along the cylinder and sphere until they eventually detach and develop pendent threads.

The detachment of fluid before it has reached the bottom of the cylinder or sphere gives rise to an interesting problem. Experiments reported in § 5.5 showed that releasing

a relatively small volume of fluid at the top of the cylinder and sphere does not result in complete coating of the cylinder or sphere. We conducted further experiments and observed that releasing a relatively large volume of fluid at the top of a cylinder does not result in complete coating either. Approximately $300\,\mathrm{cm}^3$ of golden syrup, poured from a beaker immediately above a cylindrical rod of steel of diameter 1.2 cm with its axis pointing horizontally, left a small uncoated region along the bottom of the rod. This qualitative observation indicates that it is difficult to completely coat the outer surface of a cylinder or sphere by releasing fluid from above.

A complete coating of the outer surfaces of a cylinder and sphere could be obtained instead by dipping them into and withdrawing from a bath of viscous fluid, a familiar method in coating industries. Thin films are expected to develop and drain as investigated here in § 5.3 and § 5.4 near the top of the cylinder and sphere. In contrast to a film of fluid draining from a vertical plate, which is always thicker towards the bottom of the plate (Jeffreys, 1930), the thickness of fluid draining from the top of the cylinder and sphere should remain uniform.

Chapter 6

Coating a sector of an inclined plane

6.1 Abstract

The flow of a Newtonian fluid down a rigid plane bounded by diverging walls is considered. The evolution at a low Reynolds number of a constant volume of fluid is determined using the free film lubrication theory and consists of up to three regimes. In the early-time regime, the fluid occupies the entire width of the prescribed bounds and spreads radially away from the source. In the intermediate regime, which exists on inclined planes bounded by gently diverging walls, the fluid continues to flow approximately radially down the slope. The front of the fluid appears to separate from the walls once it has extended a distance, which is estimated by scaling arguments and compared with experiments. In the late-time regime on an inclined plane, the front of the flow can become unstable and produce one or a series of extended regions.

6.2 Introduction

A thin layer of fluid flowing with a free surface above and a rigid surface underneath occurs naturally in a wide range of situations. These include the spreading of lava in geophysics,

the long-scale evolution of macroscopic thin films in biophysics and the manufacturing process of glass in industrial engineering. Some important flow features can be examined by considering a Newtonian fluid to be driven predominantly by effects due to gravity. The flow is consequently in the direction of any component of gravity and any gradient of the free surface. Effects due to inertia are small compared to viscous forces provided that the Reynolds number is small. Effects due to capillary action are neglected in the dynamical regime of interest, where the Bond number is large.

Previous studies indicate that the shape of the rigid surface plays an important role in influencing the evolution of the free surface. The thin film lubrication theory is used to describe the different flows that arise on an unconfined horizontal plane (Huppert 1982a), an unconfined inclined plane (Huppert 1982b, Lister 1992) and various different open channel systems (Takagi and Huppert 2007). The channels considered so far are limited to those with the condition that the characteristic length scale of the flow extent is much greater than the channel width. This allows any cross-stream flow to be neglected to leading oder and simplifies the governing equations considerably.

Here, the flow on a rigid surface confined by a pair of diverging walls is considered, where any cross-stream flow must be incorporated into the theory in general. Various different situations are considered with a particular emphasis on inclined flows, which are motivated by three separate ideas. Firstly, the flow front initially occupies the entire width of the bounds and eventually separates from the bounds. The transition from a laterally confined flow to an unconfined flow towards the front involves interesting dynamics near the bounds. This has never been investigated before as all previous studies assume the viscous flow on a rigid surface to be either confined or unconfined at all times. Secondly, the governing equations with additional terms introduced by any cross-stream flow provide a more general formulation of confined flows, where the channel width can be considered to vary arbitrarily. Thirdly, experiments conducted on an inclined rigid plane show that the front of the fluid becomes unstable when it is unconfined (Huppert 1982b) while its stability is not yet clear when it is confined with a sufficiently small channel width. Laboratory experiments on an inclined rigid plane with a pair of diverging walls are designed to investigate the influence of the lateral bounds on any development of instabilities at the front.

In the next section, a general theoretical formulation for the viscous flow on a sector-shaped plane is presented. Three dynamical phases generally exist and are identified as early-time, intermediate and late-time regimes in the subsequent subsections. In section 6.3, the separation of the fluid front from the lateral bounds is investigated with reference to laboratory experiments by considering the transition to the late-time regime. In section 6.4, the influence of the lateral bounds on the development of a fingering instability at the front is discussed.

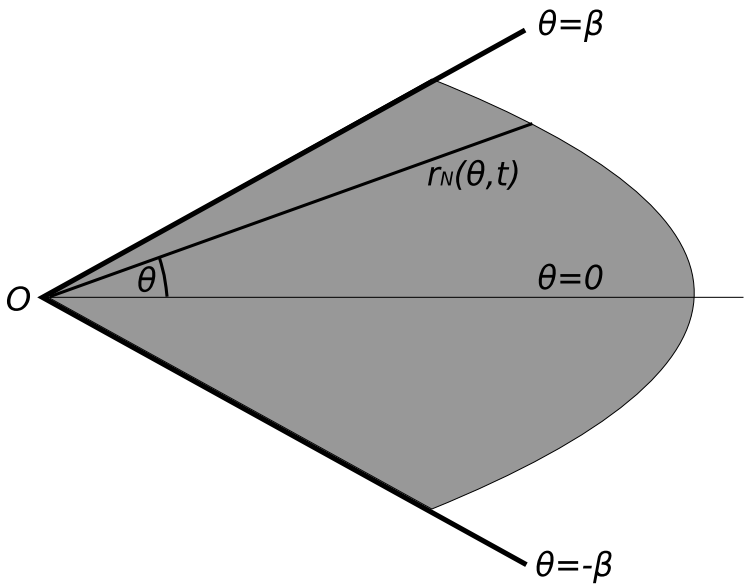

Figure 6.1: *A sketch in the (r,θ) plane of a constant volume of fluid, which flows away from the point source O and is marked by the shaded region of depth $h(r,\theta,t) > 0$ behind the front $r < r_N(\theta,t)$. The bounds are located at $\theta = \pm\beta$ and the fall line $\theta = 0$ makes an angle γ to the horizontal.*

6.2.1 Theory

Consider a flat channel with a linearly increasing width down a slope of angle γ to the horizontal. The side walls meet at angle 2β at the origin and the line of symmetry corresponds to the fall line. A cylindrical polar coordinate system is adopted so that the (r,θ) plane represents the bottom surface with the z axis pointing upwards normal to the plane. The fall line is represented by $\theta = 0$ and the pair of flat boundaries is represented by $\theta = \pm\beta$. A constant volume of viscous fluid is released instantaneously at the origin.

At any time $t > 0$, the fluid occupies a depth $h(r,\theta,t)$ and reaches an extent $r_N(\theta,t)$ down the inclined plane, as shown in figure 6.1. The length scale of the fluid depth is considered to be much smaller than its extent so that the lubrication approximation holds. The velocity vector $\mathbf{u}(r,\theta,z,t)$, satisfies the modified Stokes equation

$$\mu\frac{\partial^2}{\partial z^2}\mathbf{u} = \nabla p, \tag{6.1}$$

where $\nabla = \partial/\partial r + r^{-1}\partial/\partial\theta$ is the gradient operator in the (r,θ) plane and p is given by

$$p = \rho g[(h-z)\cos\gamma - r\cos\theta\sin\gamma]. \tag{6.2}$$

By imposing the no-slip boundary condition at the rigid boundary $z = 0$ and the no-stress condition at the free surface $z = h$, we determine the velocity profile to be parabolic and

is given by

$$\mathbf{u} = -\nabla p \frac{1}{2\mu} z(2h - z). \tag{6.3}$$

Note that the no-slip condition $\mathbf{u} = \mathbf{0}$ at the rigid bounds $\theta = \pm\beta$ is not satisfied by (6.3). The velocity profile inside a small inner region near the bounding walls $\theta = \pm\beta$ must have an explicit dependence on θ, which must be solved using the full Stokes equation rather than (6.1). However, the region must scale in width like the film thickness, which is assumed to be small compared to the channel width. The scaling follows from the isotropy of the biharmonic equation satisfied by the stream function of the two-dimensional Stokes flow. It is therefore adequate to consider the velocity profile to be given by (6.3) throughout the flow, to leading order.

The volumetric flux $\mathbf{Q}$ is defined as the depth-integrated velocity and is given by

$$\mathbf{Q} \equiv \int_0^h \mathbf{u}\, dz = -\frac{g}{3\nu} h^3 \nabla p. \tag{6.4}$$

By evaluating ∇p using (6.2) and substituting the expression into (6.4), the radial component of $\mathbf{Q}$ is given by

$$Q_r = \frac{g}{3\nu} h^3 [-\frac{\partial h}{\partial r} \cos\gamma + \cos\theta \sin\gamma] \tag{6.5}$$

and the azimuthal component by

$$Q_\theta = \frac{g}{3\nu} h^3 [-\frac{1}{r}\frac{\partial h}{\partial \theta} \cos\gamma - \sin\theta \sin\gamma]. \tag{6.6}$$

The depth averaged equation of mass conservation

$$\frac{\partial h}{\partial t} + \nabla \cdot \mathbf{Q} = 0, \tag{6.7}$$

where $\nabla \cdot \mathbf{Q}$ in cylindrical polar coordinates is

$$\nabla \cdot \mathbf{Q} = \frac{1}{r}\frac{\partial}{\partial r}(rQ_r) + \frac{1}{r}\frac{\partial}{\partial \theta}(Q_\theta), \tag{6.8}$$

becomes

$$\frac{\partial h}{\partial t} + \frac{g}{3\nu r}\Big[-\cos\gamma \frac{\partial}{\partial r}(rh^3\frac{\partial h}{\partial r}) + \cos\theta\sin\gamma \frac{\partial}{\partial r}(rh^3) - \frac{\cos\gamma}{r}\frac{\partial}{\partial\theta}(h^3\frac{\partial h}{\partial\theta}) - 3h^2\sin\gamma\sin\theta\frac{\partial h}{\partial\theta}\Big] = 0. \tag{6.9}$$

The depth at any point evolves in time according to (6.9) due to four different factors. The second term of (6.9) corresponds to the radial gradient of the free surface, the third term the component of gravity in the radial direction, the fourth term the azimuthal gradient of the free surface and the fifth term the component of gravity in the azimuthal direction.

Finally, the global conservation of mass is given by

$$\int_{-\beta}^{\beta}\int_{0}^{r_N(\theta,t)} rh(r,\theta,t)\,dr d\theta = V \tag{6.10}$$

and completes the mathematical formulation of the problem. By considering the asymptotic balances of (6.9), there exist up to three regimes, which are studied separately in the following subsections.

6.2.2 Early-time regime

Initially, the depth profile is independent of θ so that $h = h(r,t)$. Any gradient in the free surface along the azimuthal direction will induce a flow to quickly diminish it. The fourth and fifth terms of (6.9) are therefore negligible to leading order. In addition, the spatial gradient of the thickness of the current is initially greater than the slope of the rigid plane. This means that only the first and second terms of (6.9) balance to give the approximate evolution equation

$$\frac{\partial h}{\partial t} - \frac{g\cos\gamma}{3\nu r}\frac{\partial}{\partial r}(rh^3\frac{\partial h}{\partial r}) = 0. \tag{6.11}$$

The self-similar solution satisfying (6.10) and (6.11) is given by

$$h(r,t) = (\frac{3}{4})^{1/4}\Big(\frac{V\nu}{\beta g t\cos\gamma}\Big)^{1/4}(1-r^2/r_N^2)^{1/3}, \tag{6.12}$$

where r_N is independent of θ and is given by

$$r_N(t) = (\frac{4}{3})^{5/8}\Big(\frac{V^3 g\cos\gamma}{\beta^3\nu}\Big)^{1/8}t^{1/8}. \tag{6.13}$$

It is worth noting that this solution tends to the solution of an axisymmetric spreading on a horizontal plane (Huppert, 1982a) in the limit as $\beta \to \pi$ and $\gamma \to 0$. The solution holds in the early-time regime, $t \ll T^*$, for some T^*. The time scale T^* corresponds to the time when flow induced by the gradient of the free surface and the component of gravity in the radial direction become comparable. This is given by

$$T^* = \frac{\nu}{gV^{1/3}}\Big(\frac{\beta\cos^5\gamma}{\sin^8\gamma}\Big)^{1/3}, \tag{6.14}$$

which is obtained by considering the scaling factors in (6.10) and balancing the second and third terms of (6.9). In the limit as $\gamma \to 0$, $T^* \to \infty$ by (6.14) so only the early-time regime is encountered in the limit as the rigid plane approaches the horizontal.

6.2.3 Intermediate regime

If the rigid plane is inclined, $\gamma > 0$, then the radial gradient of the free surface becomes less important for all $t \gg T^*$. In addition, if β is sufficiently small with $\tan\beta \ll 1$ so that the channel widens slowly down the plane, then $\cos\theta\partial h/\partial r \gg r^{-1}\sin\theta\partial h/\partial\theta$ so the component of gravity is approximately in the radial direction everywhere. Any significant azimuthal gradient of the free surface is considered to be diminished at a very short time scale by the resultant flow and the presence of the lateral bounds. This leaves only the first and third terms of (6.9) to balance to give

$$\frac{\partial h}{\partial t} + \frac{g\sin\gamma\cos\theta}{3\nu r}\frac{\partial}{\partial r}(rh^3) = 0. \tag{6.15}$$

Note that the depth h depends implicitly on θ through the multiplicative factor of the second term in (6.15). This dependence is weak, which means that the fluid must continue to flow in the radial direction to leading order. Furthermore, the depth h must vanish at O because the flux vector $\mathbf{Q}$ and hence Q_r in (6.5) must vanish at the source. The self-similar solution satisfying (6.10) and (6.15) with the condition that the depth h vanishes at O is given by

$$h(r,\theta,t) = (\frac{9}{20})^{1/5}\Big(\frac{V\nu^2}{\beta g^2 t^2\sin^2\gamma\cos^2\theta}\Big)^{1/5}(r/r_N)^{1/2}, \tag{6.16}$$

where r_N is given by

$$r_N(\theta,t) = (\frac{125}{48})^{1/5}\Big(\frac{V^2 g\sin\gamma\cos\theta}{\beta^2\nu}\Big)^{1/5}t^{1/5}. \tag{6.17}$$

The agreement between theory and experimental data in figure 6.2 shows that the overall structure of the flow is given by (6.16) and (6.17), suggesting that the neglected details at the front or near the walls do not play an important role. The solution (6.16) can be substituted into (6.9) to justify the earlier assumptions that the second, fourth and fifth terms of (6.9) are relatively small in the intermediate region $T^* \ll t \ll T^{**}$. The time scale T^{**} is that at which the third and fourth terms of (6.9) become comparable and is given by

$$T^{**} = \frac{\nu}{gV^{1/3}\beta^3}\Big(\frac{\cos^5\gamma}{\sin^8\gamma}\Big)^{1/3}. \tag{6.18}$$

It can be verified using the forms of the two time scales in (6.14) and (6.18) that the intermediate regime exists when $\tan\beta \ll 1$.

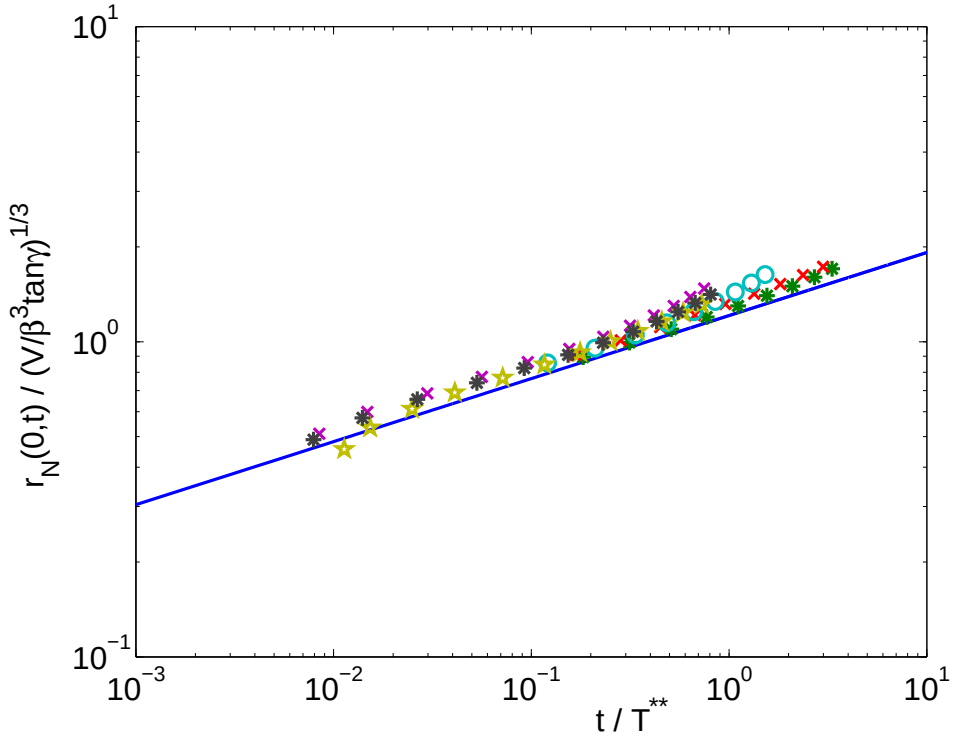

Figure 6.2: *A plot of the non-dimensional flow extent $r_N(0,t)/L$ against non-dimensional time t/T^{**}, where $L = (V/\tan\gamma)^{1/3}\beta^{-1}$ and T^{**} is given by (6.18). Experimental data for each run using a different set of V, γ and ν are marked in different symbols and appear to collapse together on the theoretical line given by (6.17) for $t < T^{**}$ as expected. Polygonal symbols correspond to experiments on a gentle slope $\tan\gamma = 0.069$ while dots and crosses correspond to experiments on a steep slope $\tan\gamma = 0.64$. The early time regime $t < T^*$ is too short to appear in the figure. The late time regime in which (6.17) no longer holds is shown by the experimental data points that slowly divert away from the solid line after $t > T^{**}$ in the figure.*

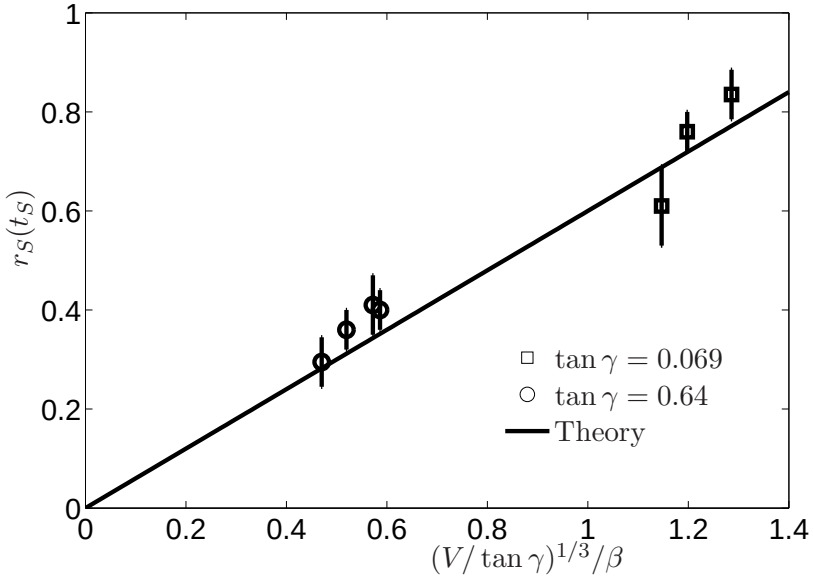

Figure 6.3: *Extent of the flow along the confining walls where the fluid appears to separate from the walls, plotted against the right hand side of (6.21). All units are in metres. Data of experiments conducted on gentle ($\tan\gamma = 0.069$) and steep ($\tan\gamma = 0.64$) inclines are shown to fit reasonably well with the theoretical line of slope 0.6. V varied from 350 to 770 cm^3 and $\beta = \pi/18$ was fixed. The error bars represent typical variations in the flow extent along the walls.*

6.2.4 Late-time regime

Effects due to the component of gravity down the slope and the lateral gradient of the free surface become comparable in the late-time regime $t \gg T^{**}$. The fluid has spread sufficiently far away from the source that only a small region near the source is in contact with the walls. The small influence of the lateral bounds can be neglected. As $t \to \infty$, the limiting form of (6.9) is identical to the late-time behaviour of viscous spreading down an unconfined slope from a point source (Lister 1992). The results are that

$$r_N(\theta = 0, t) \sim \left(\frac{V^4 g^3 \sin^8\gamma}{\nu^3 \cos^3\gamma}\right)^{1/9} t^{1/3} \tag{6.19}$$

and the maximal extent of the fluid away from the fall line $\theta = 0$ scales like $(V/\tan\gamma)^{1/3}$ (Lister 1992). The dependence on β and the confinement near the source is lost as the majority of the flow becomes unconfined. These results hold in the late-time regime up until a fingering instability develops at the leading front of the flow.

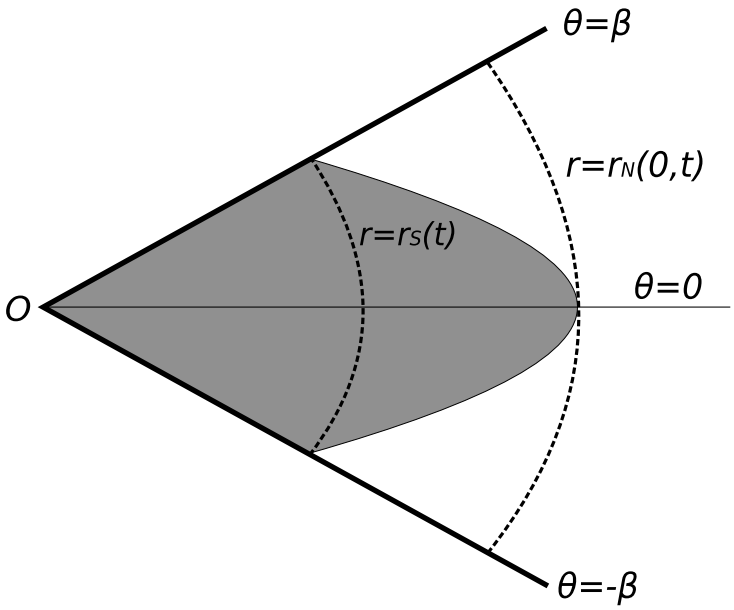

Figure 6.4: *A sketch in the (r, θ) plane of the region whose width of the bounds is fully occupied $(r < r_S(t))$ and partially occupied $(r_S(t) < r < r_N(0,t))$.*

6.3 Transition from confined to unconfined flow

Laboratory experiments were conducted to investigate the transition from confined to unconfined flow. A constant volume of glycerine was released rapidly down a 2 m channel of slowly increasing width, where $\beta = \pi/18$. The volume of the fluid and the angle of inclination of the channel were varied systematically. The leading edge of the bulk structure flowing down the centreline of the channel and along the confining walls was measured at different times.

The experiments show that the front of the fluid eventually separates from the bounds. This means that the flow front $r_N(\theta, t)$, whose extent does not depend on θ initially, deforms such that $r_N(\beta, t) < r_N(0, t)$ as shown in figure 6.4. The flow extent along the sides, denoted by $r_S(t) \equiv r_N(\beta, t)$, continues to grow with time but much more slowly than $r_N(0, t)$, the flow extent along the fall line.

A scaling analysis indicates that the flow front begins to deform significantly during the transition from the intermediate to the late-time regime. The difference between $r_N(0, t)$ and $r_N(\beta, t)$ is identically 0 during the early-time regime and is of order β^2 by (6.17) and hence negligible during the intermediate regime. At some time $t_S \sim T^{**}$, however, the azimuthal flow can no longer be neglected. This is when the spreading due to the component of gravity down the slope and the cross-slope gradient of the free surface

become comparable. The depth evolves according to

$$\frac{\partial h}{\partial t} + \frac{g}{3\nu r}\left[\cos\theta \sin\gamma \frac{\partial}{\partial r}(rh^3) - \frac{\cos\gamma}{r}\frac{\partial}{\partial\theta}\left(h^3\frac{\partial h}{\partial\theta}\right)\right] = 0, \tag{6.20}$$

which is obtained by keeping the first, third and fourth terms of (6.9). There is now an explicit dependence of the depth profile h and the frontal extent r_N on θ. As a result, a significant qualitative change in the shape of the fluid-air interface at the front is encountered for the first time. This naturally gives rise to a separation point whose radial extent $r = r_S(t)$ is well behind the flow extent $r_N(0,t)$ along $\theta = 0$. By considering the scaling factors of (6.10) and (6.20), we determine the radial extent at which the transition to the late-time regime occurs to scale like

$$r_S(t_S) \sim (V/\tan\gamma)^{1/3}/\beta. \tag{6.21}$$

The constant of proportionality is estimated to be approximately 0.6 using sets of experimental data, which are plotted in figure 6.3. The linear relationship between $r_S(t_S)$ and $(V/\tan\gamma)^{1/3}/\beta$ is consistent with the scaling relationship (6.21). The exact evolution of r_S, which extends much more slowly than the extent of the flow down the centreline of the inclined plane, is not pursued any further here.

6.4 Fingering instability at the front

Laboratory experiments show that for a fixed volume of fluid, the front of the current ultimately develops a fingering instability and forms one or a series of rivulets extending down the slope. The fingering instability in all experiments occurred at time $t > T^{**}$, after the front had separated from the walls. The characteristic wavelength of the instability is discussed below.

The extent $r = r_I$ at which the front first develops an instability might possibly depend on one or a combination of V, g/ν, β and $\tan\gamma$, the only parameters appearing in the formulation of the problem. By dimensional analysis, r_I must be proportional to $V^{1/3}$ as it is the only way of constructing a length scale that does not depend on time. In addition, the wavelength of the instability at the front must have a characteristic length scale λ that may depend on the surface tension T but is independent of ν (Huppert 1982b). A scaling analysis of (6.9), incorporating effects due to surface tension, offers an order-of-magnitude estimate of λ. The analysis is similar to that performed for the fingering instability of thin films on a cylinder and sphere (Takagi & Huppert, 2010). Further work is required to investigate effects on the fingering instability due to the curved front of the bulk flow. Unlike the spreading on a cylinder or sphere, where the fluid is initially uniform across the

flow, the curved front of the current down a sector-shaped plane may influence the onset and the wavelength of the instability.

6.5 Conclusion

A constant volume of fluid, released on a sector-shaped plane, evolves in three different regimes. In the early-time regime $t \ll T^*$, the front spreads away from the source and the flow extent scales with time like $t^{1/8}$. In the intermediate regime $T^* \ll t \ll T^{**}$, the current continues to spread predominantly radially and the flow extent scales like $t^{1/5}$. In the late-time regime $t \gg T^{**}$, the leading edge of the fluid has separated from the walls and its extent scales like $t^{1/3}$ down the slope. The separation occurs when the flow extends a distance, which is proportional to $V^{1/3}$ and independent of ν.

Chapter 7

Steady granular flow confined by levees down a rough inclined plane

7.1 Abstract

Laboratory experiments of sand flowing steadily on a rough inclined plane are reported and discussed. A dense granular flow between static levees develops down the plane and reaches a steady state, which is attained more rapidly if the plane is initially covered in sand to a thickness h_{stop}. The characteristic width of the bulk flow increases linearly with the mass flow rate, which does not appreciably affect the maximal thickness or surface velocity at large times. We propose a simple model which is consistent with our observations. The decrease in thickness toward the margins of the flow and the existence of a minimum flow rate of steady flow are discussed. The flow features of sand are different from those of spherical beads which ultimately become unstable, indicating that the shape of grains plays an important role in shallow granular flows.

7.2 Introduction

Granular materials can flow in a wide range of geophysical situations, on the Earth and on Mars, and in industrial settings. Examples include landslides, ice streams, pyroclastic flows and pill dispensers. To gain a better understanding of these forms of motion, dense granular flows have been studied extensively in recent years (GDRMiDi, 2004; Forterre & Pouliquen, 2008). Many experiments have contributed to the development of a continuum theory of granular dynamics (Jop *et al.*, 2006), but this is not anywhere near complete.

For steady flow down a rough plane inclined at a range of intermediate angles (Azanza *et al.*, 1999; Forterre & Pouliquen, 2003; Pouliquen, 1999; Silbert *et al.*, 2001; Börzsönyi & Ecke, 2007), the theory predicts

$$\frac{U}{\sqrt{gh}} = \alpha + \beta \frac{h}{h_{\mathrm{stop}}}, \tag{7.1}$$

where U is the depth-averaged velocity, h is the flow depth, h_{stop} is the thickness of the layer that naturally deposits on the incline when the flow stops, g is gravitational acceleration and α and β are dimensionless parameters. However, this theory and most others (Goldhirsch, 2003; Jenkins, 2006) do not accurately describe how shallow layers with thickness close to h_{stop} can be either static or flowing. Open problems remain in addressing nonlocal effects which play a role in shallow layers close to jamming (Rajchenbach, 2003; Aranson *et al.*, 2008; Pouliquen & Forterre, 2009), a phenomenon exhibited similarly by yield stress fluids (Coussot *et al.*, 1996; Balmforth *et al.*, 2002). Shallow granular flows must be better understood in order to conduct hazard analysis by predicting paths of natural flows, which are often close in thickness to h_{stop} as they spread out over an open slope (McDonald & Anderson, 1996; Félix & Thomas, 2004; Deboeuf *et al.*, 2006; Mangeney *et al.*, 2007*a*).

Previous experiments showed that spherical beads released steadily on a rough incline develop a thin flowing layer with nearly static margins (Félix & Thomas, 2004). Further experiments showed that the flow gradually becomes thinner and wider in time (Deboeuf *et al.*, 2006). The authors of this paper claimed that the structure of the flow approaches a steady state. However, we conducted similar experiments, but for longer periods, by releasing spherical beads of diameter 0.35 ± 0.05 mm at a rate of 4.6–21.0 g/s on rough slopes of 24–26 degrees, and discovered that the margins of the flow eventually become unstable, leading to considerable spatiotemporal variations in the flowing structure after a typical time of 70–90 minutes. The instability is not observed when the beads are replaced with the more generic material of non-spherical grains of sand, as reported here, indicating that the shape of grains plays an important role in shallow granular flows.

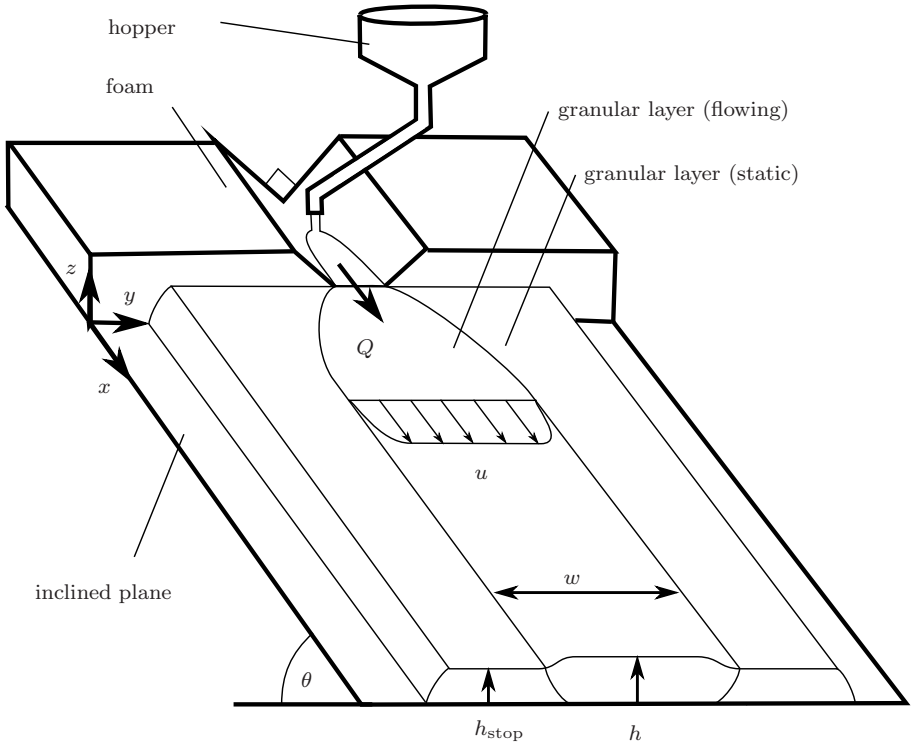

Figure 7.1: *Schematic of the experiment. Sand in the hopper is released onto the V-shaped foam and flows down the rough inclined plane. The bulk layer of the resultant flow has thickness h, width w, and surface velocity u, confined by static layers of sand of thickness h_{stop}. The angle of inclination of the plane $\theta = 32^o$ is fixed and the steady mass flow rate Q is chosen within a wide range.*

7.3 Method

We have carried out laboratory experiments to investigate sand flowing down an open and rough incline (figure 7.1). The sand consisted of non-spherical grains of mean diameter $0.45 \pm 0.15\,\mathrm{mm}$ and was glued on the incline to form a rough surface. The incline was 3 m long and 1 m wide, which was wider than any of the flows in our experiments. The incline was fixed at an angle of 32° to the horizontal because this produces steady flows confined by levees over approximately the widest range of flow rates. Our preliminary study of steady flows provides a foundation for future studies of intermittent avalanches (Börzsönyi *et al.*, 2008) and roll waves (Forterre & Pouliquen, 2003), which develop on gentler and steeper slopes respectively. The experiments were initiated in two different ways. In one set of experiments the incline was initially free of sand. In another set of experiments the incline was covered in an erodible layer of uniform thickness $h_{\mathrm{stop}} \approx 4.5\,\mathrm{mm}$. The static layer was set up before each run by releasing sand steadily onto the incline until the flow was uniform and then abruptly stopping the flow, a technique adopted previously (Pouliquen, 1999).

A perspex cylindrical hopper of diameter 250 mm and height 700 mm was used to supply the sand. The bottom of the hopper was connected to a cone which fed the sand into a smooth pipe of diameter 30 mm. A control valve could be screwed across the pipe to control the mass flow rate Q to lie between 5 and $218\,\mathrm{g\,s^{-1}}$, with a repeatability better than $\pm 2\,\mathrm{g\,s^{-1}}$. Steady flows could be maintained indefinitely by transferring the sand that flowed off the inclined plane back into the hopper. Below the control valve the sand fell freely down a tube onto a block of foam on the inclined surface. There was a 'V'-shaped groove cut into the middle of the foam to produce a point-like source of grains so that the only length scale was set by the flow rate. The foam was highly inelastic and absorbed the energy of the impacting grains so as to produce a dense flow from the source.

All measurements of the flow were taken approximately 2 m down the incline, where the flow was fully developed. This was verified by mounting instruments on a traverse and checking that measurements at other positions did not vary. The flow thickness was measured to an accuracy of ± 0.1 mm at 1 000 Hz using a laser triangulator (Micro-Epsilon LLT2800–100 2D Laser displacement measuring system). This could only measure the thickness over ≈ 130 mm of the flow so for wider flows it was positioned to observe one edge rather than the whole flow. Surface velocities were measured to an accuracy of $\pm 0.3\,\mathrm{mm\,s^{-1}}$ with a high-speed camera (Photron SA1 5 400 fps, 1024×1024 pixels, 12 bit ADC) using PIV (Dalziel, 2003). The cross-slope thickness and velocity profiles were averaged over 30 seconds to reduce statistical fluctuations.

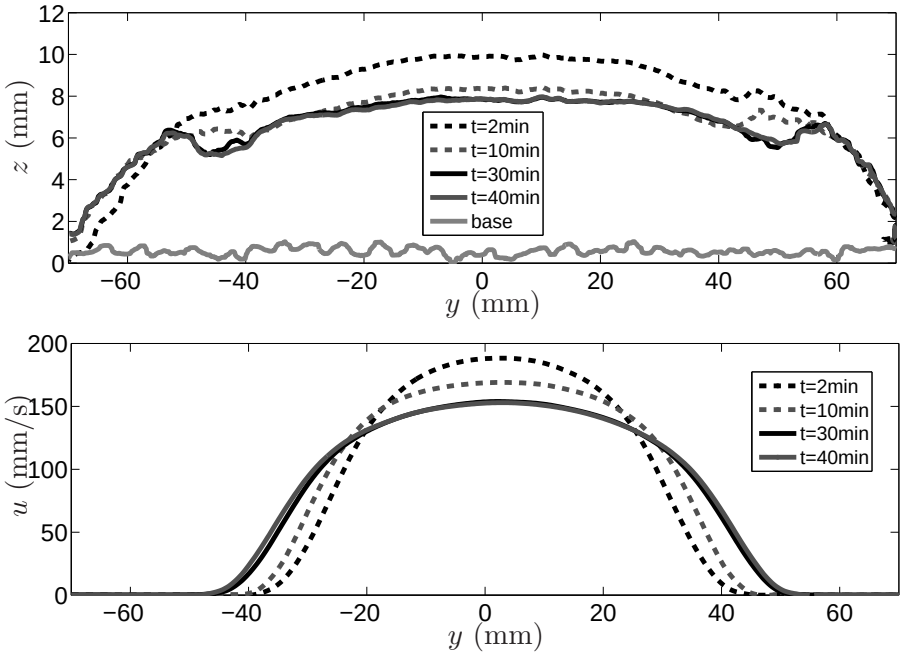

Figure 7.2: *Thickness and surface velocity of sand* 2 m *down a rough incline, which is initially free of sand. Both the characteristic thickness and surface velocity decrease slowly with time until a steady state is reached.*

7.4 Results

Our results show that steady flows develop for mass flow rates ranging between 31 and $218\,\mathrm{g\,s^{-1}}$. For flow rates below $Q_c = 20 \pm 10\,\mathrm{g\,s^{-1}}$ steady flows are not obtained; instead, avalanches are triggered nearly periodically. Here we examine steady flows, though we discuss the implications of the unsteady system at small flow rates in the conclusion. Temporal evolutions of the thickness and the surface velocity across the flow with $Q = 50\,\mathrm{g\,s^{-1}}$ for an experiment initiated without erodible grains on the incline are shown in figure 7.2. There is a gradual decrease in height and velocity once the initial flow front has passed the measurement point. Note that the curves at 30 and 40 minutes in figure 7.2 overlay each other, indicating that the system has reached an approximately steady state. We verified by conducting experiments for over two hours that both the thickness and width of the flow tend to constant values with time.

Figure 7.3 shows the corresponding results of another run initiated differently by covering the incline to a thickness h_{stop} and maintaining the same flow rate as before. The flow attains a steady state more quickly, as indicated by the coinciding curves at 12 and 20 minutes. Figure 7.4 shows that the steady velocity profiles coincide with the previous case, indicating that the long-time steady state is independent of the initial conditions on the incline. The remaining discussion is based on measurements of steady flow, obtained more quickly by initially covering the incline with sand of thickness h_{stop}.

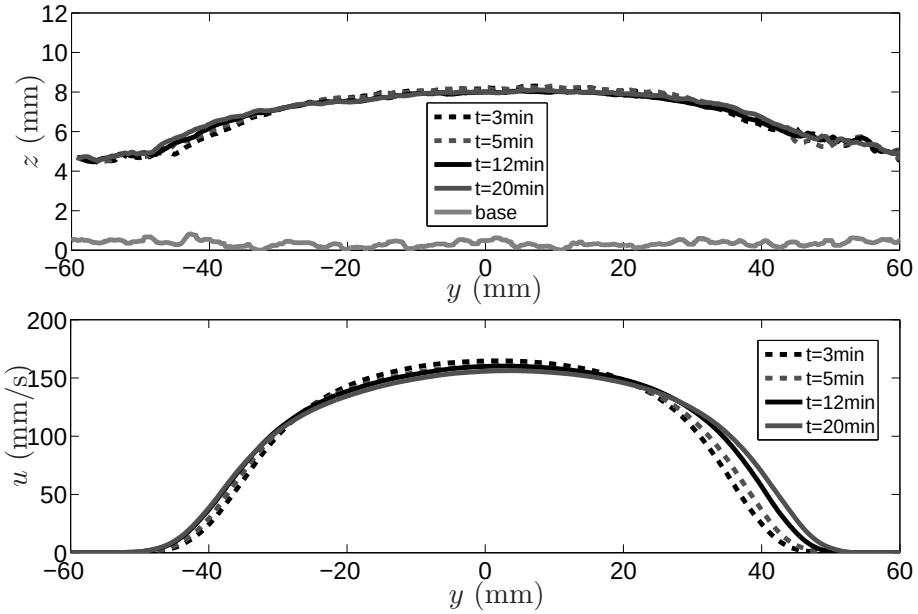

Figure 7.3: *Thickness and surface velocity of sand* 2 m *down a rough incline initially covered with a static, erodible layer of thickness* h_{stop}*. Minimal variations with time indicate that the flow quickly reaches a steady state.*

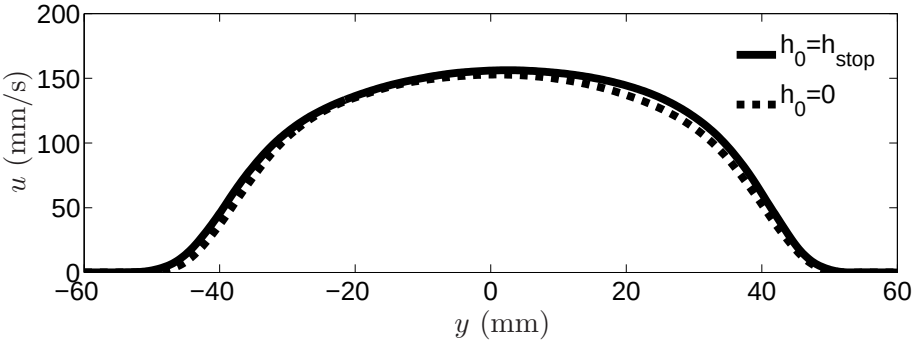

Figure 7.4: *Steady surface velocity profiles in the long-time limit on a rough incline, covered initially with no sand* ($h_0 = 0$) *and with an erodible layer of sand* ($h_0 = h_{\mathrm{stop}}$)*. The mass flow rate is* $Q = 50\,\mathrm{g/s}$ *in both experiments.*

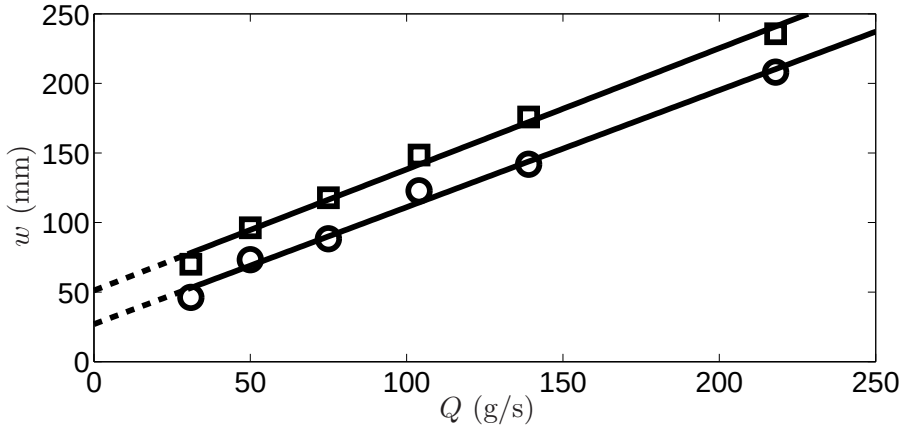

Figure 7.5: *Characteristic width of the flowing region with non-zero velocity (squares) and surface velocity greater than half the maximal velocity attained at the center of the flow (circles), plotted against the mass flow rate. Each line of best fit is extrapolated to* $Q = 0$.

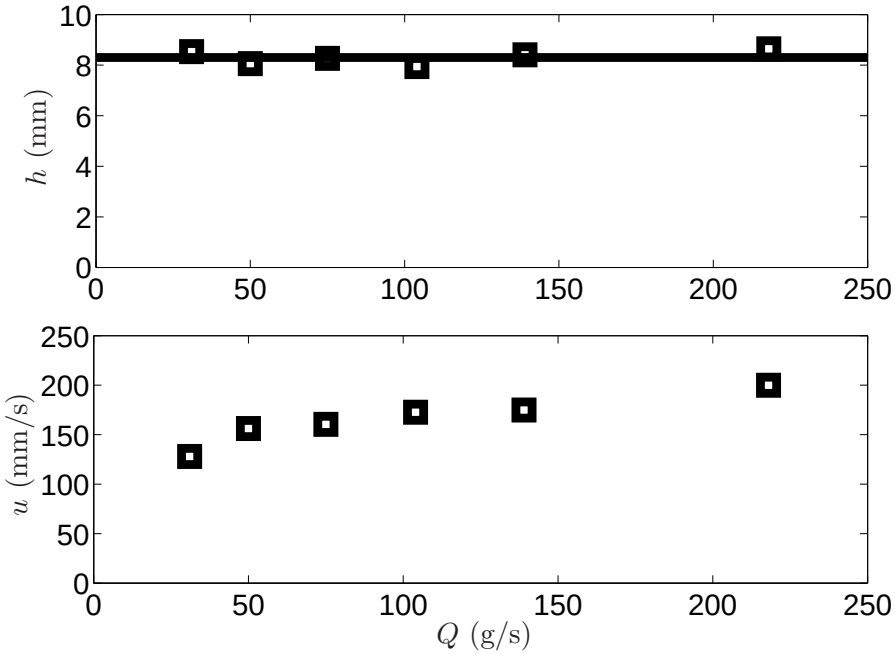

Figure 7.6: *Maximal thickness and surface velocity of steadily flowing sand as functions of the mass flow rate,* Q.

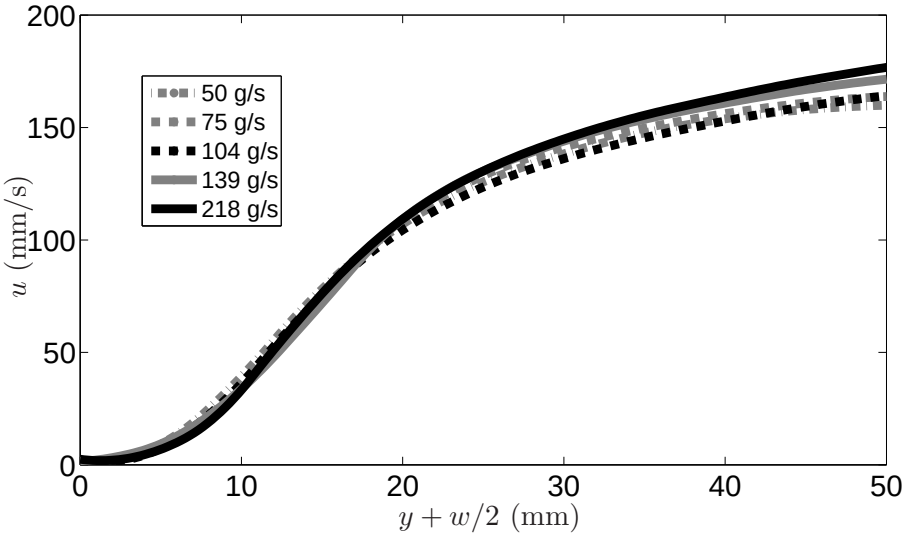

Figure 7.7: *Surface velocity profiles across the slope near one margin of the flowing layer for different mass flow rates.*

Steady flows obtained at different flow rates all feature a central region of approximately constant thickness and a pair of margins where the thickness decreases to h_{stop}. The central region is characterized by its width w, maximal thickness h and surface velocity attained at the center of the flow u. The width of the flow increases linearly with the mass flow rate as shown in figure 7.5, where w is defined as the width of the region with surface velocity greater than one half of its maximum attained at the center. We have considered other definitions of the width, including the width of the region of non-zero velocity (Deboeuf *et al.*, 2006), which changes the intercept w_0 but gives the same slope as shown by the approximately parallel lines of best fit in figure 7.5. The error bars are comparable to both the size of the symbols and the linear norms of residuals of the two fitting lines, 12–13 mm. The thickness of the central flow is independent of the flow rate and shows no systematic deviation, as shown in figure 7.6. In contrast to the observations and theory of (Deboeuf *et al.*, 2006), the bulk region of the flowing layer in all our experiments is flat with a maximal thickness of 8.3 ± 0.4 mm, which is greater than, but the same order of magnitude as, $h_{\text{stop}} \approx 4.5$ mm. The surface velocity increases weakly with the flow rate and appears to approach a finite limit as $Q \to \infty$, as shown in figure 7.6. There is a relatively large change between $Q = 31$ and $Q = 50\,\text{g}\,\text{s}^{-1}$ but from here to $Q = 218\,\text{g}\,\text{s}^{-1}$, a 430% increase in mass flow rate, the velocity only increases from 158 to $200\,\text{mm}\,\text{s}^{-1}$, a 26% increase. The increase in velocity with increasing mass flow rate, without any change in the flow depth, is attributed to the reduced influence of lateral stresses as h/w decreases. The surface velocity varies strongly at the margins and weakly in the central region, suggesting that lateral stresses are most important at the margins, but also play

a role in the center of the flow even at a small aspect ratio of 1/20. Lateral variations in the surface velocity toward one margin of the flow for different flow rates are shown in figure 7.7. The approximate collapse of the velocity profiles suggests that the margins of the flowing layer are independent of the mass flow rate. Note that the length scale of the margins is comparable in order of magnitude to w_0.

7.5 Discussion

We propose a simple model that incorporates all our observations. In the central region of the bulk flow, any lateral variation in the layer thickness would be reduced by a cross-stream flow driven by an induced pressure gradient. Given that the long-time steady flow must be in lateral force balance, and that the central region is yielded and behaves like a fluid, the layer thickness becomes flat over time sufficiently far downstream, as shown for $|y| < 20\,\mathrm{mm}$ in figure 7.3. The layer thickness is governed by the details at the margins, which are independent of the flow width for sufficiently wide flows (figure 7.7). The central region of wide flows has the same constant height h, depth-averaged velocity U and density ρ, independent of the flow rate Q, in agreement with figure 7.6. An increase in the flow rate results predominantly in an increase in the flow width described by

$$Q = (w - w_0)q, \tag{7.2}$$

where $q = \rho h U$ is the mass flow rate per unit cross-stream width and w_0 can be interpreted as a correction in the flow width due to the margins. The flow width increases linearly with the mass flow rate Q because w_0 and q depend on the grain and incline properties but not on Q. The agreement of this model with our experiments is shown by the linear relationships in figure 7.5.

The model of Deboeuf *et al.* (2006) has a constant aspect ratio $\gamma = h/w$ independent of the mass flow rate, which does not agree with our experimental results. The assumption of a constant aspect ratio and a scaling analysis of the flow rule (7.1) imply that w scales like either $Q^{2/5}$ or $Q^{2/7}$ for small or large Q respectively. This is inconsistent with the linear relationship between w and Q (figure 7.5). In addition, the model of Deboeuf *et al.* (2006) predicts the flow thickness to increase arbitrarily as the flow rate is increased. This could not be in a steady state because a lateral flow would be driven by the much greater hydrostatic pressure under the middle of the flow.

The central region of steady flows has constant thickness and is bounded by regions of constant width, where the thickness and the surface velocity decrease considerably toward the margins (figure 7.7). If the region near the margins were behaving like a fluid,

then grains would flow down the height gradient and this could only be in steady state if there were recirculating eddies within the flow, though we have no evidence of this. If the region were plug-like, then static stresses would balance the height gradient but this appears incompatible with the surface shear (figure 7.3). A possible mechanism for balancing the lateral pressure gradient is attributed to a non-zero value in the second normal stress difference, $\sigma_{yy} - \sigma_{zz}$, where σ is the stress tensor (Tanner, 1970). A closer inspection is needed to understand the structure of the margin and its stability. We speculate that shallow flows of glass beads are unstable because they are subcritical, meaning that disturbances move faster than the beads on the surface and hence can propagate upstream (Börzsönyi *et al.*, 2008). In contrast, sand flows reported here are supercritical, suggesting that any perturbation of the flow margins decays by the arrival of fresh sand.

The margins play an important role particularly for narrow streams, which are retarded considerably by lateral stresses, as shown for $Q = 31\,\mathrm{g/s}$ in figure 7.6. There is a minimum mass flow rate for steady flow, which suggests that there is a minimum width of the flow and a minimum mass flux per unit cross-stream width. The minimum width exists because a stream of insufficient width would be unable to flow by overcoming lateral stresses exerted by static margins. We conclude that steady flows have a minimum flow rate and that our simple model describes shallow flows with flow rates greater than this minimum.

Chapter 8

Avalanches triggered at regular intervals from a steady source

8.1 Abstract

An avalanche involves the flow of granular material down a slope. Laboratory experiments are reported to show how a steady mass flux of sand from a point source can trigger avalanches down a rough inclined plane. The avalanches occur at regular intervals when the rate of supply is just below the minimum rate required for steady flow. For lower flow rates, the avalanches occur at irregular intervals. The regular avalanches maintain their shape, size and speed down the slope, that is they behave like three-dimensional solitons. We discuss the challenges associated with the mathematical treatment of the granular dynamics.

8.2 Introduction

There are numerous natural hazards featuring the flow of granular materials on mountainous terrain. Examples include rockfalls, snow avalanches (Hopfinger, 1983) and debris

flows (Davies, 1986). These natural flows have the potential to destroy everything along their path; and therefore they are a serious danger to life and infrastructure on mountains. A continuous stream often develops into a succession of waves of higher speeds and masses, which can be particularly destructive. In order to conduct hazard analysis and protect inhabited areas, for example by diverting the descending waves with barriers (Cui *et al.*, 2007; Hákonardóttir *et al.*, 2003), the size and speed of the waves must be predicted. This requires a quantitative understanding of dense granular flows (GDRMiDi, 2004). However, they are not well understood, especially in shallow layers, where flowing and static regions simultaneously exist.

Laboratory experiments have been conducted using cohesionless grains to study surface waves on shallow granular flows. Avalanches triggered suddenly on different surfaces, including a horizontal plane (Lajeunesse *et al.*, 2004; Lube *et al.*, 2004), a curved slope (Savage & Hutter, 1991; Gray *et al.*, 1999; Davies & Mcsaveney, 1999) and an erodible granular layer on a rough inclined plane (Daerr, 2001), have provided insight into the dynamics of avalanches from initiation to termination. A steady release of granular material may also result in the development of avalanches down a rough inclined plane. On gentle slopes, avalanches are triggered intermittently from the source (Lemieux & Durian, 2000; Tischer *et al.*, 2001; Félix & Thomas, 2004), when the rate of supply is below a critical value, which is examined below. On steeper slopes, longitudinal (Prasad *et al.*, 2000; Forterre & Pouliquen, 2003) and transverse (Malloggi *et al.*, 2006) instabilities develop on the flowing surface and produce avalanches down the plane. Although some wave phenomena are partly described by continuum models of granular flows (Savage & Hutter, 1989; Aranson & Tsimring, 2001; Turnbull *et al.*, 2007), it remains a challenge to understand how avalanches can continue propagating and cause severe damage along their path.

Recent experiments (Börzsönyi *et al.*, 2005; 2008) and numerical simulations (Mangeney *et al.*, 2007*b*) suggest that avalanches may travel steadily on an erodible layer down a rough inclined plane. The previous experiments were conducted by supplying grains at a constant rate evenly along the top of an inclined plane of length 220 cm and width 40 cm. Avalanches of sand with different sizes initiate intermittently and travel steadily downstream.

We report experiments here which show that avalanches of similar size can be triggered at regular intervals by releasing sand from a point source down the slope at some steady rates. In contrast to the release of grains on a horizontal surface, which results in a broad distribution of avalanche sizes on a granular heap (Abate *et al.*, 2007), the release on a rough slope within a range of slope angles can produce avalanches of approximately constant size. We discuss why the resultant flow remains a challenge to describe theoretically.

8.3 Laboratory experiments

8.3.1 Method

Experiments were carried out on a plane of length 3 m and width 1 m (figure 8.1). A layer of sand with mean size 0.45 ± 0.15 mm was glued on the plane to form a rough surface. The rough plane was supported by an aluminium framework and could be inclined by a pulley system. The inclination angle to the horizontal was measured by a digital inclinometer with an accuracy of 0.1°.

The same sand was supplied steadily at the top end of the inclined plane. A hopper of sand was connected at the bottom to a smooth pipe with a screw mechanism, which controlled the mass flow rate ranging from 5 to 218 ± 2 g/s. The pipe extended down to a V-shaped block of foam, which allowed the sand to flow down the inclined plane effectively from a point source.

The thickness of the resultant flow of sand was measured by a laser triangulator system at different positions down the inclined plane. Thickness profiles, consisting of 1024 data points along ≈ 130 mm of the centreline of the flow, were recorded every 0.04 seconds. Sand falling off the bottom end of the plane was transferred back into the hopper.

8.3.2 Results

Different types of flow arise at large times depending on the angle of inclination of the rough plane and the mass flow rate (figure 8.2). The main possible regimes are sketched in figure 8.3. The flow is dilute on steep slopes with angle greater than approximately 38 degrees. On more gentle slopes, dense granular flows develop in a shallow layer. On slopes ranging in angle between approximately 33 and 38 degrees, the flow is dense and unsteady because roll waves develop on the flowing surface (Forterre & Pouliquen, 2003), which can result in avalanches far downstream. On any slope ranging in angle between 31 and 33 degrees, the flow is dense and steady provided that the flow rate is above a critical value. The minimum flow rate required for steady flow increases sharply as the slope angle is reduced. When the flow rate is lower than and close to this minimum, avalanches are triggered at regular intervals, which are examined further in this section.

The current investigation provides a foundation for studying the more complicated regime of avalanches which are triggered at irregular intervals when the flow rate is further reduced or when the rough plane is less inclined. At flow rates far below the critical rate required for steady flow, most avalanches eventually stop and form a thick erodible

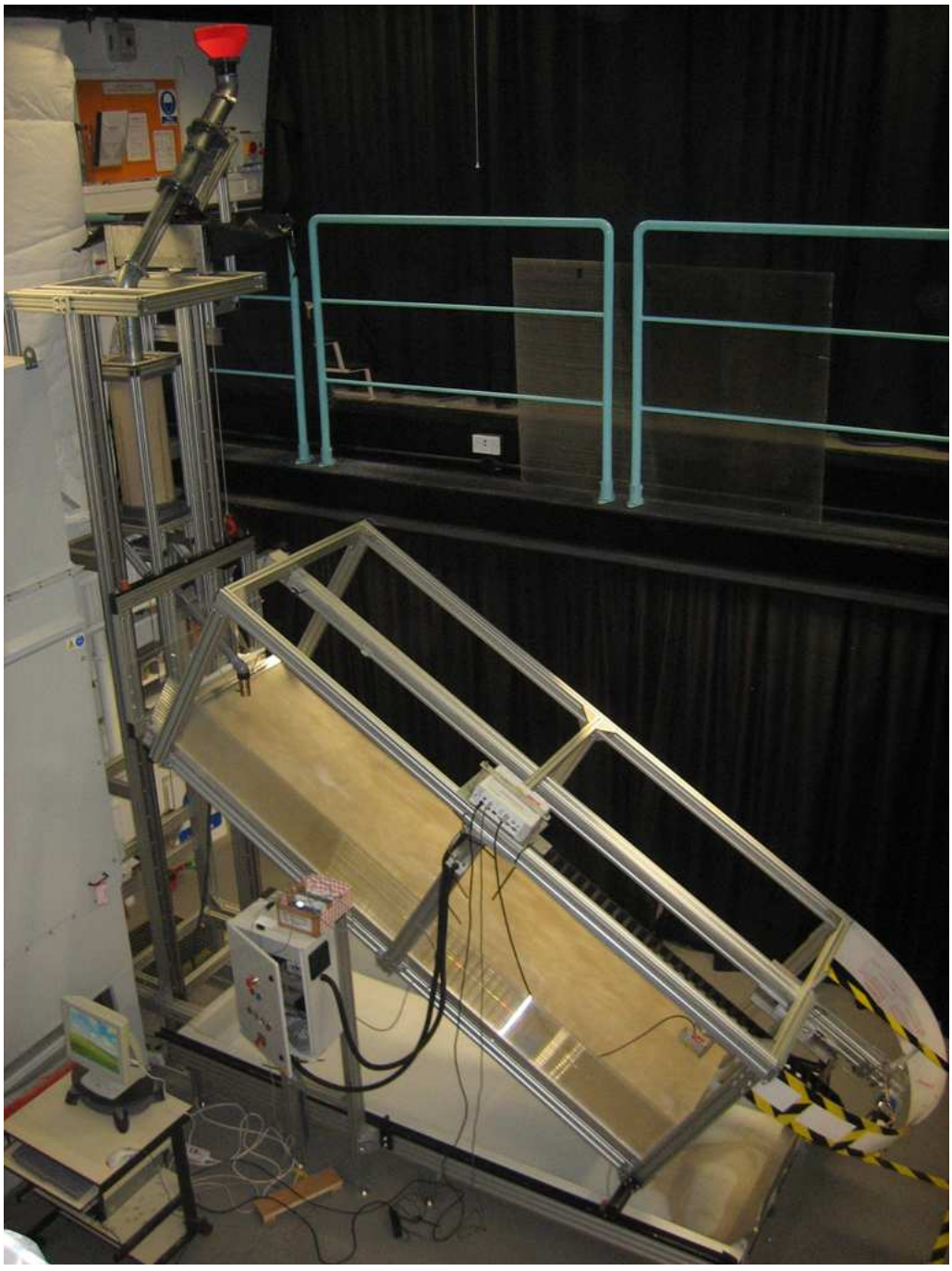

Figure 8.1: *Photograph of the experimental configuration. The rough inclined plane is supported by an aluminium structure.*

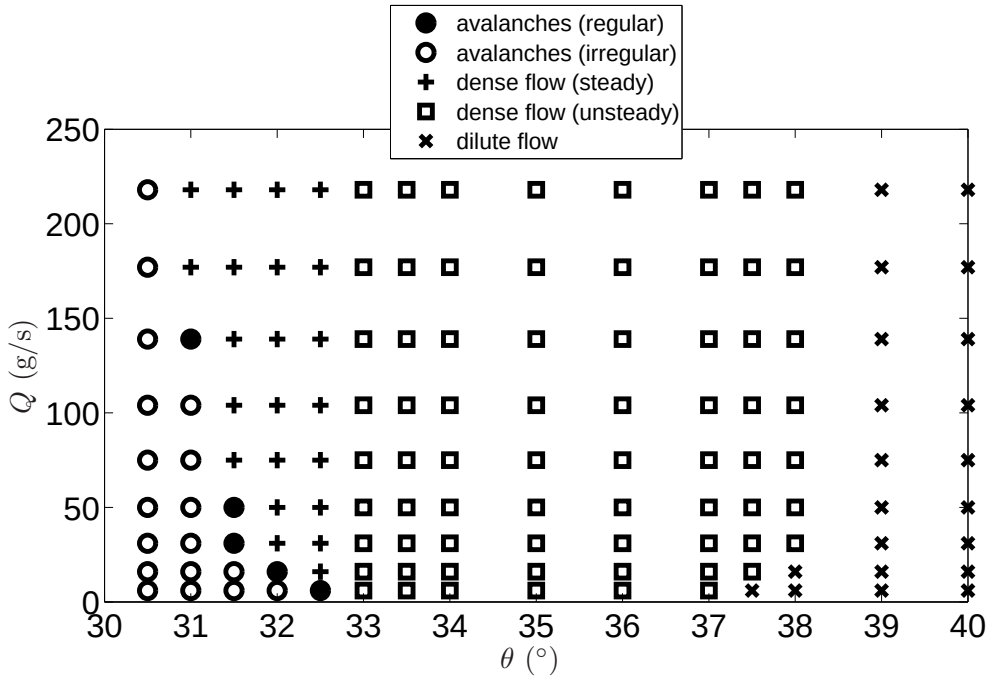

Figure 8.2: *Regime diagram showing the different types of flow as a result of a supply at a steady rate Q down a rough plane inclined at an angle θ to the horizontal. Avalanches are triggered at regular or irregular intervals down gentle slopes with $\theta < 33$ degrees when the flow rate is small. At larger flow rates, dense granular flow develops and remains steady. On steeper slopes, the dense flow becomes unsteady downstream as roll waves develop.*

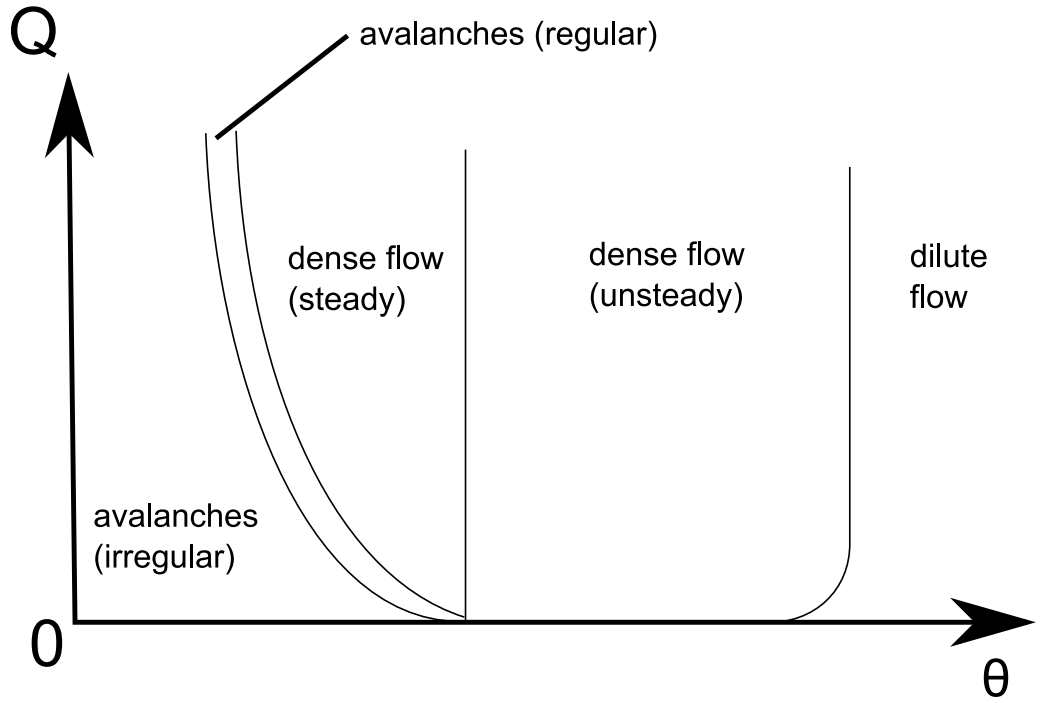

Figure 8.3: *A sketch of the salient regimes in figure 8.2. The regime of regular avalanches, as investigated here, marks the boundary between irregular avalanches and dense steady flow.*

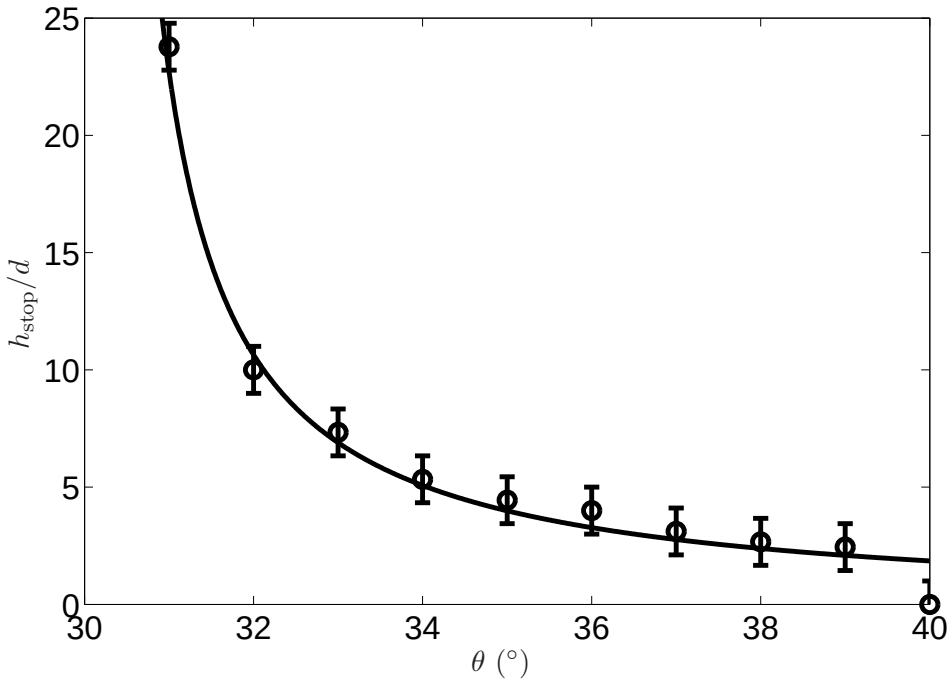

Figure 8.4: *The thickness of the deposit on the rough plane, scaled by the mean size of individual grains ($d \approx 0.45\,mm$), as a function of the slope of the plane. The line is given by (8.1) with $a = 0.48$ and $\theta_1 = 30.1°$.*

layer down the slope. Subsequent avalanches stop closer to the source until a massive avalanche is triggered, eroding the thick layer and reaching the end of the slope. Although this unsteady system may eventually reach a time-periodic state, avalanches are initially triggered at irregular intervals. We instead examine a simpler time-periodic state which arises when sand is supplied at a rate close to and below the critical rate required for steady flow.

Pulses of avalanches are triggered at approximately regular intervals in the following manner. First, a relatively deep pile of sand grows near the source. After some time, an avalanche is triggered and propagates down the incline in a solitary wave. The avalanche leaves behind a layer of deposit at rest and erodes any static layer ahead of the front. The avalanche comes to a halt when there is no more erodible layer of sand ahead of the flow. In this manner, an erodible layer of static sand is produced and extends down the incline. Successive avalanches are triggered and propagate down the incline on the erodible layer, produced by the deposit of earlier avalanches.

The thickness of the deposit is related to the following phenomenon. When the supply of grains required for steady flow down a slope is turned off, the flow gradually stops and deposits a layer on the inclined plane. The thickness of the final deposited layer depends on the angle of inclination of the plane as shown in figure 8.4. The thickness for the

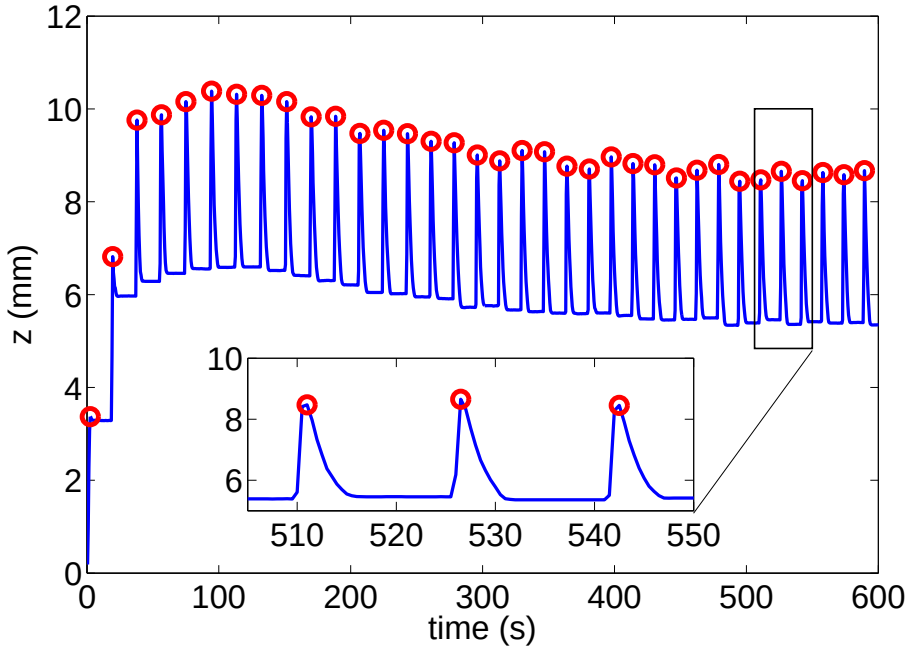

Figure 8.5: *A plot of the mean thickness of the layer of sand 2 m down the incline from the source, averaged over half-second intervals near the beginning of an experiment with $q = 16\,g/s$ and $\theta = 32°$. Time begins from the moment when the first avalanche reaches the 2 m mark. The local maxima are represented by circles and correspond to the arrival of avalanches. Note that the minimum thicknesses are greater than h_{stop} during the transient phase.*

moderate range of inclination angles, bounded by approximately 31 and 39 degrees, is well described by a curve of the form (Börzsönyi *et al.*, 2008)

$$\frac{h_{\text{stop}}}{d} = \frac{a}{\tan\theta - \tan\theta_1}, \tag{8.1}$$

where $a = 0.48$ and $\theta_1 = 30.1°$ are dimensionless parameters. A layer of thickness less than h_{stop} is unable to flow. We discuss later how h_{stop}, which characterises the roughness and the slope of the inclined plane, appears in the condition for regular avalanches to develop.

The intervals in time between the arrival of successive avalanches can be computed readily by measuring the thickness of sand down the inclined plane. A representative set of results is presented for sand released at $q = 16\,\text{g/s}$ down a 32° slope. Figure 8.5 shows an evolution of the mean thickness of the layer of sand 2 m down the slope. The local maxima are represented by circles and correspond to the arrival of avalanches. The local minima correspond to the static layer that is deposited following the passage of avalanches. The mean and standard deviation of twenty intervals in time between the arrival of successive avalanches are shown in figure 8.6. The intervals decrease slowly with time until approximately 50 minutes into the experiment. The intervals remain close to

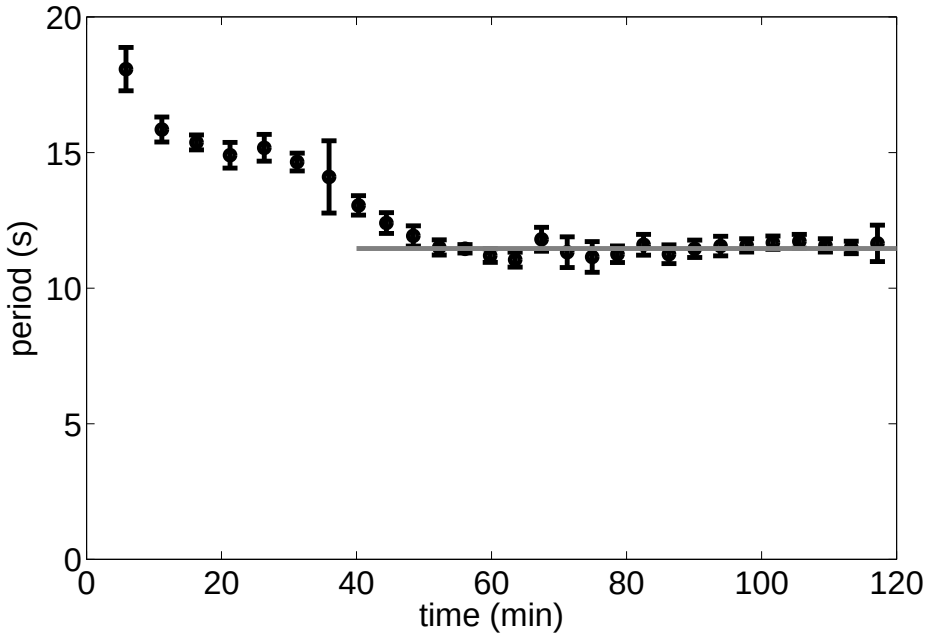

Figure 8.6: *The time interval between the arrival of successive avalanches plotted against time. Each data point is the mean period of twenty successive avalanches. The error bars show the standard deviation of the period of the same twenty avalanches. After approximately 50 minutes, the period remains close to 11.5 seconds, as marked by the horizontal line. This indicates that avalanches arrive at regular intervals in the long-time limit.*

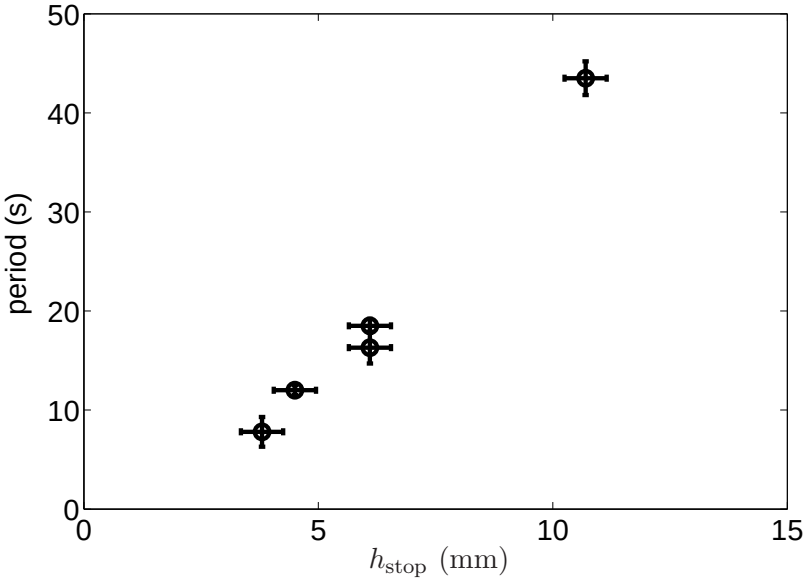

Figure 8.7: *Period of avalanches triggered at regular intervals increases with h_{stop}. This means that the interval between successive avalanches is longer down a more gentle slope.*

11.5 seconds subsequently, indicating that avalanches arrive at regular intervals in the long time limit.

The regular interval between successive avalanches at large times increases on a gentler slope, which is associated with an increase in h_{stop}, as shown in figure 8.7. Moreover, an increase in h_{stop} increases the minimum flow rate required for steady flow as shown in figure 8.8. This means that the mass of grains in each avalanche, which is the product of the interval and the steady rate of supply at the source, increases sharply with h_{stop}. Avalanches initiated at regular intervals are more massive and occur less frequently on more gentle slopes.

The shape, size and speed of an avalanche are computed from thickness profiles at successive times which are translated steadily along the slope. The translation speed c and the mean thickness profile f are obtained by minimising a measure of deviations of the translated profiles,

$$\sum_i \sum_j [h(x_i, t_j) - f(x_i - ct_j)]^2, \tag{8.2}$$

where h represents data recorded at discrete positions x_i and times t_j. The speed corresponds to the wave speed of avalanches, based on the assumption that avalanches retain their shape and size as they travel steadily, as verified below. The computed speeds are consistent with images captured by a high-speed camera, which offers an alternative method of computing the speed of avalanches.

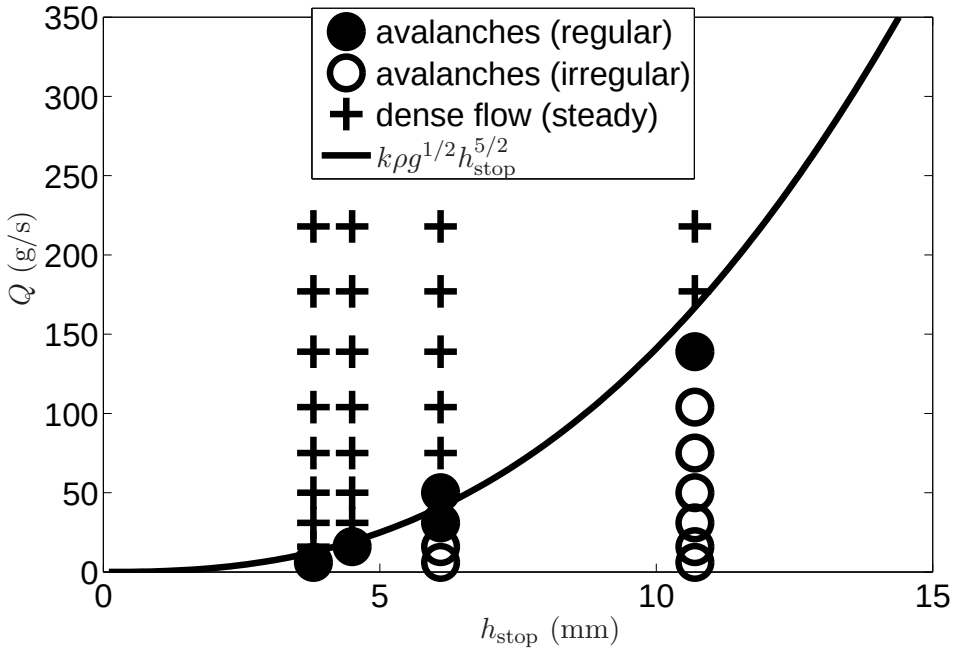

Figure 8.8: *The minimum flow rate required for steady flow is estimated by (8.6), where the constant of proportionality $k \approx 3$.*

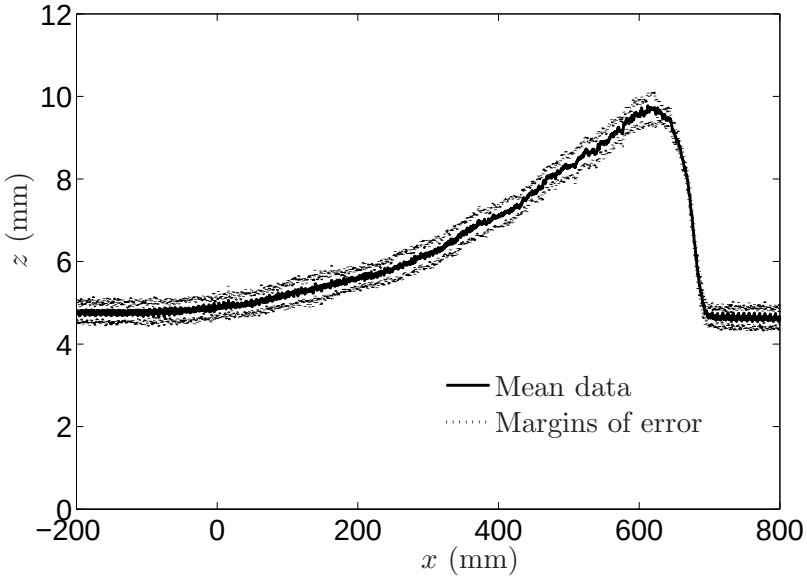

Figure 8.9: *Thickness profile of an avalanche 2 m down a 32° slope. The margins of error of the experimental data represent one standard deviation about the mean profile due to fluctuations in the flow.*

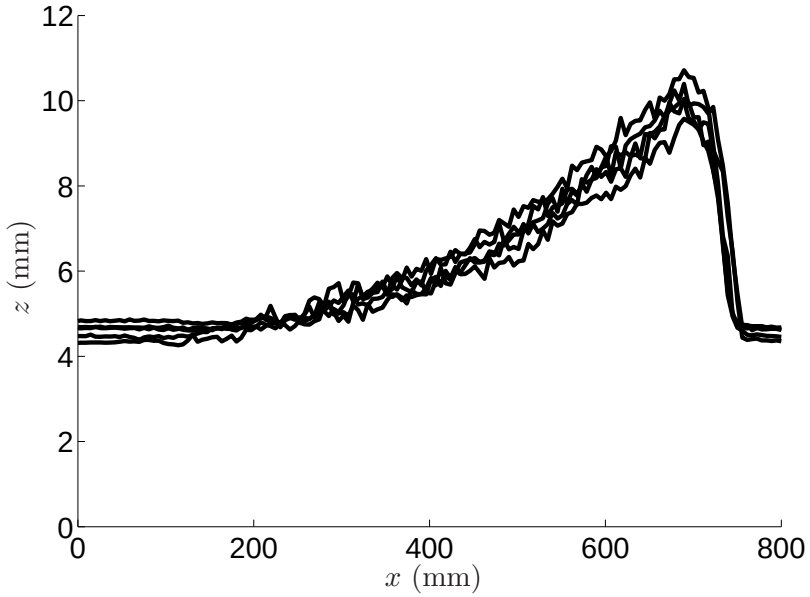

Figure 8.10: *Thickness profiles of five successive avalanches 2 m down a 32° slope. The overlap of the mean profiles suggests that the successive avalanches have the same shape and size.*

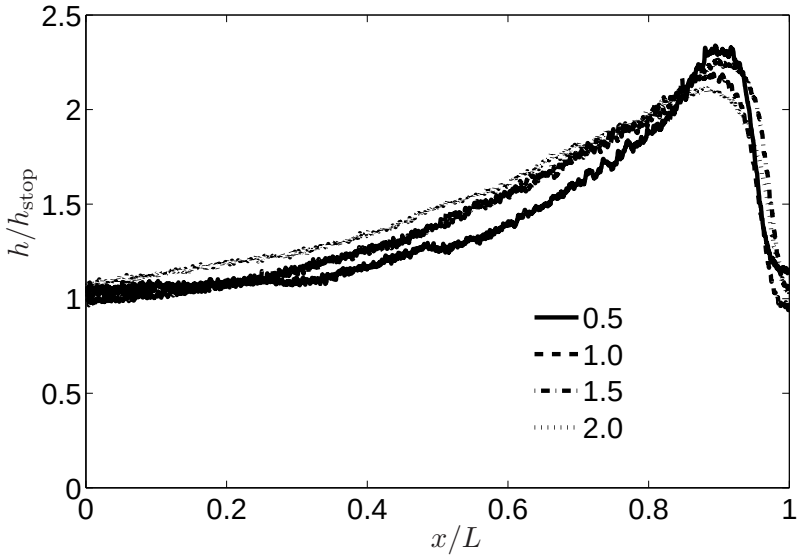

Figure 8.11: *Dimensional thickness profile of representative avalanches at 0.5 m, 1.0 m, 1.5 m and 2.0 m down a 32° slope. The horizontal length is scaled by $L \approx 700$ mm and the vertical length is scaled by $h_{\mathrm{stop}} \approx 4.5$ mm. The mean profiles almost overlap, suggesting that avalanches retain their shape and size as they propagate downstream.*

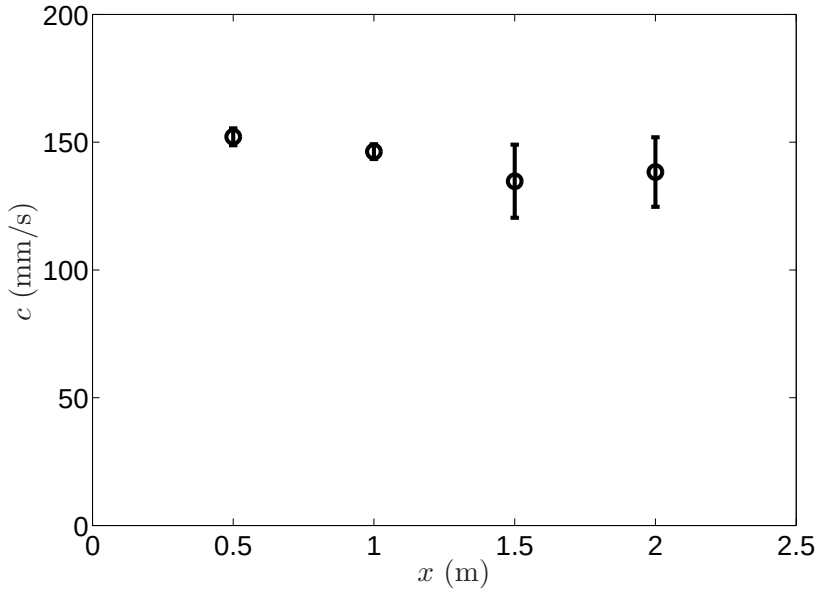

Figure 8.12: *Mean and standard deviation of the wave speed of ten representative avalanches at different extents down a 32° slope. The speed of each avalanche remains approximately constant during the course of its propagation. Variations in the wave speed are smaller closer to the source.*

The shape and size of avalanches are presented in the representative case of sand supplied at a rate of $q = 16\,\mathrm{g/s}$ down a 32° slope. The thickness profile of a representative avalanche 2 m down the slope is shown in figure 8.9. The thickness increases sharply at the front and decreases gently towards the back of the wave. The margins of error are attributed to flow fluctuations, which are represented by one standard deviation above and below the mean curve. Figure 8.10 shows the thickness profile of five successive avalanches, which collapse with errors comparable to the flow fluctuations. This indicates that avalanches of similar shape and size travel down the slope. Figure 8.11 shows the thickness profile of representative avalanches at different extents down the slope. The profiles indicate that avalanches do not change appreciably in shape or size as they travel down the slope. The speed of wave propagation is approximately constant as indicated by figure 8.12.

The dimensionless wave speed is plotted against the maximal thickness attained near the front of avalanches on different slopes in figure 8.13. The wave speed c is scaled by $\sqrt{gh_{\mathrm{stop}}\cos\theta}$ and the maximal thickness h_f by h_{stop}. Avalanches initiated at regular intervals from a point source down different slopes with θ ranging between 31 and 32.5 degrees, as investigated here, have approximately constant wave speed, $c = 0.6 \pm 0.1$. These avalanches are generally slower in speed and closer in thickness to h_{stop} than the avalanches triggered from a steady line source on steeper slopes with θ ranging between 32 and 41 degrees (Börzsönyi *et al.*, 2005).

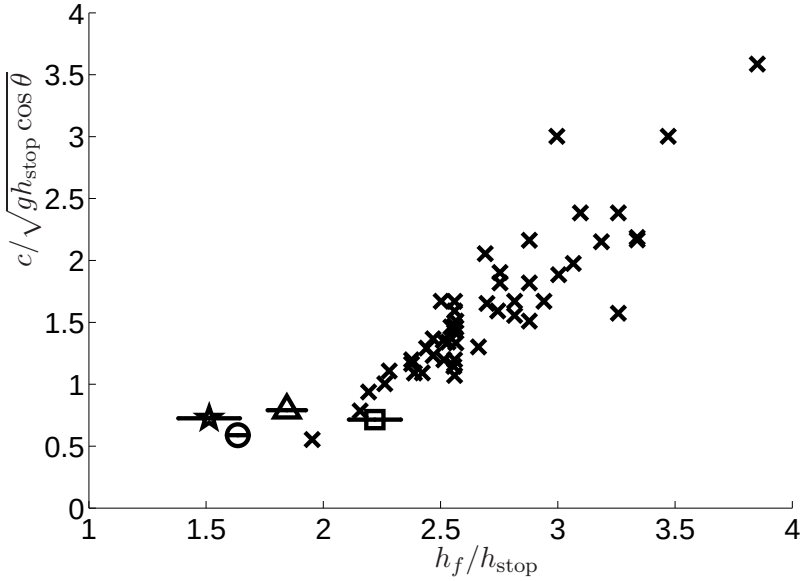

Figure 8.13: *Dimensionless wave speed plotted against dimensionless thickness of the wave front. Symbols with horizontal error bars represent the mean speed of several avalanches initiated at regular intervals from a point source down a slope with angle 31.0° (◯), 31.5° (△), 32.0° (□) and 32.5° (⋆). Vertical error bars are shorter than the size of the symbols. Crosses represent avalanches initiated at irregular intervals from a line source on slopes ranging between 32 and 41 degrees, reproduced from figure 2b of Börzsönyi* et al. *(2005).*

8.4 Discussion

Simple ideas are developed below to estimate the condition for avalanches to be triggered at regular intervals from a steady source, as observed in the experiments. We then discuss some challenges associated with the mathematical treatment of the dynamics of avalanches.

The granular flows considered here pose theoretical challenges partly because the thickness of the flows is not much greater than h_{stop}. Shallow granular flows are not as well understood as deep flows where the thickness is much greater than h_{stop}. For $h \gg h_{\mathrm{stop}}$, the depth-averaged velocity u of the flow is given by the empirical flow rule

$$\frac{u}{\sqrt{gh}} = \alpha + \beta \frac{h}{h_{\mathrm{stop}}}, \tag{8.3}$$

where α and β are dimensionless parameters which depend on the granular material (Pouliquen, 1999). Materials commonly used in the laboratory are sand ($\alpha = -0.77$, $\beta = 0.65$) and glass beads ($\alpha = 0$, $\beta = 0.14$) (Forterre & Pouliquen, 2003). Shallow granular flows including avalanches, which are confined by static margins as they develop down open slopes, have thickness comparable by order of magnitude to h_{stop} and are not described by (8.3).

In order to study the flow rates resulting in avalanches at regular intervals, we consider the minimum flow rate required for steady flow. When the flow rate is far above this minimum, a steady flow develops with thickness h much smaller than the width w of the flow down the inclined plane. The flow is sheared predominantly across its thickness and remains steady down the slope. At larger flow rates, the thickness h remains comparable by order of magnitude to h_{stop}, which is written as $h \sim h_{\mathrm{stop}}$. The dominant length scale of the system is h_{stop}. The other physical quantities with dimensional units are gravity g and the mass flow rate Q, which primarily changes the width of the flow only. It follows by dimensional analysis that a suitable scale for the downstream velocity is given by

$$u \sim \sqrt{g h_{\mathrm{stop}}}. \tag{8.4}$$

By mass conservation, the mass flow rate

$$Q \sim \rho u w h_{\mathrm{stop}}, \tag{8.5}$$

where $\rho \approx 1.5\,\mathrm{kg/m^3}$ is the density of sand. The condition for steady flow is $w \gg h_{\mathrm{stop}}$, which is equivalent to $Q \gg Q_c$, where

$$Q_c \sim \rho g^{1/2} h_{stop}^{5/2} \tag{8.6}$$

is obtained by combining (8.4) and (8.5). Below this critical flow rate, it is not possible to sustain a steady flow with comparable width and thickness. Such a flow would be resisted by lateral stresses and eventually stop. Instead, avalanches are triggered when a sufficient mass of grains accumulates near the source. Figure 8.8 shows that (8.6) is consistent with experiments.

There are some aspects of the experiments which are not fully understood. A feature of the avalanches triggered at regular intervals is that the dimensionless wave speed is constant on different slopes. Unlike avalanches triggered intermittently from a line source, the avalanches triggered at regular intervals from a point source vary in dimensionless thickness but not in dimensional speed as the slope angle θ changes. The maximal thickness attained near the front of the wave is $h_f = \gamma h_{\mathrm{stop}}$, where $\gamma = 1.9 \pm 0.5$ depends on θ as shown in figure 8.13. This means that avalanches have an explicit dependence on θ in addition to the implicit dependence through h_{stop}, which is further evidence that a relation like (8.3) fails for shallow flows. The function $\gamma(\theta)$ is not monotonic and not well understood. Another feature of the avalanches is that they travel steadily like three-dimensional solitons, retaining their shape and size. Dispersive effects due to down-slope variations in thickness may be countered by nonlinear effects due to wave steepening. However, it is surprising that cross-slope variations in thickness, which would cause fluids

to disperse across the main flow, do not cause the avalanche to spread laterally and evolve downstream. This may relate to the possibility for steady granular flows at larger flow rates to feature lateral variations in thickness near the margins.

Further insight into the experimental observations could be gained by the development of a mathematical model of avalanches, but this is far from straightforward. One possible approach is to move into the reference frame of an avalanche and consider the flowing region using a depth-averaged model of shallow granular flow, conserving mass and momentum down the slope (Savage & Hutter, 1989). This simplified approach neglects lateral variations and the vertical structure of the avalanche. These features may play an important role particularly near the interface between the flowing and static regions. It is beyond the scope of the present analysis to study the exchange of mass across the interface due to erosion and deposition of grains. A better understanding of these processes would be helpful for developing a model, which predicts and explains the dynamics of avalanches observed in the experiments.

Chapter 9

Nonlinear peristaltic waves in an elastic tube

9.1 Abstract

Nonlinear waves of fluid are driven in an elastic tube by imposing a radial force of sinusoidal form. The governing equations of the deformation of the tube and the flow rate inside the tube are derived using linear elasticity theory and lubrication theory. Steady and periodic solutions in the reference frame of a steadily propagating wave are obtained by either asymptotic theory in the two regimes of small and large forcing amplitudes or numerical techniques for moderate forcing amplitudes, respectively. A strongly deformed tube of Newtonian fluid is shown to feature an occluded region and a peak region, which depends weakly on the large forcing amplitude. The flow rate inside the tube reduces significantly when the fluid has a yield stress, as investigated using a Bingham plastic model. The flow of Newtonian fluid containing a rigid rod in the tube shows that a maximal speed of the rod is attained by imposing a radial force of moderate amplitude. The rod generally declines in speed with increasing radius, suggesting that the python, which must take in food by peristalsis without grinding into smaller pieces, has a bitter pill to swallow.

9.2 Introduction

Fluid inside a deformable tube can be driven by the mechanism of peristaltic action. Many biological ducts convey contents, including a bolus in the gastronomical duct and urine in the ureter, by propagating waves of muscular contraction and relaxation. A python is able to swallow prey of considerable size this way. A related type of flow in a deformed tube occurs in peristaltic pumps, which are used for the infusion of medication into the circulatory system and the treatment of wastewater in the environment, amongst many other applications. Pushing toothpaste out of its tube is another example of relevance.

Mathematical models of peristaltic motion can be developed using lubrication theory, provided that effects due to fluid inertia are negligible. The low-Reynolds-number flow of Newtonian fluid was described in an axisymmetric tube with either a sinusoidal (Shapiro *et al.*, 1969) or non-sinusoidal (Lykoudis & Roos, 1970) deformation in its radius. The flow of non-Newtonian fluid was studied in a similar fashion, given a small deformation in the tube radius (Frigaard & Ryan, 2004; Vajravelu *et al.*, 2005). Another variation is to introduce a peripheral layer of Newtonian fluid adjacent to the wall, which has a different viscosity from that of the inner fluid (Brasseur *et al.*, 1987). These models prescribe the tube deformation without taking elastic properties of the tube into consideration.

Of interest is a situation where the shape of the tube is unknown a priori and must be solved as part of the problem, given some coupling between the hydrodynamics and the mechanics of the elastic tube. Related free-boundary problems of flow near an elastic material arise in a range of contexts, including the swimming of a microorganism near a rigid wall (Argentina *et al.*, 2007; Balmforth *et al.*, 2010) and premelting of ice in a deformable capillary (Wettlaufer & Worster, 1995; Wettlaufer *et al.*, 1996). In the context of peristaltic motion with a prescribed activation wave of muscular contraction, where elastic tubes result in finite-amplitude deformations, tubes containing Newtonian fluid (Carew & Pedley, 1997) and a rigid bolus (Bertuzzi *et al.*, 1983) have been solved numerically. Analytic solutions are desirable for gaining a deeper understanding of peristaltic flow inside a strongly deformed tube, where the response in tube radius is a nonlinear function of the forces driving the flow.

Here, theoretical models of peristaltic flow are developed, given a sinusoidal wave of radial force of arbitrary amplitude that translates along an elastic tube. In the reference frame of the wave, steady and periodic solutions are obtained to describe the motion of three different materials inside the tube. In section 9.3, the flow of Newtonian fluid is investigated inside a linearly elastic tube and separately inside a tube of finite bending stiffness. In section 9.4, the flow governed by a Bingham plastic model is considered, which exhibits the dual behaviour of a fluid and a solid. Familiar examples of non-Newtonian fluid

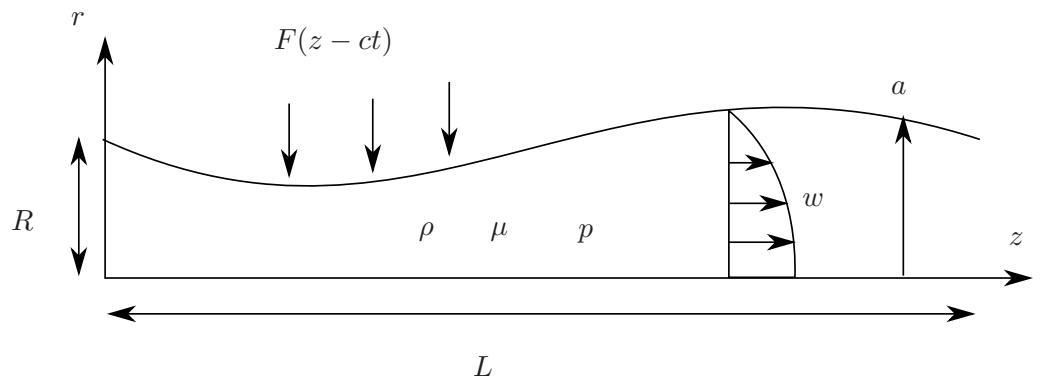

Figure 9.1: *Sketch in cylindrical polar coordinates of a deformed tube filled with Newtonian fluid. A prescribed radial force F perturbs the tube of radius a and induces flow with axial velocity w.*

described by the Bingham model include mud, paint, slurry, and toothpaste. In section 9.5, the propulsion of a rigid body in a Newtonian fluid is examined. The coupled motion of the solid and the fluid provides useful insight into the flow of pills in the gastronomical duct, kidney stones in the ureter, and blood cells in small blood vessels. In each section, the governing equations are derived and solved using asymptotic theory in the two regimes of small and large forcing amplitudes, which give rise to linear and nonlinear responses in tube radius respectively. The theoretical results are complemented by numerical solutions that describe responses to moderate forcing amplitudes.

9.3 Newtonian fluid

Consider a Newtonian fluid of density ρ and dynamic viscosity μ with pressure p_0, inside a cylindrical tube of constant radius R in its undeformed state. A radial force per unit area of sinusoidal form $F(z-ct) = \eta \sin[(z-ct)2\pi/L]$ is applied on the tube along the axial coordinate z at time t. The imposed force, characterised by its amplitude η, steady speed c, and wavelength L, perturbs the pressure p inside the tube and the tube radius a, as sketched in figure 9.1. The velocity $\mathbf{u}$ of the induced flow of fluid is governed by

$$\rho \frac{D\mathbf{u}}{Dt} = -\nabla p + \mu \nabla^2 \mathbf{u}, \tag{9.1}$$

subject to the condition of incompressibility,

$$\nabla \cdot \mathbf{u} = 0. \tag{9.2}$$

The elastic properties of the tube are such that the change in pressure across the tube is of the form

$$D \frac{\partial^n}{\partial z^n}(a - R) + F, \tag{9.3}$$

where $n = 0$ or 4 characterises the type of elastic material constituting the tube and D denotes its stiffness. The case of $n = 0$ corresponds to a linearly elastic tube such that its deformation is proportional to the net radial force. For example, the tube could be attached by springs to a rigid surrounding backing, where D is the spring constant. The case of $n = 4$ corresponds to a thin shell of bending stiffness $D = h^3E/12(1 - \nu^2)$, where h is the shell thickness, E the Young modulus and ν the Poisson ratio (Love, 1944). The objective is to determine the shape of the tube and the volumetric flow rate q per wave period, L/c.

It is convenient to introduce dimensionless variables of axial coordinate $z' = z/L$, radial coordinate $r' = r/R$, time $t' = tc/L$, pressure $p' = pR/\mu c$, tube stiffness $D' = DR/\mu c$, amplitude of forcing $\eta' = \eta R/\mu c$, and flow rate $q' = q/\pi R^2 c$. All quantities from here onwards are dimensionless, without the primes for simplicity. In addition, it is convenient to formulate the problem in the reference frame of the wave, moving at speed 1 in the z direction. The advantage of moving with the wave is that the tube radius is steady in time in this reference frame, as justified below. The axial velocity w and radial velocity u are governed by (9.1)

$$\delta^2 Re\frac{Du}{Dt} = -\frac{\partial p}{\partial r} + \delta^2\frac{1}{r}\frac{\partial}{\partial r}\left(r\frac{\partial u}{\partial r}\right) + \delta^4\frac{\partial^2 u}{\partial z^2} \tag{9.4}$$

and

$$Re\frac{Dw}{Dt} = -\frac{\partial p}{\partial z} + \frac{1}{r}\frac{\partial}{\partial r}\left(r\frac{\partial w}{\partial r}\right) + \delta^2\frac{\partial^2 w}{\partial z^2}, \tag{9.5}$$

where

$$\delta \equiv \frac{R}{L} \tag{9.6}$$

is the aspect ratio of the region of interest and

$$Re \equiv \frac{\rho c R^2}{\mu L} \tag{9.7}$$

is the Reynolds number. The deformation of the tube is small provided that $\delta \ll 1$ under the long-wave approximation. Inertia is negligible compared to viscous forces provided that $Re \ll 1$. It is natural to seek steady solutions in the wave frame because the explicit dependence on time is dropped by neglecting effects due to inertia. Under these approximations of lubrication theory, the leading-order equation of (9.4) indicates that the pressure inside the tube is uniform in the radial direction. Consequently, (9.3) is equal to $p - p_0$ so

$$\frac{dp}{dz} = D\frac{d^{1+n}a}{dz^{1+n}} + \eta\cos z, \tag{9.8}$$

by differentiating (9.3) with respect to z. The leading-order equation of (9.5) gives rise to

a second-order differential equation for the axial velocity w,

$$\frac{dp}{dz} = \frac{1}{r}\frac{\partial}{\partial r}\left(r\frac{\partial w}{\partial r}\right). \tag{9.9}$$

The associated boundary conditions are $w = -1$ on $r = a$, by the condition of no slip on the tube wall, and $\partial w/\partial r = 0$ on $r = 0$, by either regularity or axisymmetry of the flow. Note that $w = -1$ in the wave frame corresponds to no axial flow in the lab frame. Integrating (9.9) twice and imposing the two boundary conditions yield the velocity profile in the wave frame,

$$w = \frac{1}{4}\frac{dp}{dz}(r^2 - a^2) - 1. \tag{9.10}$$

Streamlines are determined by contours of the streamfunction

$$\psi = -\frac{1}{16}\frac{dp}{dz}r^2(2a^2 - r^2) - \frac{1}{2}r^2, \tag{9.11}$$

which is obtained by integrating $w = r^{-1}\partial\psi/\partial r$.

A measure of the proportion of fluid propagating with a wave is given by the time-averaged flow rate in the lab frame, πq, where $q = 1+2\int_0^a wr\,dr$. The integral corresponds to the flow rate in the wave frame. The constant 1 is attributed to frame advection. Note that the global conservation of fluid volume implies

$$\langle a^2\rangle = 1, \tag{9.12}$$

where $\langle\cdot\rangle \equiv (2\pi)^{-1}\int_0^{2\pi}\cdot\,dz$. The time-averaged flow rate in the lab frame is proportional to

$$q = -\frac{1}{8}\frac{dp}{dz}a^4 - a^2 + 1, \tag{9.13}$$

where dp/dz is given by (9.8). When $n = 0$ in (9.8), the first-order differential equation (9.13) must be solved subject to the periodic boundary condition $a(0) = a(2\pi)$. When $n = 4$ in (9.8), the fifth-order differential equation (9.13) must be solved subject to periodic boundary conditions $d^ia/dz^i(0) = d^ia/dz^i(2\pi)$ for $i = 0, 1, 2, 3, 4$. A boundary-value problem with an eigenvalue to be determined, q, must be solved to determine the radius of the tube.

The system of equations, (9.12) and (9.13), can be solved numerically using a built-in function of Matlab called bvp4c. The forcing amplitude η is incremented slowly from 0 with $a = 1$ to obtain a solution during each iteration, which forms an initial guess for solutions with successive increments of η. A representative set of solutions for the tube radius in response to different forcing amplitudes η is plotted in figure 9.2. The associated solutions of the eigenvalue q are presented later. For small η, the tube deformation is small

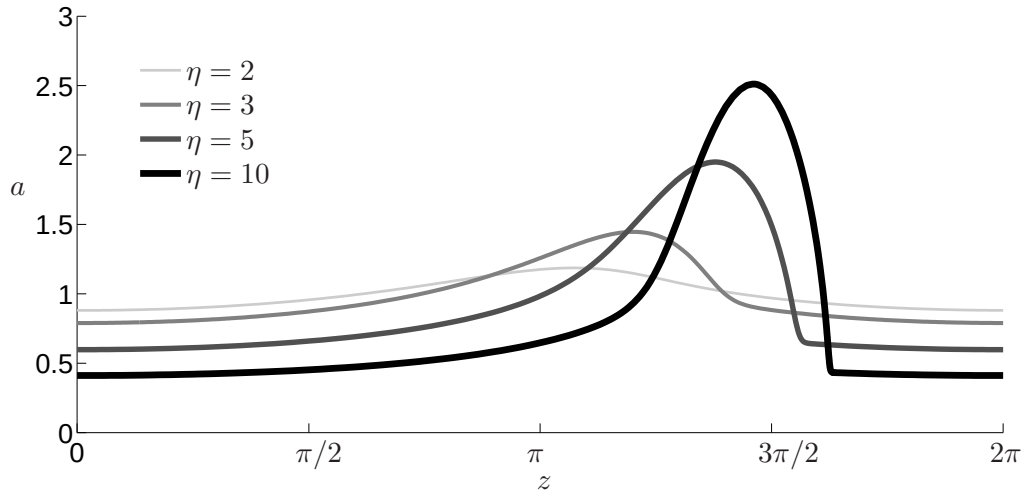

Figure 9.2: *Numerical solutions of the tube radius perturbed by different forcing amplitudes η. The tube is of type $n = 0$ and has stiffness $D = 1$. As η increases, the deformation of the tube increases.*

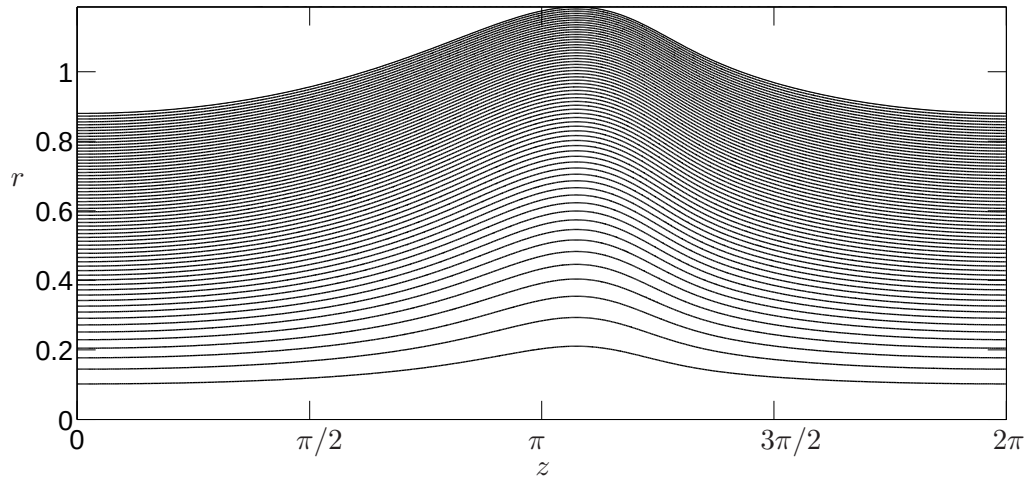

Figure 9.3: *Streamlines of flow driven by a radial force of amplitude $\eta = 2$. In the wave frame, the axial velocity inside the tube is everywhere negative.*

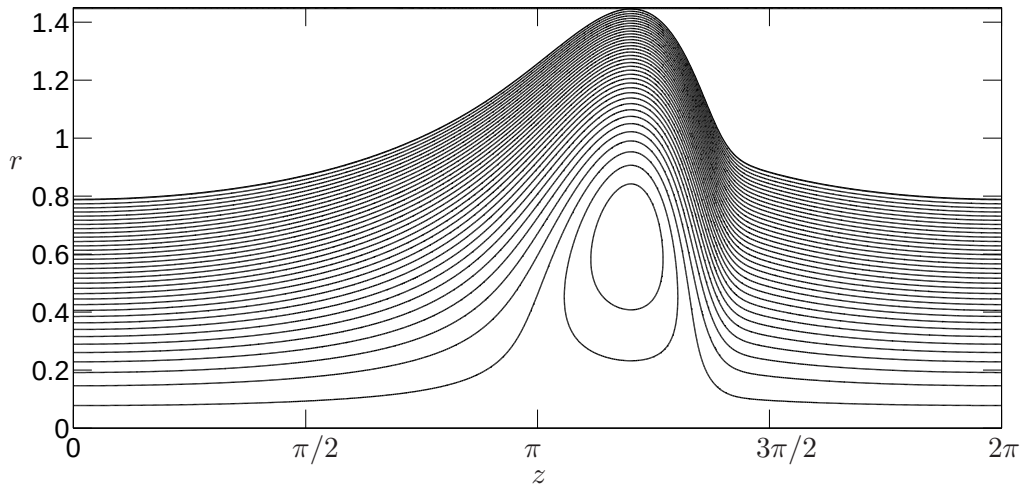

Figure 9.4: *Streamlines of flow driven by a radial force of amplitude $\eta = 3$. In the wave frame, a trapped core, recirculating anti-clockwise, forms in the region where a peak radius of the tube is attained.*

as expected. As η increases, the tube is occluded except near $z = 3\pi/2$, where its radius peaks due to the imposed force that is maximal and radially outward. Streamlines of the flow induced with forcing amplitudes $\eta = 2$ and $\eta = 3$ are shown in figures 9.3 and 9.4, obtained using equation (9.11). As η increases, a qualitative change in the structure of the streamlines is observed, from axial flow that is everywhere negative in the wave frame to the development of a recirculating zone where the tube peaks in radius. Fluid inside the recirculating zone propagates with the wave.

In the limit as $\eta \to 0$, the tube is almost undeformed and flow inside the tube is expected to be negligible. In the limit as $\eta \to \infty$, the trapped core near $z = 3\pi/2$ is expected to increase in size and allow most of the fluid in the tube to propagate with the wave. The two regimes of small and large η are investigated separately using asymptotic theory.

In the small-amplitude regime, $\eta \ll 1$, it is fruitful to seek series solutions of a and q about the base state, $a = 1$ and $q = 0$. The subsequent term in a is of order η, which indicates that the leading term in q is of order η^2, by operating $\langle\cdot\rangle$ on (9.13) and using the integral constraint (9.12). The radius of the tube responds linearly to the amplitude of the external forcing. Substituting $a = 1 + \eta a_1 + o(\eta^2)$ into (9.13) gives

$$D\frac{d^{1+n}a_1}{dz^{1+n}} - 16a_1 = \cos z, \tag{9.14}$$

which is solved subject to periodic boundary conditions. The solution is given by

$$a = 1 - \eta\frac{16\cos z - D\sin z}{16^2 + D^2} + o(\eta^2), \tag{9.15}$$

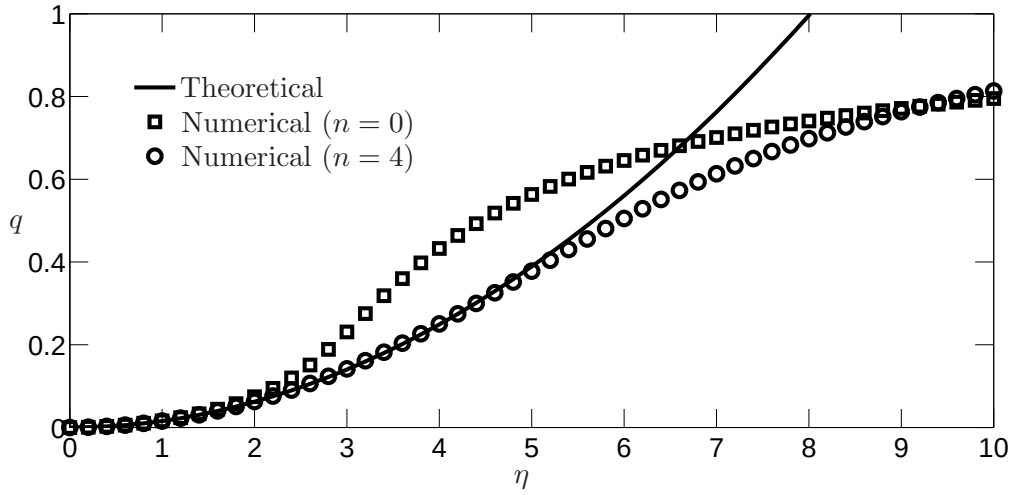

Figure 9.5: *Theoretical prediction and numerical solutions of the time-averaged flow rate in the lab frame for small forcing amplitudes η. The numerical solutions are obtained with tube stiffness $D = 1$ and agree with the theoretical prediction in the asymptotic limit as $\eta \to 0$, independent of the type of tube, $n = 0, 4$.*

independent of the type of tube characterised by $n = 0, 4$ because $\sin z$ and $\cos z$ are invariant under four differentiations. Operating $\langle\cdot\rangle$ on (9.13), which gives $q = -\langle (dp/dz)a^4/8\rangle$, and imposing periodic boundary conditions at $z = 0, 2\pi$, yield an expression for the time-averaged flow rate,

$$q = \frac{4\eta^2}{16^2 + D^2} + o(\eta^3), \tag{9.16}$$

which is in agreement with numerical results for small η as shown in figure 9.5. Note that the theoretical prediction given by (9.16) in the asymptotic limit as $\eta \to 0$ agrees with numerical results up to $\eta \approx 2$ inside a tube of type $n = 0$ and up to $\eta \approx 5$ inside a tube of type $n = 4$. The numerical results in the figure suggest that q approaches 1 as η increases, which is investigated below.

In the large-amplitude regime, $\eta \gg 1$, two qualitatively distinct regions develop, one near $z = 3\pi/2$ where the tube radius peaks, and the other away from $z = 3\pi/2$ where the tube is occluded. Quantitative details of the two regions must be considered separately in the two types of tubes, $n = 0$ and $n = 4$. Of interest is the quantity $1 - q$, a measure of the proportion of fluid left behind the wave.

When $n = 0$, the tube radius is expected to approach 0 in the occluded region so the dominant contribution to dp/dz in (9.13) arises from the second rather than the first term on the right hand side of (9.8). The governing differential equation (9.13) reduces to an algebraic equation

$$-\eta \cos z\, a^4 - 8a^2 + (1 - q) = 0. \tag{9.17}$$

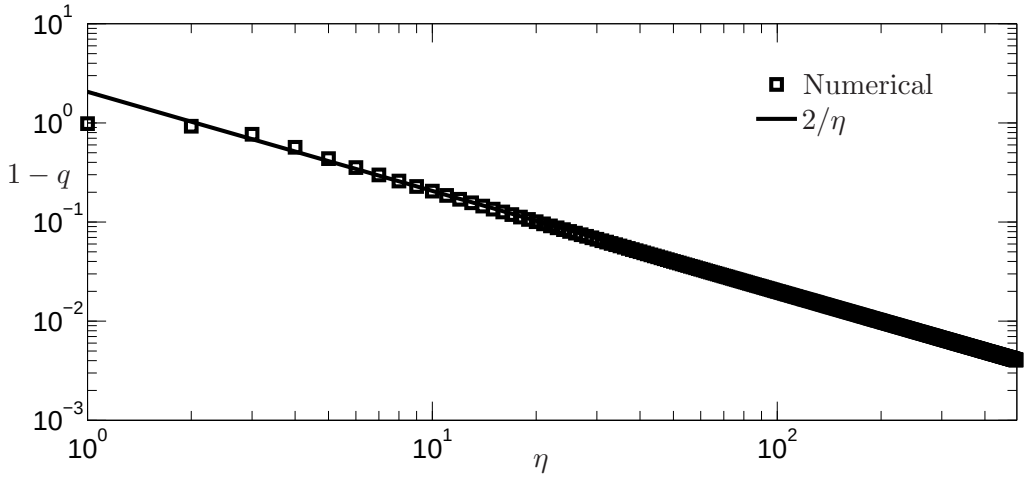

Figure 9.6: *Theoretical prediction and numerical solutions of the characteristic proportion of fluid left behind the wave for large η, plotted on logarithmic scales. The tube is of type $n = 0$ and has stiffness $D = 1$.*

This quadratic equation in a^2 results in two branches,

$$a^2 = \frac{4}{\eta \cos z}\left(-1 \pm \sqrt{1 + \frac{\eta}{2}(1-q)\cos z}\right), \tag{9.18}$$

where $\pm$ is either positive in the lower branch or negative in the upper branch. Only the lower branch corresponds to a real tube radius throughout the domain $0 \leq z \leq 2\pi$. However, the lower branch alone violates the global conservation of fluid volume, (9.12). This must be resolved by switching smoothly from the lower to the upper branch at $z = \pi$. The condition that the lower and upper branches meet at $z = \pi$ requires

$$q = 1 - 2\eta^{-1} + o(\eta^{-2}). \tag{9.19}$$

The theoretical prediction for the flow rate given by (9.19) is in excellent agreement with numerical results, as shown in figure 9.6. Note that the characteristic proportion of fluid left behind the wave is determined solely by the occluded region, independent of the peak region to be examined later. Substituting (9.19) into (9.18) gives the solution for the tube radius in the occluded region,

$$a = \begin{cases} 2\left(1 - \sqrt{2}|\cos z/2|\right)^{-1/2}\eta^{-1/2} + o(\eta^{-1}) & \pi \leq z < 3\pi/2, \\ 2\left(1 + \sqrt{2}|\cos z/2|\right)^{-1/2}\eta^{-1/2} + o(\eta^{-1}) & 0 \leq z < \pi,\ 3\pi/2 < z \leq 2\pi, \end{cases} \tag{9.20}$$

which is continuous at $z = \pi$ but discontinuous at $z = 3\pi/2$. The radius of the tube diverges as $z \to 3\pi/2$ from below and converges to $\sqrt{2/\eta}$ from above. The divergence and discontinuity represent the formation of a shock, which is resolved mathematically by

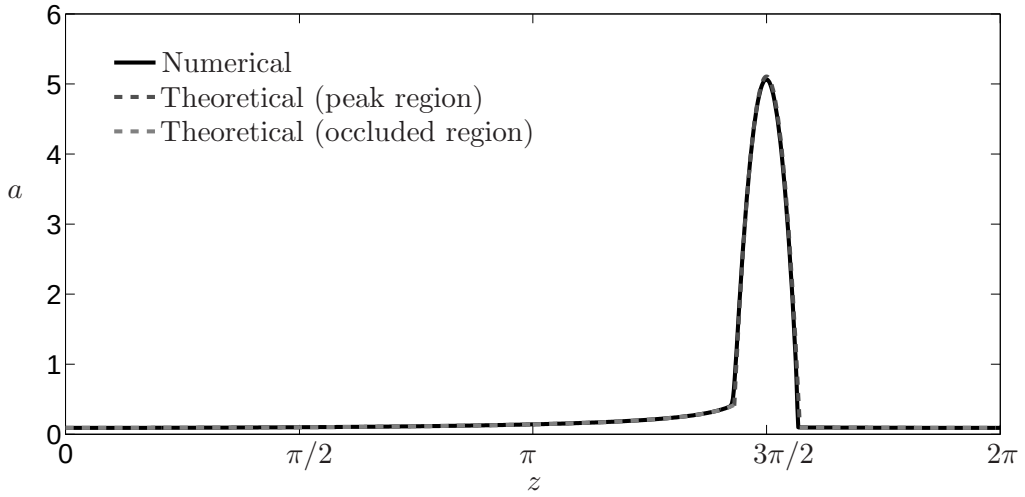

Figure 9.7: *Theoretical and numerical solutions of the tube radius deformed with forcing amplitude* $\eta = 200$. *The theoretical solution, given by (9.21) in the peak region and (9.20) in the occluded region, is in excellent agreement with the numerical solution obtained using input parameters* $n = 0$ *and* $D = 1$.

considering a boundary layer near $z = 3\pi/2$, the peak region.

In the peak region, the tube radius is expected to grow arbitrarily with forcing amplitude η, suggesting that only the first term on the right hand side of (9.13) is dominant. This means that $dp/dz = 0$ so the pressure in the peak region is uniform. It can be shown, by combining equations (9.8) and (9.12), where $\cos z$ in (9.8) is expanded near $z = 3\pi/2$, that the rescaled tube radius is given by $A = \eta^{-1/5}a$ and has a peak A_{max} at $\zeta = 0$, where ζ is the rescaled axial coordinate in the peak region such that $z = 3\pi/2 + \eta^{-2/5}\zeta$. The rescaled equation of (9.8) reduces to $D\,dA/d\zeta + \zeta = 0$ and is integrated to obtain

$$A = A_{max} - \frac{\zeta^2}{2D}. \tag{9.21}$$

The tube radius in the peak region has a parabolic profile, provided that the tube has stiffness $D > 0$. The peak radius of the tube is given by $a_{max} = \eta^{1/5}A_{max}$ with

$$A_{max} = \left(\frac{15^2\pi^2}{2^7 D}\right)^{1/5}, \tag{9.22}$$

which is obtained by solving the rescaled equation of (9.12), $\int_{-\delta}^{\delta} A^2\,d\zeta = 2\pi$, where $\delta = \sqrt{2DA_{max}}$ corresponds to the half-width of the peak region. The occluded region given by (9.20) and the peak region given by (9.21) agree with numerical results, demonstrated in figure 9.7 for a tube of stiffness $D = 1$, forced with amplitude $\eta = 200$. The scaling $\eta^{1/5}$ and the prefactor (9.22) for the peak radius of the tube also agree with numerical results as shown in figure 9.8. The form of a_{max} indicates that the peak radius depends depends

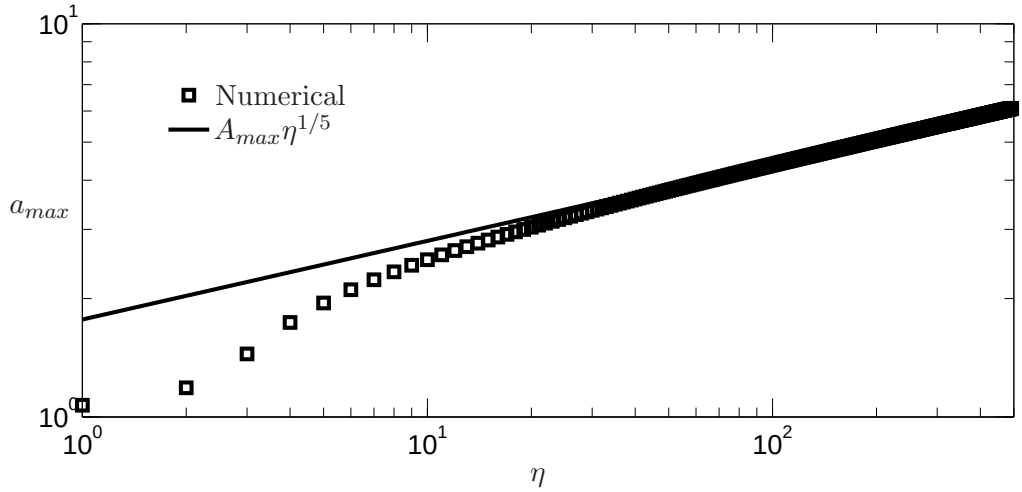

Figure 9.8: *Theoretical prediction and numerical solutions of the peak radius of the tube of type $n = 0$ and stiffness $D = 1$, plotted on logarithmic scales.*

weakly on the tube stiffness and the forcing amplitude for large η.

When the type of tube is characterised by $n = 4$, different scalings of the flow are obtained in both the occluded and peak regions. In the peak region, the pressure is uniform and the rescaled equations are obtained by combining equations (9.8) and (9.12), as before. The rescaled tube radius is given by $A = \eta^{-1/13}a$ and satisfies $D\,d^5A/d\zeta^5+\zeta = 0$, subject to the boundary conditions that A, $dA/d\zeta$, and $d^2A/d\zeta^2$ all vanish near the ends of the peak region, as $\zeta \to \pm\delta$, where $z = 3\pi/2 + \eta^{-2/13}\zeta$. These boundary conditions ensure that the peak region matches smoothly to the occluded region, which is considered later. Integrating the fifth-order differential equation fives times gives the radius of the tube in the peak region,

$$a = \eta^{1/13}\frac{1}{6!D}\left(\delta^2 - \zeta^2\right)^3, \tag{9.23}$$

where

$$\delta = (\pi D^2 6!^2)^{1/13}\left(\frac{11}{3} - \frac{20}{7} - \frac{6}{11} + \frac{1}{13}\right)^{-1/13} \tag{9.24}$$

is obtained using the rescaled integral constraint (9.12), $\int_{-\delta}^{\delta} A^2\,d\zeta = 2\pi$. The peak region agrees with numerics, demonstrated by figure 9.9 for $\eta = 200$, $D = 1$. The maximal radius of the tube at $z = 3\pi/2$, $\eta^{1/13}\delta^6/6!D$, agrees with the numerics as shown in figure 9.10. Note that the forcing amplitude must increase by thirteen orders of magnitude to deform the tube radius by one order of magnitude. A comparison of figures 9.7 and 9.9 indicates that for the same value of D and large η, the peak region of the tube of type $n = 4$ is longer and less deformed than that of the tube of type $n = 0$. The extremely weak dependence of the tube deformation on the applied force in the limit of large η is attributed to large amount of energy that is dissipated due to viscous forces in the highly occluded region,

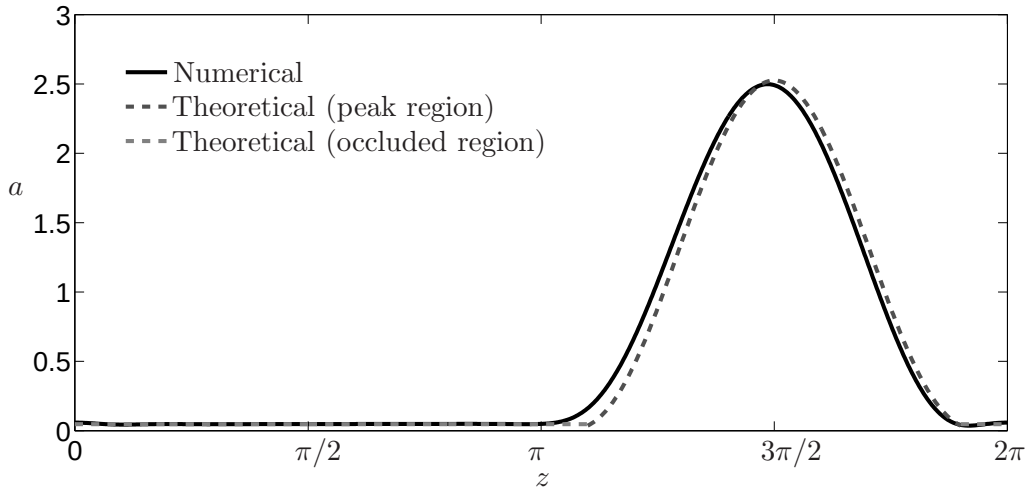

Figure 9.9: *Theoretical and numerical solutions of the tube radius deformed with forcing amplitude* $\eta = 200$*. The theoretical prediction, given by (9.23) in the peak region, agrees with the numerical solution obtained using input parameters* $n = 4$ *and* $D = 1$*.*

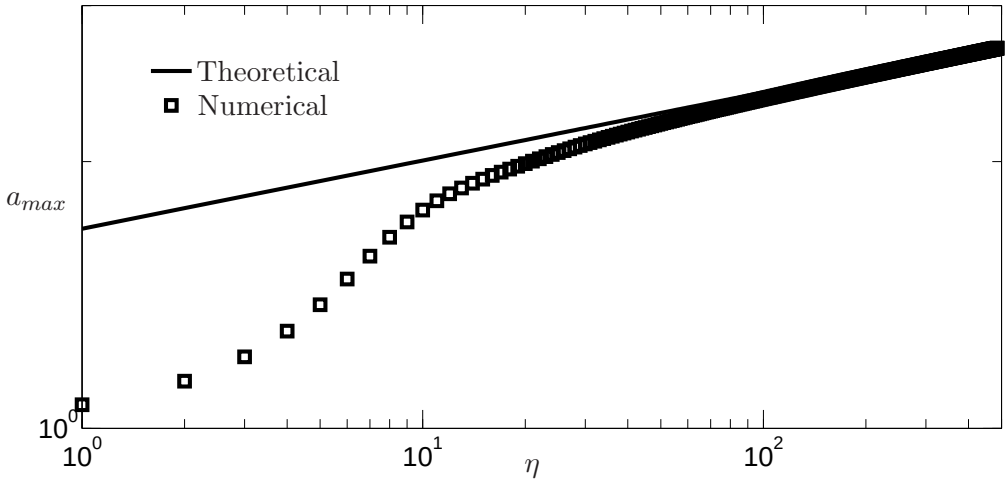

Figure 9.10: *Theoretical prediction and numerical solutions of the peak radius of the tube of type* $n = 4$*, plotted on logarithmic scales.*

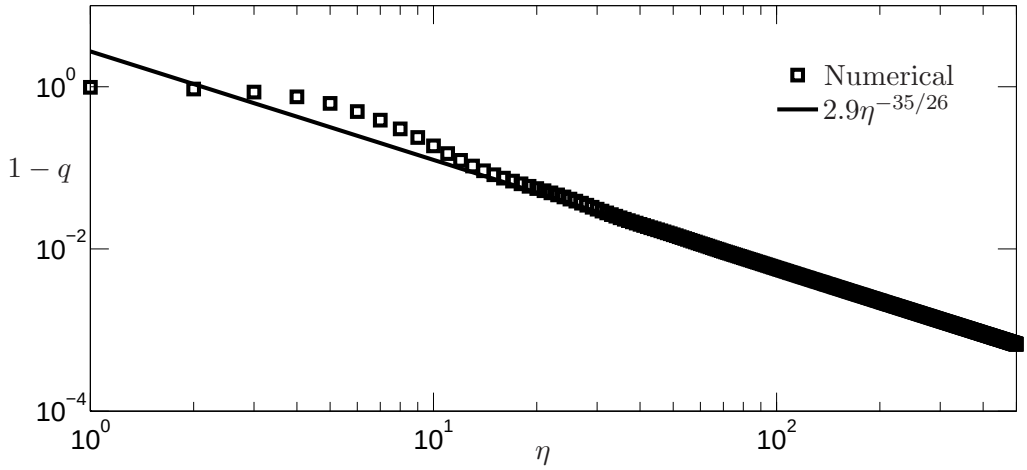

Figure 9.11: *Theoretical prediction and numerical solutions of the characteristic proportion of fluid left behind the wave inside a tube of type $n = 4$, plotted on logarithmic scales.*

instead of doing mechanical work to deflect and expand the peak region of the tube.

In the occluded region away from $z = 3\pi/2$, the numerical solution in figure 9.9 suggests that the tube radius rapidly approaches zero with increasing η. This implies that keeping the dominant terms of (9.13) reduces to $a^2 = 1 - q$. The occluded region has a constant radius. In contrast to the previous problem inside a tube of type $n = 0$, in which q was determined by the occluded region, q in a tube of type $n = 4$ must be obtained by matching the occluded and peak regions using matched asymptotic expansions. It can be shown in the matched region near $z = 3\pi/2 \pm \eta^{-2/13}\delta$ that all terms are dominant in (9.13), except the contribution to dp/dz from $\eta \cos z$, which drops to leading order. A scaling analysis of the reduced equation of (9.13) and its boundary conditions in the matched region indicates that $1 - q = o(\eta^{-35/26})$. The prefactor of this scaling is approximately 2.9 because numerical values of $(1 - q)\eta^{35/26}$ quickly approach this value with increasing η. This theoretical prediction agrees well with numerical results as shown in figure 9.11. Note that the characteristic proportion of fluid left behind the wave approaches 0 more quickly in the limit of $\eta \to \infty$ in a tube of type $n = 4$ than $n = 0$. A tube of type $n = 4$ has a smaller occluded region than a tube of type $n = 0$, implying a trapped core of larger size in the peak region that allows more fluid to propagate with the wave.

It has been determined that a non-zero radial force always results in deformation of a tube of Newtonian fluid. This is no longer the case when the tube contains fluid with a yield stress, where sufficient force on the tube must be applied to induce any motion. The problem of pumping a Bingham plastic, which is a type of non-Newtonian fluid with a yield stress, is considered in the following section. For simplicity, the tube is of type $n = 0$ in the remaining sections.

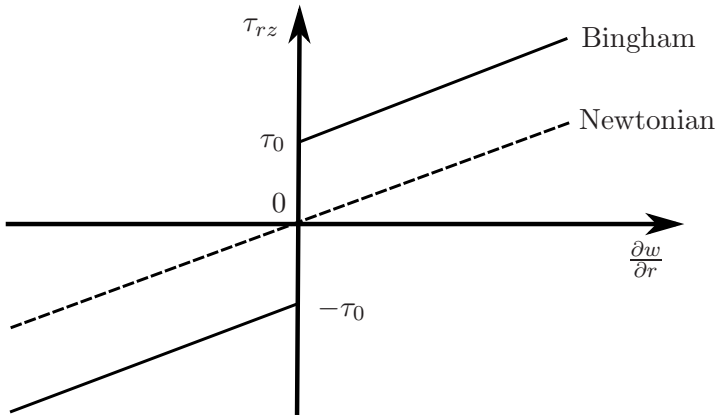

Figure 9.12: *Stress-strain relationships of a Newtonian fluid and a Bingham plastic. The Newtonian curve has a slope corresponding to its viscosity. The Bingham curve has a stress-intercept corresponding to the yield stress and a slope corresponding to the plastic viscosity.*

9.4 Bingham plastic

Consider a Bingham fluid with yield stress τ_0 and plastic viscosity μ. The Bingham fluid behaves either like a Newtonian fluid of viscosity μ in regions where the shear stress exceeds the yield stress, or like a plug without deformation in regions where the shear stress is below the yield stress. The stress-strain relationship of a Bingham fluid is compared with that of a Newtonian fluid in figure 9.12. The introduction of the yield stress modifies the force balance in the axial direction (9.9) to the system of equations

$$\frac{dp}{dz} = \frac{1}{r}\frac{\partial}{\partial r}\left(r\tau_{rz}\right) \tag{9.25}$$

and

$$\frac{\partial w}{\partial r} = \begin{cases} \tau_{rz} - sgn\left(\frac{\partial w}{\partial r}\right) B & |\tau_{rz}| > B, \\ 0 & |\tau_{rz}| < B, \end{cases} \tag{9.26}$$

where

$$B \equiv \frac{\tau_0 R}{\mu c} \tag{9.27}$$

is the dimensionless yield stress, also known as the Bingham number. Equation (9.26) is the one-dimensional approximation of the Bingham constitutive law that applies to the current problem in a slender geometry (Vajravelu *et al.*, 2005). The limit as $B \to 0$ reduces to the Newtonian problem encountered in section 9.3.

The boundary conditions of the axial velocity w are the same as in the Newtonian problem. The solution, satisfying the no-slip condition on the tube wall and regularity at

$r = 0$, is given by

$$w = \begin{cases} -\frac{1}{4}\frac{dp}{dz}[(a^2 - r^2) - 2r_0(a - r)] - 1 & r > r_0 \\ -\frac{1}{4}\frac{dp}{dz}(a - r_0)^2 - 1 & r \leq r_0, \end{cases} \tag{9.28}$$

where

$$r_0 = \min\left[2B/|dp/dz|, a\right] \tag{9.29}$$

is the radius of the plug-like region inside the tube. The velocity profile is either parabolic for $r > r_0$ or uniform for $r \leq r_0$. The central region of the tube, bounded by radius r_0, is actually a pseudo-plug because the associated velocity profile is flat in radius and only appears to be below the yield stress to leading order (Balmforth & Craster, 1999). Indeed, this region is not truly rigid because axial velocity variations remain, except if $r_0 = a$, in which case the fluid spanning that section of the tube becomes truly rigid.

The time-averaged flow rate in the lab frame scaled by π, $q = 1 + 2\int_0^a wr\, dr$, is computed from the axial flow velocity w in the wave frame, as in section 9.3. The expression for q is given by

$$q = -\frac{1}{24}\frac{dp}{dz}(a - r_0)^2\left((a + r_0)^2 + 2a^2\right) - a^2 + 1, \tag{9.30}$$

where dp/dz is given by (9.8) with $n = 0$. The expression on the right hand side of (9.30) without the two final terms represents the steady flow rate in the wave frame and is equivalent to the Buckingham-Reiner equation (Bird *et al.*, 1987). In the limit as $B \to 0$, the flow rate in (9.30) with $r_0 = 0$ reduces to (9.13) and recovers the flow rate of Newtonian fluid, as expected.

The tube radius is determined by solving the governing equations as a boundary-value problem in the domain $0 \leq z \leq 2\pi$. Equation (9.30), subject to the periodic boundary condition $a(0) = a(2\pi)$, contains an eigenvalue q and must be solved subject to the integral constraint (9.12). A sample solution is shown in figure 9.13 and features three qualitatively distinct regions. A sheared region, $r_0 < r < a$, forms near the tube wall where the tube is most deformed. A region of pseudo-plug, $r < r_0 < a$, forms inside the sheared region. A solid region, $r < r_0 = a$, occupies the entire cross-section of the tube where its radius is uniform in z. This means that at any extent along the tube in the lab frame, a stationary region develops during an interval of time, which begins after the departure of a sheared region and ends on arrival of another sheared region.

In the regime of small forcing amplitude η, solutions of the form $a = 1 + \eta a_1 + o(\eta^2)$ and $q = \eta^2 q_2 + o(\eta^3)$ are sought, as in section 9.3. In a tube of type $n = 0$ without stiffness, $D = 0$, it follows from (9.30) that

$$a = 1 - \frac{\eta}{48}\cos z(1 - r_0)^2\left((1 + r_0)^2 + 2a^2\right) + o(\eta^2). \tag{9.31}$$

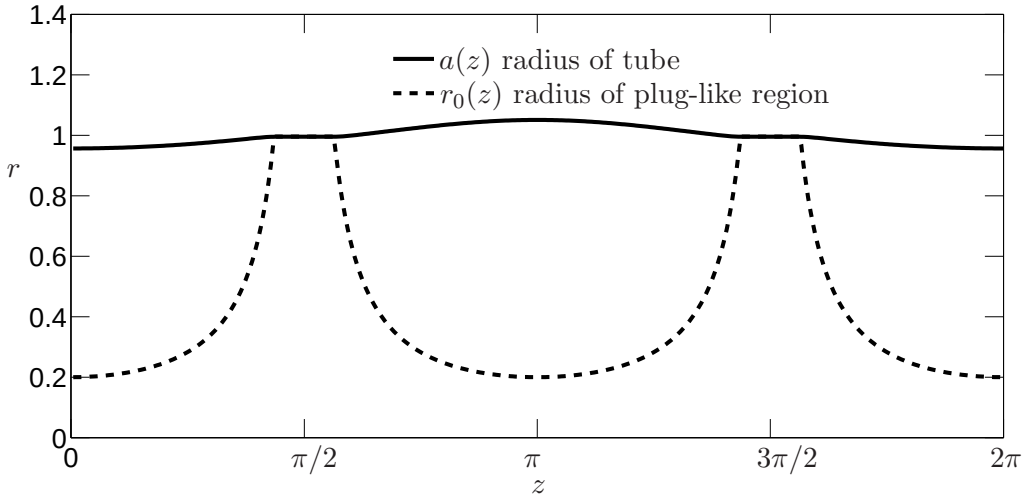

Figure 9.13: *Numerical solution of the tube radius and the plug-like region inside a Bingham fluid. The dashed curve, which translates steadily with the wave, represents the phase boundary between the sheared and plug-like regions. The input parameters are* $n = 0$, $D = 0$, $\eta = 1$, $B = 0.1$.

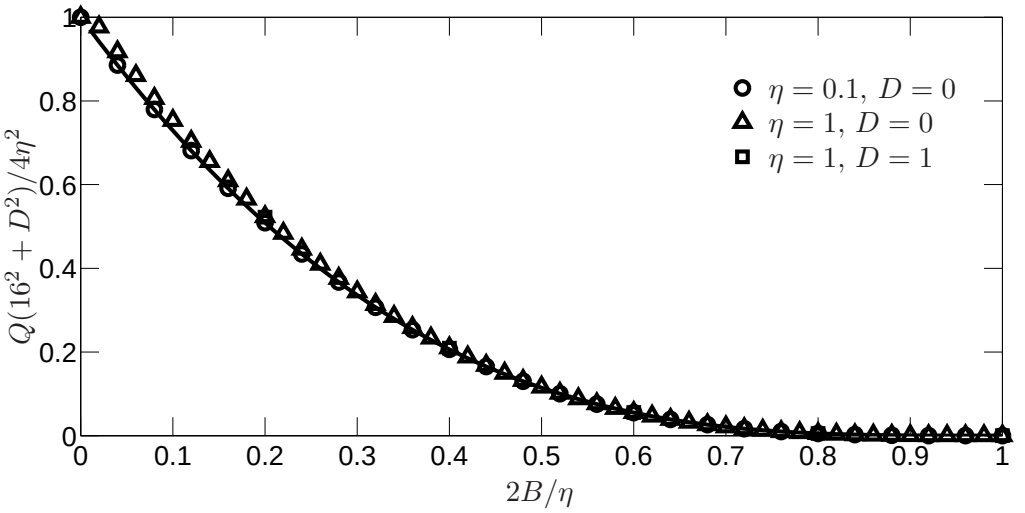

Figure 9.14: *Theoretical prediction for small* η *and numerical solutions of the time-averaged flow rate of Bingham fluid, scaled by the corresponding flow rate of Newtonian fluid. The theoretical prediction is represented by the solid curve. The numerical solutions, represented by different symbols, are obtained by fixing* η *and varying the Bingham number given by (9.27) from 0 to* $\eta/2$.

The time-averaged flow rate q is computed by operating $\langle\cdot\rangle$ on (9.30), the method adopted in section 9.3. It can be shown, after some steps of algebra, that

$$q = \frac{\eta^2}{96}\langle \cos^2 z(1-r_0)^3\left((1+r_0)^2+2\right)\rangle. \tag{9.32}$$

There is no contribution to (9.32) from the solid region, where $r_0 = 1$. The flow rate is determined by the sheared regions, $|z| < \xi$ and $|z-\pi| < \xi$, where $\xi \equiv \cos^{-1}(2B/\eta)$ is the half-width of each region. Substituting $r_0 = 2B/\eta|\cos z|$ into (9.32) and integrating over the sheared regions gives

$$q = \frac{\eta^2}{48\pi} f(\xi), \tag{9.33}$$

where

$$\begin{aligned} f(\xi) &= \frac{3\xi}{2} - \frac{11}{4}\sin(2\xi) + 4\xi\cos^2\xi + \tan\xi\cos^4\xi \\ &\quad - \cos^5\xi\left(\tanh^{-1}(\tan\frac{\xi}{2}) + \frac{1}{4(1-\sin\xi)} - \frac{1}{4(\cos\frac{\xi}{2}+\sin\frac{\xi}{2})^2}\right). \end{aligned} \tag{9.34}$$

Figure 9.14 shows the flow rate given by (9.33), scaled by the corresponding flow rate of Newtonian fluid, (9.16), as a function of the rescaled Bingham number, $2B/\eta$. The theoretical prediction for $D = 0$ and small η is in excellent agreement with numerical results. The rescaled flow rate is a monotonically decreasing function of the rescaled Bingham number for $2B/\eta \leq 1$, as shown in figure 9.14, because the plug-like region increases in size and reduces the flow due to a larger yield stress. In the limit as $2B/\eta \to 1$, the flow rate $q \to 0$ because the forcing amplitude η is insufficient to drive much flow. For $2B/\eta \geq 1$, $q = 0$ because the yield stress is not overcome by the imposed force, resulting in no motion. As the Bingham number approaches 0, the flow rate given by (9.33) approaches the corresponding flow rate of Newtonian fluid, as expected.

In the regime of large forcing amplitude η, solutions are obtained by examining the flow near threshold of no motion, $a = r_0 = 1$, which occurs in the limit as $2B/\eta \to 1$. The small parameter $\epsilon \equiv 1-2B/\eta$ is introduced to examine the limit as $\epsilon \to 0$. Equations (9.29) and (9.30) respectively suggest solutions of the form $r_0 = 1-\epsilon r_1+o(\epsilon^2)$ and $a = 1+\epsilon^2 a_2+o(\epsilon^3)$. The $o(\epsilon)$ correction to the radius of the plug-like region

$$r_1 = \begin{cases} 1-\frac{\zeta^2}{2} & |\zeta| < \sqrt{2},\ |\zeta-\epsilon^{-1/2}\pi| < \sqrt{2}, \\ 0 & \text{otherwise}, \end{cases} \tag{9.35}$$

where $\zeta = \epsilon^{-1/2}z$ is the rescaled axial coordinate, is obtained by expanding $\cos z$ near

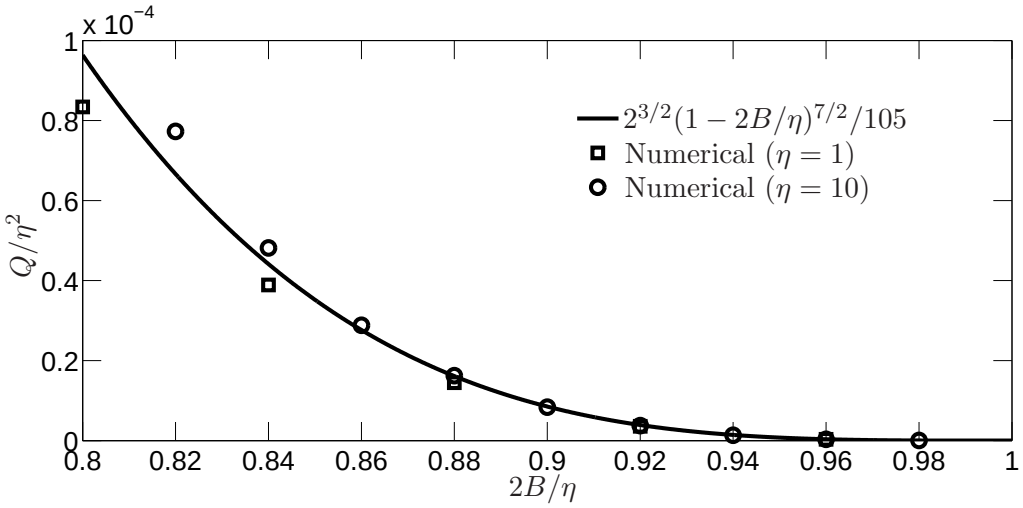

Figure 9.15: *Theoretical prediction in the asymptotic limit as* $2B/\eta \to 1$ *and numerical solutions of the time-averaged flow rate of Bingham fluid.*

$z = 0, \pi$ in (9.29). Substituting r_1 into (9.30) gives

$$a_2 = \pm\frac{\eta r_1^2}{8}, \tag{9.36}$$

where $\pm$ is either $+$ for $|\zeta| < \sqrt{2}$ or $-$ for $|\zeta - \epsilon^{-1/2}\pi| < \sqrt{2}$. Operating $\langle\cdot\rangle$ on (9.30) gives

$$q = \frac{2^{3/2}\eta^2\epsilon^{7/2}}{105}, \tag{9.37}$$

which is in agreement with numerical results as shown in figure 9.15. The flow rate scales like $\epsilon^{7/2}$, indicating that the flow of Bingham plastic increases very weakly with the applied force as it overcomes the yield stress.

It has been determined that the flow rate of both Newtonian fluid and Bingham fluid is a monotonically non-decreasing function of the forcing amplitude. This is no longer the case for the speed of propulsion of a rigid body inside a tube filled with fluid, as investigated in the following section.

9.5 Rigid body

Consider a rigid body of radius b surrounded by a Newtonian fluid of density ρ and dynamic viscosity μ. For simplicity, the rigid body is considered to be an infinitely-long rod of constant radius b so that steady and periodic solutions can be obtained in the wave frame. The rod has steady axial velocity W in the lab frame, as sketched in figure 9.16.

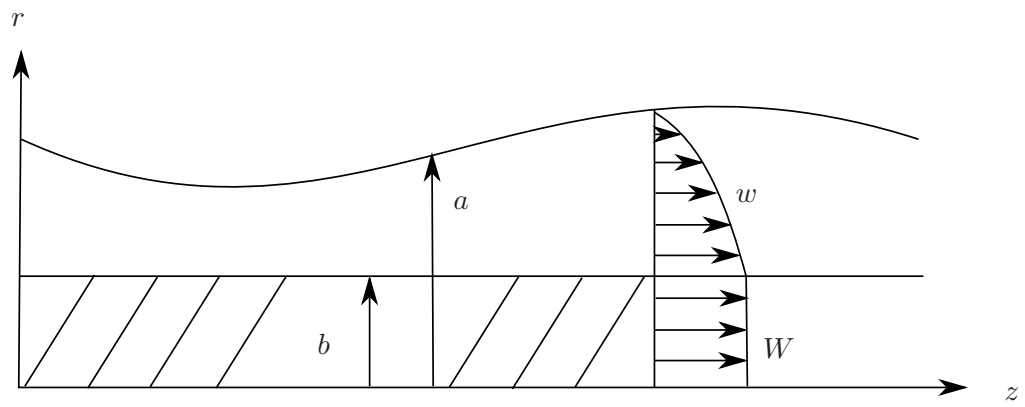

Figure 9.16: *Schematic sketch in cylindrical polar coordinates of an elastic tube filled with Newtonian fluid and a rigid rod. The rod has radius b and propels at a steady axial velocity W in the lab frame.*

The axial velocity profile of the fluid is governed by (9.9), subject to no-slip conditions on the tube wall and the rigid rod. The boundary conditions that $w = 0$ on $r = a$ and $w = W$ on $r = b$ determine the axial velocity in the lab frame,

$$w = -\frac{1}{4}\frac{dp}{dz}(a^2 - r^2) - \left(\frac{W + \frac{1}{4}\frac{dp}{dz}(a^2 - b^2)}{\log\frac{a}{b}}\right)\log\frac{r}{a}. \tag{9.38}$$

In a similar manner to before in sections 9.3 and 9.4, the flow rate in the lab frame is determined and given by

$$q = -\frac{1}{8}\frac{dp}{dz}\left(a^4 - b^4 - \frac{(a^2 - b^2)^2}{\log(\frac{a}{b})}\right) + \frac{W(a^2 - b^2)}{2\log(\frac{a}{b})} - b^2W - a^2 + 1. \tag{9.39}$$

In the limit as $b \to 0$, the flow rate given by (9.39) reduces to the flow rate of Newtonian fluid without any rod given by (9.13), as expected. Note that the boundary-value problem governed by (9.39), with the same periodic boundary condition $a(0) = a(2\pi)$ as before, features W as an eigenvalue to be determined in addition to the eigenvalue q.

The two eigenvalues are determined by imposing two integral constraints, one of which is given by the global conservation of fluid, (9.12). Another integral constraint is obtained from the axial force balance on the rigid rod. Given that the rod is in steady motion, there is no net force exerted on the rod. This is written mathematically as $\langle[r\partial w/\partial r]_{r=b}\rangle = 0$, which reduces to

$$\langle\frac{W + \frac{1}{4}\frac{dp}{dz}(a^2 - b^2)}{\log\frac{a}{b}}\rangle = 0. \tag{9.40}$$

Figure 9.17 shows a set of solutions of tubes containing rigid rods of different size, where the forcing amplitude is fixed at $\eta = 10$. The associated eigenvalues, q and W, are

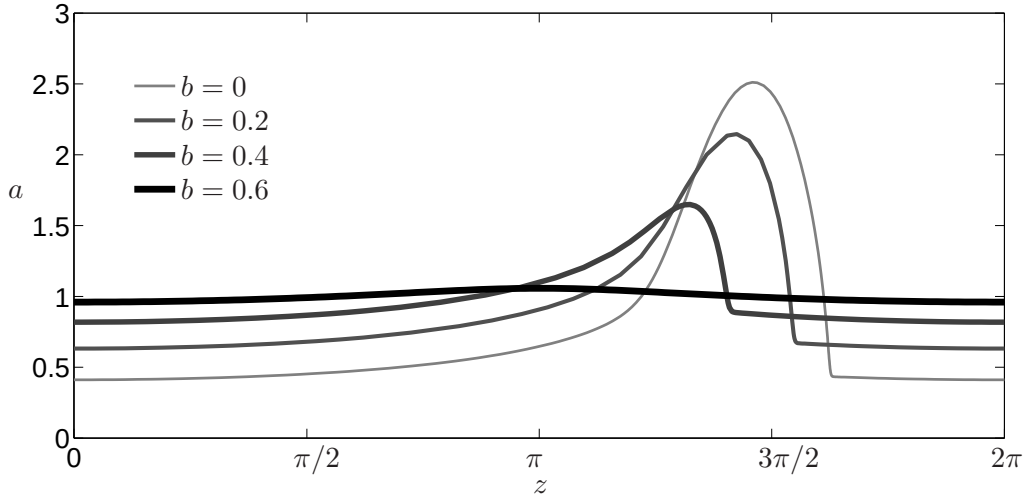

Figure 9.17: *Numerical solutions of the deformed tube containing a rigid rod of different radius b, propelled by a radial force of amplitude $\eta = 10$.*

presented later. The special case of $b = 0$ corresponds to a tube of Newtonian fluid only, which features an occluded region and a peak region, as investigated in section 9.3. The peak radius of the tube decreases with increasing b as shown in figure 9.17, indicating that the presence of the rigid rod reduces the deformation of the tube. The tube is occupied with more solid and less fluid, which partly explains the decreased deformation of the tube with increasing radius of the rigid rod.

The flow rate q increases with η in a qualitatively similar manner, independent of the rod radius b. However, the steady speed of the rod W increases for small η and decreases for large η, as shown in figure 9.18 for three representative values of b. For all values of rod radius, a maximal speed is attained at an intermediate value of η. The maximal attainable speed is less than half the wave speed. The rod speed decreases with η thereafter because the large forcing increases the viscous resistance in the occluded region, making it more difficult for the rod to move relative to the tube. The rod speed generally decreases with increasing b, indicating that it is more difficult to propel a rod of greater size. The quantitative details of the two asymptotic regimes of small and large forcing amplitudes are investigated separately below.

In the regime of small η, solutions of the form $a = 1 + \eta a_1 + o(\eta^2)$, $q = \eta^2 q_2 + o(\eta^3)$, and $W = \eta^2 W_2 + o(\eta^3)$ are sought. Equation (9.39) to order η reduces to $kDda_1/dz + 16a_1 = -k\cos z$, which is integrated subject to the periodic boundary condition $a_1(0) = a_1(2\pi)$ to obtain the solution

$$a = 1 - \eta \frac{16k\cos z + k^2 D \sin z}{(kD)^2 + 16^2} + o(\eta^2), \tag{9.41}$$

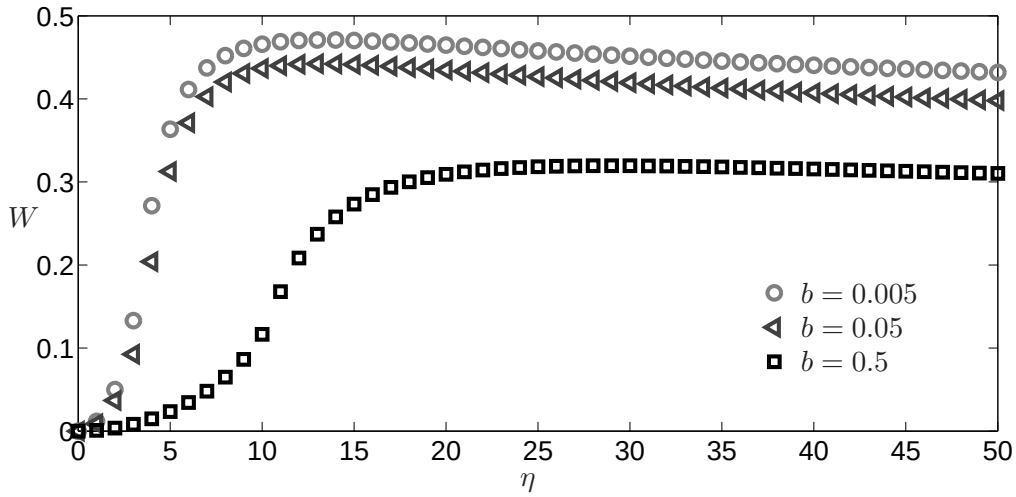

Figure 9.18: *Numerical solutions of the steady velocity of the rigid rod of radius b as a function of the forcing amplitude η.*

where $k = 1 - b^4 + (1 - b^2)^2 / \log b$.

The solution given by (9.41) is substituted into the integral constraint (9.40) to obtain the leading-order speed of the rigid rod,

$$W = \frac{2k}{(kD)^2 + 16^2} \left(2 + \frac{1 - b^2}{\log b} \right) \eta^2 + o(\eta^3). \tag{9.42}$$

Operating $\langle \cdot \rangle$ on (9.39) obtains the leading-order flow rate in the lab frame,

$$q = \frac{2k}{(kD)^2 + 16^2} \left(2 + \frac{1 - b^2}{\log b} \right) (1 - b^2) \eta^2 + o(\eta^3). \tag{9.43}$$

Note that $q \to W$ in the limit as $b \to 0$, indicating that a rigid wire of negligible radius propagates along the centreline of the tube at a steady speed corresponding to the flow rate of the surrounding fluid. The solutions given by (9.42) and (9.43) are in agreement with numerical results, as shown in figure 9.19.

In the regime of large η, the resultant deformation of the tube is qualitatively similar to that of a tube containing Newtonian fluid only, as in section 9.3. A peak region near $z = 3\pi/2$ and an occluded region away from $z = 3\pi/2$ are expected to develop. The two regions are investigated separately below.

In the peak region near $z = 3\pi/2$, the peak radius is determined in a similar manner to before in section 9.3. The conditions in the peak region are that the pressure is uniform and that the total volume must be conserved by (9.12). The peak radius is given by

$$a_{max} = \left(\frac{15^2 \pi^2 (1 - b^2)^2 \eta}{2^7 D} \right)^{1/5}, \tag{9.44}$$

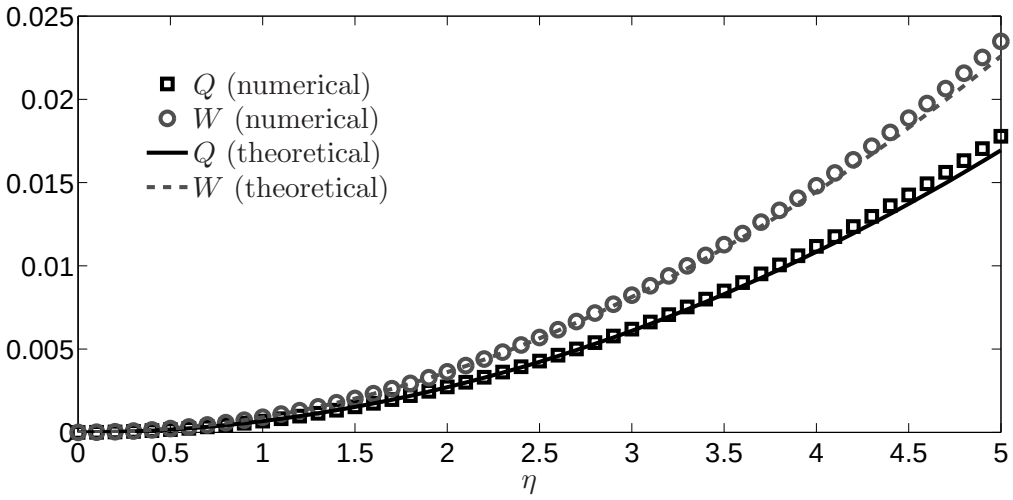

Figure 9.19: *Theoretical predictions in the asymptotic limit of $\eta \to 0$ and numerical solutions of the flow rate q of fluid and the steady speed W of rigid body.*

which scales like $\eta^{1/5}$ with a prefactor that decreases with increasing b, in agreement with numerical results.

In the occluded region, the radius of the tube is expected to approach the radius of the rigid rod. Solutions of the form

$$a = b + \eta^{-1/2}\alpha + o(\eta^{-1}) \tag{9.45}$$

are sought, with the two eigenvalues of the form

$$W = W_\infty + o(\eta^{-1/2}) \tag{9.46}$$

and

$$q = 1 - b^2 - \eta^{-1/2} b\hat{q} + o(\eta^{-1}), \tag{9.47}$$

where α, W_∞ and $\hat{q}$ are all of order 1 to be determined. Note that $1 - b^2 - q$ is a measure of the proportion of fluid left behind the wave, which is expected to scale like $(a - b)b$ and diminish in the limit as $\eta \to \infty$. This is because most of the fluid is trapped in a recirculating core of the peak region and propagates with the wave, while the remaining fluid lies in a thin shell of radius b and thickness $a - b$, the gap between the tube and the rod. The choice of the scaling $\eta^{-1/2}$ for corrections to a, q and W is justified below. A cubic equation for α,

$$\cos z\, \alpha^3 + 6(2 - W_\infty)\alpha - 6\hat{q} = 0, \tag{9.48}$$

is obtained by substituting (9.45), (9.46), and (9.47) into (9.39), and neglecting terms of order η^{-1}. All three terms in the cubic equation must be of order 1 by demanding that

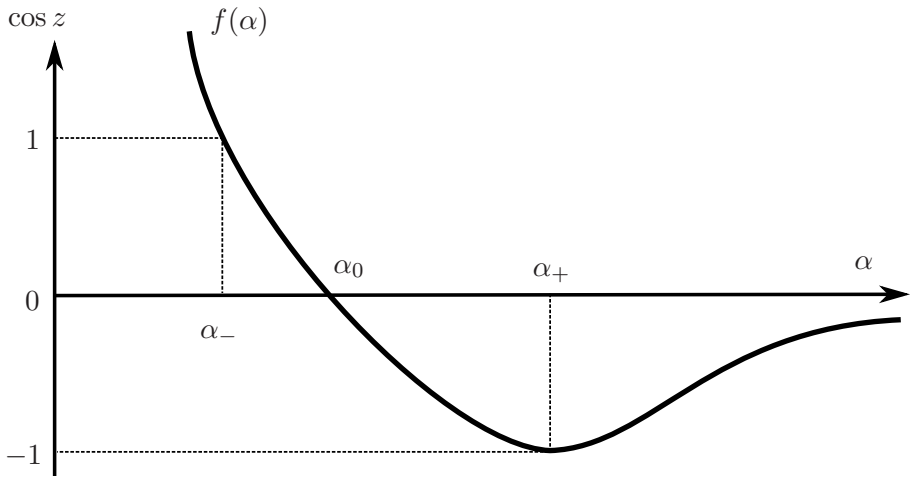

Figure 9.20: *Sketch of $f(\alpha)$ given by (9.49), which changes sign at α_0 and attains its minimum of -1 at α_+. The value α_- corresponds to the minimal radius of the tube in the occluded region.*

$a \to b + o(\eta^{-1/2})$, $q \to 1 - b^2 + o(\eta^{-1/2})$ and $W \to W_\infty + o(\eta^{-1/2})$, which justifies the earlier choice of the scaling $\eta^{-1/2}$. The solution for α is determined implicitly by a rearrangement of (9.48),

$$\cos z = f(\alpha) \equiv \frac{6}{\alpha^3}\left(\hat{q} - \alpha\,(2 - W_\infty)\right). \tag{9.49}$$

The function f has a local minimum at $\alpha_+ = 3\hat{q}/(4 - 2W_\infty)$ with the asymptotic limits that $f \to \infty$ as $\alpha \to 0$ and $f \to 0$ as $\alpha \to \infty$, as sketched in figure 9.20. Given that the tube radius must match smoothly with the peak region as $z \to 3\pi/2$, f must attain a local minimum of -1. The equation $f(\alpha_+) = -1$ reduces to

$$\hat{q} = \frac{2^{3/2}}{3}\,(2 - W_\infty)^{3/2}, \tag{9.50}$$

which provides an equation for the two unknown quantities, W_∞ and $\hat{q}$. A minimal tube radius is attained at $z = 0$, where $\alpha = \alpha_-$ satisfies the cubic equation $f(\alpha_-) = 1$. The function f changes sign at $\alpha_0 = 2\alpha_+/3$.

In addition to equation (9.50), another equation relating W_∞ and $\hat{q}$ can be obtained by (9.40). Note that contributions to the integral (9.40) from the occluded region are dominant because they are negligible from the peak region, where $a \sim \eta^{1/5}$ as $z \to 3\pi/2$. By substituting (9.45) into (9.40) and keeping only the leading-order terms of order $\eta^{1/2}$, we obtain

$$\langle \frac{2W_\infty}{\alpha} + \alpha \cos z \rangle = 0. \tag{9.51}$$

This integral constraint indicates that the tangential-stress balance is between the stress due to the rod speed and the radial forcing in the occluded region. The tangential stress on the rod is independent of the peak region or the stiffness D of the tube. Furthermore, the

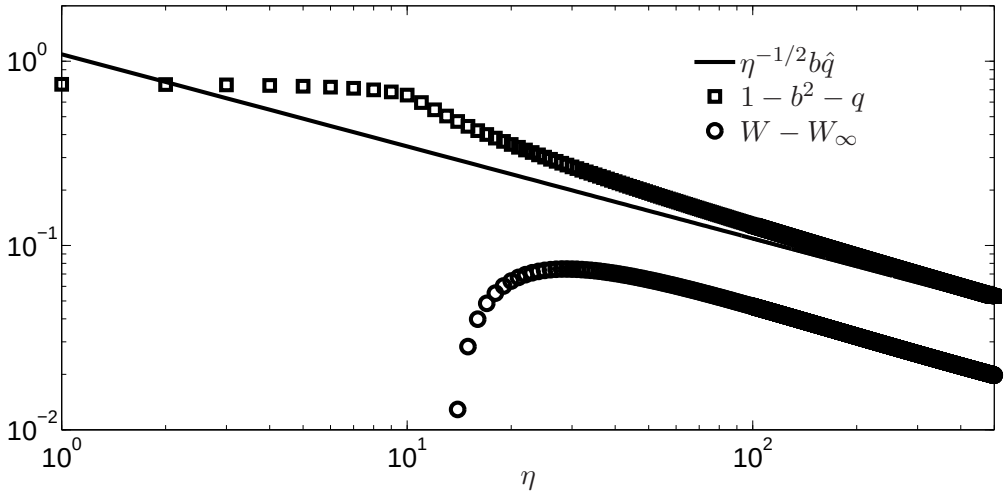

Figure 9.21: *The proportion of fluid left by the wave $1-b^2-q$ and the approach of the rod speed W to $W_\infty \approx 0.247$ for large forcing amplitudes η, plotted on logarithmic scales. The radius of the rod $b = 0.5$ is fixed. Theoretical prediction for the proportion of fluid left by the wave, $\eta^{-1/2}b\hat{q}$, with $\hat{q} \approx 2.19$, agrees with numerical results. The slope of $W - W_\infty$ indicates that W approaches W_∞ like $\eta^{-1/2}$.*

governing equations for W_∞ and $\hat{q}$, (9.50) and (9.51), are independent of b. This indicates that in the regime of large forcing amplitudes, the size of the rod does not influence its speed of propulsion to leading order. The integral constraint (9.51) reduces to

$$(4W_\infty - 6)\langle\alpha^{-1}\rangle + (4 - 2W_\infty)^{3/2}\langle\alpha^{-2}\rangle = 0, \tag{9.52}$$

by substituting (9.49) and (9.50) into (9.51). The integral $\langle\cdot\rangle$ in z-space can be evaluated in α-space by using (9.49), treating the three regions of $0 \le z \le \pi$, $\pi < z < 3\pi/2$ and $3\pi/2 < z < 2\pi$ separately. This gives

$$\langle\cdot\rangle = \int_{\alpha_+}^{\infty} \cdot J\, d\alpha - \int_{\alpha_-}^{\alpha_0} \cdot J\, d\alpha - \int_{\alpha_-}^{\alpha_+} \cdot J\, d\alpha, \tag{9.53}$$

where

$$J = \frac{df/d\alpha}{2\pi\sqrt{1-f^2}}. \tag{9.54}$$

Solving equation (9.52), where $\langle\alpha^{-1}\rangle$ and $\langle\alpha^{-2}\rangle$ are evaluated numerically using (9.53), gives $W_\infty \approx 0.247$. It follows that $\hat{q} \approx 2.19$ by (9.50) and completes the theoretical analysis of the problem.

A measure of the proportion of fluid left behind the wave is plotted as a function of the forcing amplitude in figure 9.21. Numerical values approach slowly to the theoretical prediction with increasing forcing amplitude. The difference between the rod speed from $W_\infty \approx 0.247$, also shown in figure 9.21, approaches 0 like $\eta^{-1/2}$, which is consistent with

(9.46). In the regime of large forcing amplitude, most of the fluid is carried with the wave while the rod propels at approximately a quarter of the wave speed in the tube.

9.6 Conclusion

A theoretical analysis of fluid driven along a deformable tube by a prescribed radial force provides important insight into peristaltic motion. For small forcing amplitudes η, the deformation of the tube is of order η and the time-averaged flow rate is of order η^2, independent of the three different types of fluid considered in the tube. For large forcing amplitudes η, different results are obtained depending on the contents of the tube, as summarised separately below.

A tube of Newtonian fluid features an occluded region and a peak region, where a trapped core of fluid recirculates in the wave frame. The peak region, which is shorter and more deformed in a linearly elastic tube with a spring constant D than a thin shell of constant bending stiffness D, depends weakly on the forcing amplitude. A larger forcing amplitude increases the size of the trapped core in the peak region, allowing more fluid to propagate with the wave.

A tube of Bingham plastic features a sheared region, a pseudo-plug region, and a solid region in the wave frame, provided that the applied force has overcome the yield stress. The existence of the three distinct regions reduces the flow rate of the Bingham plastic considerably compared to that of a Newtonian fluid, which is sheared everywhere. The flow rate of the Bingham plastic increases from 0 extremely slowly with the forcing amplitude as the yield stress is overcome.

The steady propulsion of a rigid rod surrounded by Newtonian fluid in a tube shows that the size of the rod plays an important role. As the radius of the rod increases, the tube deforms less with a smaller speed of propulsion of the rod. The maximal speed of the rod, which is less than half the wave speed, is attained at a moderate forcing amplitude. A larger body, which reduces the maximal attainable speed of propulsion, is a bitter pill to swallow for the hungry python.

The propulsion of a rigid body in a deformable tube could be pursued further by modifying the underlying assumptions of the problem. The theoretical analysis presented here is limited to describing steady and periodic solutions in the wave frame. Time-dependent solutions in a non-periodic domain could be investigated, for example, by prescribing a radial force with a solitary-wave profile to drive a rigid body of finite length. This may provide further insight into the motion of the rigid body, where the regions ahead and behind the body in the tube are respectively relaxed and contracted.

Chapter 10

Conclusion

10.1 Summary

The flow of materials is considered in a series of different situations relevant to processes in geophysics, engineering and biology. A common feature in all the situations is that the flowing structure is long and thin. In order to study effects of the topography, the volume and the rheology of the flowing structure, the moving boundaries of the flow are predicted by solving a class of free-boundary problems in mathematical models. General results are obtained and have broad implications as outlined below.

Chapters 2 and 3 are concerned with predicting the advance of lava flows supplied at unsteady rates down a slope. The initial advance of long lava flows depends importantly on the effusion rate, which controls the cumulative volume of the lava emplaced on volcanoes. The results indicate that the advancing front depends importantly on the volume of the flowing material and weakly on the topography. A major strength of the theoretical approaches lies in their general applicability to predict the advance of a diverse range of geophysical flows, including ice streams and debris flows.

Chapters 4, 5 and 6 investigate the slumping of a constant volume of viscous fluid on rigid surfaces with different shapes, motivated by the engineering of industrial processes involving thin films. The importance of the fluid volume is reinforced by the result that the volume sets the length scale of the flow features. For example, the leading edge of fluid spreading on a sphere splits into a series of rivulets after extending a critical length, which depends primarily on the fluid volume. Another example is that the leading front of viscous flow in a channel of slowly increasing width detaches from the walls after extending a critical distance, which depends importantly on the fluid volume. In contrast, the viscosity of the fluid has no effect on the length scale and only changes the time scale of the flow.

Chapters 7 and 8 examine the flow of granular materials, which can produce levees and avalanches down a rough inclined plane. These phenomena do not arise in Newtonian flows, indicating that changing the rheology of the flowing structure introduces new flow features. Distinct results are obtained in the laboratory using sand and glass beads, meaning that shallow granular flows depend on the shape of grains constituting the flowing material.

Chapter 9 studies the peristaltic pumping of different materials in a linearly elastic tube. Newtonian fluids, Bingham plastics and rigid bodies are considered separately in the tube. The deformation of the tube and the motion of the inner contents are different in each case, reinforcing the idea that the rheology of the material plays an important role.

10.2 Future work

The series of problems considered here should provide a foundation for studying further problems in the future. The simplified models can be extended to incorporate additional effects in more complicated situations, which may better represent realistic scenarios in geophysical, engineering and biological applications. Effects include the cohesive properties of snow in the flow of avalanches and nonlinear elasticity of biological ducts undergoing peristalsis.

Testing the models against analog experiments in the laboratory offers insight into the strengths and limitations of the models. The limitations highlight the areas where further work is needed, offering future research opportunities. In the long term, new methods which are different from the simplified approach adopted here may help us better understand some remaining issues, including the mechanics of contact lines and granular materials.

A recurring and important aspect of the spreading of viscous fluids which remains to be completely understood is the mechanics of moving contact lines. Effects due to contact

lines, which are neglected in the simplified models developed here, may play an important role in viscous flow along corners of a tipped container. The contact line should also influence the motion of rivulets which develop after the fingering instability of thin films flowing on slopes. The physics at the molecular level near the contact line may influence the macroscopic behaviour of thin liquid films.

The physics at the scale of individual grains may influence the macroscopic flow of granular materials. Different features of the flow arise depending on the shape of the grains, which are different for sand and glass beads. Incorporating the physics at the level of individual grains may provide insight into the macroscopic behaviour of granular flows and how the flows can stop.

Acknowledgements

I have been fortunate to have the opportunity to pursue my interests in a stimulating environment with influential and inspirational people.

My supervisors, Herbert Huppert and Jim McElwaine, introduced me to the power of combining mathematics and simple experiments to study the dynamics of viscous fluids and granular materials. Herbert, who lectured so entertainingly on fluid dynamics when I was an undergraduate, inspired me to pursue compelling projects on viscous flows. Jim showed me with great enthusiasm and imagination how challenging issues arise in granular flows. As scientists with profound insight and individuals with great character, both my supervisors have set excellent examples for me. I am extremely grateful to them for offering their support, encouragement and guidance throughout the period of my doctoral training.

I have benefited from spending part of the period with people outside Cambridge. Neil Balmforth supervised my project on peristaltic waves at the Woods Hole Oceanographic Institution during the summer of 2009. In the summer of 2008, Steve Sparks and his colleagues introduced me to many intriguing aspects of volcanism during a field trip to the Isle of Rum in Scotland.

It has been a fruitful experience to be part of an academic community in Cambridge. I have engaged regularly in discussions with all members of the Institute of Theoretical Geophysics, including Grae Worster, Jerome Neufeld, John Lister and Roiy Sayag. John Hinch, John Lister and Stuart Dalziel offered constructive comments on early stages of my work. My examiners, Grae Worster and Andrew Hogg, provided additional comments for improvement.

I have been privileged to work with friendly and helpful people in the laboratory. David Page-Croft, John Milton, Mark Hallworth, Neil Price and Trevor Parkin provided technical

support for my experiments. Alex Holyoake and Stuart Dalziel helped me process some experimental data.

A Gates Cambridge Scholarship provided full financial support for my graduate study and research. The Gates Cambridge Trust, King's College and the Department of Applied Mathematics and Theoretical Physics provided generous funds for attending numerous conferences.

I am thankful for the moral support of my family and friends who made my time in Cambridge so enjoyable and enriching.

Bibliography

Abate, A. R., Katsuragi, H. & Durian, D. J. 2007 Avalanche statistics and time-resolved grain dynamics for a driven heap. *Phys. Rev. E* **76**, 61301.

Acheson, D. J. 1990 *Elementary fluid dynamics*. Oxford University Press.

Ancey, C., Cochard, S. & Andreini, N. 2009 The dam-break problem for viscous fluids in the high-capillary-number limit. *J. Fluid Mech.* **624**, 1–22.

Aranson, I. S. & Tsimring, L. S. 2001 Continuum description of avalanches in granular media. *Phys. Rev. E* **64**, 020301.

Aranson, I. S., Tsimring, L. S., Malloggi, F. & Clément, E. 2008 Nonlocal rheological properties of granular flows near a jamming limit. *Phys. Rev. E* **78**, 031303.

Argentina, M., Skotheim, J. & Mahadevan, L. 2007 Settling and swimming of flexible fluid-lubricated foils. *Phys. Rev. Lett.* **99**, 224503.

Azanza, E., Chevoir, F. & Moucheront, P. 1999 Experimental study of collisional granular flows down an inclined plane. *J. Fluid Mech.* **400**, 199–227.

Babchin, A. J., Frenkel, A. L., Levich, B. G. & Sivashinsky, G. I. 1983 Nonlinear saturation of Rayleigh–Taylor instability in thin films. *Phys. Fluids* **26**, 3159–3161.

Balmforth, N. J., Coombs, D. & Pachmann, S. 2010 Microelastohydrodynamics of swimming organisms near solid boundaries in complex fluids. *Q. J. Mech. Appl. Math.* **63**, 267–294.

Balmforth, N. J. & Craster, R. V. 1999 A consistent thin-layer theory for Bingham plastics. *J. Non-Newtonian Fluid Mech.* **84**, 65–81.

Balmforth, N. J., Craster, R. V. & Sassi, R. 2002 Shallow viscoplastic flow on an inclined plane. *J. Fluid Mech.* **470**, 1–29.

Baloga, S. & Pieri, D. 1986 Time-dependent profiles of lava flows. *J. Geophys. Res.* **91**, 9543–9552.

Batchelor, G. K. 2000 *An Introduction to Fluid Dynamics*. Cambridge University Press.

Batchelor, G. K., Moffatt, H. K. & Worster, M. G. 2000 *Perspectives in Fluid Dynamics: A Collective Introduction to Current Research*. Cambridge University Press.

Bertozzi, A. L. & Brenner, M. P. 1997 Linear stability and transient growth in driven contact lines. *Phys. Fluids* **9**, 530–539.

Bertuzzi, A., Salinari, S., Mancinelli, R. & Pescatori, M. 1983 Peristaltic transport of a solid bolus. *J. Biomechanics* **16**, 459.

Bird, R. B., Armstrong, R. C. & Hassager, O. 1987 *Dynamics of polymeric liquids, Vol. 1, Fluid mechanics*. John Wiley& Sons, New York.

Blong, R. J. 1984 *Volcanic hazards. A sourcebook on the effects of eruptions*. Academic Press Australia, North Ryde.

Börzsönyi, T. & Ecke, R. E. 2007 Flow rule of dense granular flows down a rough incline. *Phys. Rev. E* **76**, 031301.

Börzsönyi, T., Halsey, T. C. & Ecke, R. E. 2005 Two scenarios for avalanche dynamics in inclined granular layers. *Phys. Rev. Lett.* **94**, 208001.

Börzsönyi, T., Halsey, T. C. & Ecke, R. E. 2008 Avalanche dynamics on a rough inclined plane. *Phys. Rev. E* **78**, 011306.

Brasseur, J. G., Corrsin, S. & Lu, N. Q. 1987 Influence of a peripheral layer of different viscosity on peristaltic pumping with Newtonian fluids. *J. Fluid Mech.* **174**, 495–519.

Bretherton, F. P. 1961 The motion of long bubbles in tubes. *J. Fluid Mech.* **10**, 166–188.

Bruno, B. C., Baloga, S. M. & Taylor, G. J. 1996 Modeling gravity-driven flows on an inclined plane. *J. Geophys. Res.* **101**, 11565–11578.

Calvari, S. & Pinkerton, H. 1999 Lava tube morphology on Etna and evidence for lava flow emplacement mechanisms. *J. Volcanol. Geotherm. Res.* **90**, 263–280.

Carew, E. O. & Pedley, T. J. 1997 An active membrane model for peristaltic pumping: part I – Periodic activation waves in an infinite tube. *J. Biomech. Eng.* **119**, 66–76.

Cazabat, A. M., Heslot, F., Troian, S. M. & Carles, P. 1990 Fingering instability of thin spreading films driven by temperature gradients. *Nature* **346**, 824–826.

Coltelli, M., Proietti, C., Branca, S., Marsella, M., Andronico, D. & Lodato, L. 2007 Analysis of the 2001 lava flow eruption of Mt. Etna from three-dimensional mapping. *J. Geophys. Res.* **112**, F02029.

Coussot, P., Proust, S. & Ancey, C. 1996 Rheological interpretation of deposits of yield stress fluids. *J. Non-Newtonian Fluid Mech.* **66**, 55–70.

Cui, X., Gray, J. & Jóhannesson, T. 2007 Deflecting dams and the formation of oblique shocks in snow avalanches at Flateyri, Iceland. *J. Geophys. Res.* **112**, F04012.

Daerr, A. 2001 Dynamical equilibrium of avalanches on a rough plane. *Phys. Fluids* **13**, 2115–2124.

Dalziel, S. B. 2003 DigiFlow User Guide. *DigiFlow, DL Research Partners, version 0.7* .

Davies, T. R. & Mcsaveney, M. J. 1999 Runout of dry granular avalanches. *Can. Geotech. J.* **36**, 313–320.

Davies, T. R. H. 1986 Large debris flows: a macro-viscous phenomenon. *Acta Mechanica* **63**, 161–178.

Davis, S. H. 1983 Contact-line problems in fluid mechanics. *J. Appl. Mech.* **50**, 977–982.

Deboeuf, S., Lajeunesse, E., Dauchot, O. & Andreotti, B. 2006 Flow rule, self-channelization, and levees in unconfined granular flows. *Phys. Rev. Lett.* **97**, 158303.

Duffy, B. R. & Moffatt, H. K. 1995 Flow of a viscous trickle on a slowly varying incline. *Chem. Eng. J.* **60**, 141–146.

Dussan, E. B. 1979 On the spreading of liquids on solid surfaces: static and dynamic contact lines. *Annu. Rev. Fluid Mech.* **11**, 371–400.

Félix, G. & Thomas, N. 2004 Relation between dry granular flow regimes and morphology of deposits: formation of levées in pyroclastic deposits. *Earth Planet. Sci. Lett.* **221**, 197–213.

Forterre, Y. & Pouliquen, O. 2003 Long-surface-wave instability in dense granular flows. *J. Fluid Mech.* **486**, 21–50.

Forterre, Y. & Pouliquen, O. 2008 Flows of Dense Granular Media. *Annu. Rev. Fluid Mech.* **40**, 1–24.

Fraysse, N. & Homsy, G. M. 1994 An experimental study of rivulet instabilities in centrifugal spin coating of viscous Newtonian and non-Newtonian fluids. *Phys. Fluids* **6**, 1491.

Frigaard, I. A. & Ryan, D. P. 2004 Flow of a visco-plastic fluid in a channel of slowly varying width. *J. Non-Newtonian Fluid Mech.* **123**, 67–83.

GDRMiDi 2004 On dense granular flows. *Eur. Phys. J. E* **14**, 341–365.

Goldhirsch, I. 2003 Rapid Granular Flows. *Annu. Rev. Fluid Mech.* **35**, 267–293.

Goodwin, R. & Homsy, G. M. 1991 Viscous flow down a slope in the vicinity of a contact line. *Phys. Fluids* **3**, 515–528.

Gray, J., Wieland, M. & Hutter, K. 1999 Gravity-driven free surface flow of granular avalanches over complex basal topography. *Proc. R. Soc. A* **455**, 1841–1874.

Greeley, R. & Hyde, J. H. 1972 Lava tubes of the Cave Basalt, Mount St. Helens, Washington. *Geol. Soc. Amer. Bull.* **83**, 2397–2418.

Griffiths, R. W. 2000 The dynamics of lava flows. *Annu. Rev. Fluid Mech.* **32**, 477–518.

Griffiths, R. W. & Fink, J. H. 1993 Effects of surface cooling on the spreading of lava flows and domes. *J. Fluid Mech.* **252**, 667–702.

Guest, J. E., Kilburn, C. R. J., Pinkerton, H. & Duncan, A. M. 1987 The evolution of lava flow-fields: observations of the 1981 and 1983 eruptions of Mount Etna, Sicily. *Bull. Volcanol.* **49**, 527–540.

Hákonardóttir, K. M., Hogg, A. J., Batey, J. & Woods, A. W. 2003 Flying avalanches. *Geophys. Res. Lett.* **30**, 2191.

Hallworth, M. A., Huppert, H. E. & Sparks, R. S. J. 1987 A laboratory simulation of basaltic lava flows. *Modern Geol.* **11**, 93–107.

Harris, A. J. L. & Rowland, S. K. 2009 Effusion rate controls on lava flow length and the role of heat loss: a review. *Studies in Volcanology: The Legacy of George P. L. Walker* pp. 33–51.

Hopfinger, E. J. 1983 Snow Avalanche Motion and Related Phenomena. *Annu. Rev. Fluid Mech.* **15**, 47–76.

Hulme, G. 1974 The interpretation of lava flow morphology. *Geophys. J. Int.* **39**, 361–383.

Huppert, H. E. 1982a The propagation of two-dimensional and axisymmetric viscous gravity currents over a rigid horizontal surface. *J. Fluid Mech.* **121**, 43–58.

Huppert, H. E. 1982b Flow and instability of viscous current down a slope. *Nature* **300**, 427–429.

Indeikina, A., Veretennikov, I. & Chang, H. C. 1997 Drop fall-off from pendent rivulets. *J. Fluid Mech.* **338**, 173–201.

Jeffreys, H. 1925 The flow of water in an inclined channel of rectangular section. *Phil. Mag.* **49**, 793–807.

Jeffreys, H. 1930 The drainage of a vertical plate. *Math. Proc. Camb. Phil. Soc.* **26**, 204–205.

Jenkins, J. T. 2006 Dense shearing flows of inelastic disks. *Phys. Fluids* **18**, 103307.

Jop, P., Forterre, Y. & Pouliquen, O. 2006 A constitutive law for dense granular flows. *Nature* **441**, 727–730.

Kerr, R. C., Griffiths, R. W. & Cashman, K. V. 2006 Formation of channelized lava flows on an unconfined slope. *J. Geophys. Res.* **111**, B10206.

Keszthelyi, L. 1995 A preliminary thermal budget for lava tubes on the Earth and planets. *J. Geophys. Res.* **100**, 20411–20420.

Lajeunesse, E., Mangeney-Castelnau, A. & Vilotte, J. P. 2004 Spreading of a granular mass on a horizontal plane. *Phys. Fluids* **16**, 2371–2381.

Lemieux, P. A. & Durian, D. J. 2000 From avalanches to fluid flow: a continuous picture of grain dynamics down a heap. *Phys. Rev. Lett.* **85**, 4273–4276.

Lighthill, M. J. & Whitham, G. B. 1955*a* On Kinematic Waves. I. Flood Movement in Long Rivers. *Proc. Roy. Soc. A* **229**, 281–316.

Lighthill, M. J. & Whitham, G. B. 1955*b* On Kinematic Waves. II. A Theory of Traffic Flow on Long Crowded Roads. *Proc. Roy. Soc. A* **229**, 317–345.

Lipman, P. W. & Banks, N. G. 1987 Aa flow dynamics, Mauna Loa 1984. *U.S. Geol. Surv. Prof. Pap.* **1350**, 1527–1567.

Lister, J. R. 1992 Viscous flows down an inclined plane from point and line sources. *J. Fluid Mech.* **242**, 631–653.

Llewellin, E. W., Mader, H. M. & Wilson, S. D. R. 2002 The rheology of a bubbly liquid. *Proc. Roy. Soc. A* **458**, 987–1016.

Love, A. E. H. 1944 *A treatise on the mathematical theory of elasticity*. Dover Publications.

Lube, G., Huppert, H. E., Sparks, R. S. J. & Hallworth, M. A. 2004 Axisymmetric collapses of granular columns. *J. Fluid Mech.* **508**, 175–199.

Lykoudis, P. S. & Roos, R. 1970 The fluid mechanics of the ureter from a lubrication theory point of view. *J. Fluid Mech.* **43**, 661–674.

Malin, M. C. 1980 The lengths of Hawaiian lava flows. *Geology* **8**, 306–308.

Malloggi, F., Lanuza, J., Andreotti, B. & Clément, E. 2006 Erosion waves: Transverse instabilities and fingering. *Europhys. Lett.* **75**, 825–831.

Mangeney, A., Bouchut, F., Thomas, N., Vilotte, J. P. & Bristeau, M. O. 2007*a* Numerical modeling of self-channeling granular flows and of their levee-channel deposits. *J. Geophys. Res* **112**, F02017.

Mangeney, A., Tsimring, L. S., Volfson, D., Aranson, I. S. & Bouchut, F. 2007*b* Avalanche mobility induced by the presence of an erodible bed and associated entrainment. *Geophys. Res. Lett.* **34**, L22401.

McDonald, R. R. & Anderson, R. S. 1996 Constraints on eolian grain flow dynamics through laboratory experiments on sand slopes. *J. Sediment. Res.* **66**, 642–653.

Melo, F., Joanny, J. F. & Fauve, S. 1989 Fingering instability of spinning drops. *Phys. Rev. Lett.* **63**, 1958–1961.

Moffatt, H. K. 1977 Behaviour of a viscous film on the outer surface of a rotating cylinder. *J. de Mécanique* **16**, 651–673.

Naranjo, J. A., Sparks, R. S. J., Stasiuk, M. V., Moreno, H. & Ablay, G. J. 1992 Morphological, structural and textural variations in the 1988-1990 andesite lava of Lonquimay Volcano, Chile. *Geol. Mag.* **129**, 657–678.

Nye, J. F. 1960 The Response of Glaciers and Ice-Sheets to Seasonal and Climatic Changes. *Proc. Roy. Soc. A* **256**, 559–584.

Oron, A., Davis, S. H. & Bankoff, S. G. 1997 Long-scale evolution of thin liquid films. *Rev. Mod. Phys.* **69**, 931–980.

Pinkerton, H. & Wilson, L. 1994 Factors controlling the lengths of channel-fed lava flows. *Bull. Volcanol.* **56**, 108–120.

Pouliquen, O. 1999 Scaling laws in granular flows down rough inclined planes. *Phys. Fluids* **11**, 542–548.

Pouliquen, O. & Forterre, Y. 2009 A non-local rheology for dense granular flows. *Phil. Trans. Roy. Soc. A* **367**, 5091.

Prasad, S. N., Pal, D. & Römkens, M. J. M. 2000 Wave formation on a shallow layer of flowing grains. *J. Fluid Mech.* **413**, 89–110.

Rajchenbach, J. 2003 Dense, rapid flows of inelastic grains under gravity. *Phys. Rev. Lett.* **90**, 144302.

Rothrock, D. A. 1968 Study of flows down the underside of an inclined plane. PhD thesis, University of Cambridge.

Roy, R. V., Roberts, A. J. & Simpson, M. E. 2002 A lubrication model of coating flows over a curved substrate in space. *J. Fluid Mech.* **454**, 235–261.

Ruschak, K. J. 1985 Coating Flows. *Annu. Rev. Fluid Mech.* **17**, 65–89.

Sakimoto, S. E. H. & Gregg, T. K. P. 2001 Channel flow: Analytic solutions, laboratory experiments, and applications to lava flows. *J. Geophys. Res.* **106**, 8629–8644.

Sakimoto, S. E. H. & Zuber, M. T. 1995 The spreading of variable-viscosity axisymmetric radial gravity currents: applications to the emplacement of Venusian 'pancake' domes. *J. Fluid Mech.* **301**, 65–77.

Savage, S. B. & Hutter, K. 1989 The motion of a finite mass of granular material down a rough incline. *J. Fluid Mech.* **199**, 177–215.

Savage, S. B. & Hutter, K. 1991 The dynamics of avalanches of granular materials from initiation to runout. Part I: Analysis. *Acta Mechanica* **86**, 201–223.

Schwartz, L. W. 1989 Viscous flows down an inclined plane: Instability and finger formation. *Phys. Fluids* **1**, 443.

Shapiro, A. H., Jaffrin, M. Y. & Weinberg, S. L. 1969 Peristaltic pumping with long wavelengths at low Reynolds number. *J. Fluid Mech.* **37**, 799–825.

Shaw, H. R. 1969 Rheology of basalt in the melting range. *J. Petrol.* **10**, 510–535.

Short, M. B., Baygents, J. C., Beck, J. W., Stone, D. A., Toomey III, R. S. & Goldstein, R. E. 2005 Stalactite Growth as a Free-Boundary Problem: A Geometric Law and Its Platonic Ideal. *Phys. Rev. Lett.* **94**, 18501.

Short, M. B., Baygents, J. C. & Goldstein, R. E. 2006 A free-boundary theory for the shape of the ideal dripping icicle. *Phys. Fluids* **18**, 083101.

Silbert, L. E., Ertaş, D., Grest, G. S., Halsey, T. C., Levine, D. & Plimpton, S. J. 2001 Granular flow down an inclined plane: Bagnold scaling and rheology. *Phys. Rev. E* **64**, 051302.

Silvi, N. & Dussan, E. B. V. 1985 On the rewetting of an inclined solid surface by a liquid. *Phys. Fluids* **28**, 5–7.

Spaid, M. A. & Homsy, G. M. 1996 Stability of Newtonian and viscoelastic dynamic contact lines. *Phys. Fluids* **8**, 460–478.

Sparks, R. S. J., Murphy, M. D., Lejeune, A. M., Watts, R. B., Barclay, J. & Young, S. R. 2000 Control on the emplacement of the andesitic lava dome of the Soufriere Hills Volcano, Montserrat by degassing-induced crystallization. *Terra Nova* **12**, 14–20.

Sparks, R. S. J., Pinkerton, H. & Hulme, G. 1976 Classification and formation of lava levees on Mount Etna, Sicily. *Geology* **4**, 269–271.

Stone, H. A. 2005 On lubrication flows in geometries with zero local curvature. *Chem. Eng. Sci.* **60**, 4838–4845.

Takagi, D. & Huppert, H. E. 2007 The effect of confining boundaries on viscous gravity currents. *J. Fluid Mech.* **577**, 495–505.

Takagi, D. & Huppert, H. E. 2008 Viscous gravity currents inside confining channels and fractures. *Phys. Fluids* **20**, 023104.

Takagi, D. & Huppert, H. E. 2010 Flow and instability of thin films on a cylinder and sphere. *J. Fluid Mech.* **647**, 221–238.

Takahashi, T. 1981 Debris Flow. *Annu. Rev. Fluid Mech.* **13**, 57–77.

Tallarico, A. & Dragoni, M. 1999 Viscous Newtonian laminar flow in a rectangular channel: application to Etna lava flows. *Bull. Volcanol.* **61**, 40–47.

Tanner, R. 1970 Some methods for estimating the normal stress functions in viscometric flows. *J. Rheol.* **14**, 483–507.

Taylor, G. I. 1961 Deposition of a viscous fluid on the wall of a tube. *J. Fluid Mech.* **10**, 161–165.

Taylor, G. I. 1962 On scraping viscous fluid from a plane surface. *The Scientific Papers of Sir Geoffrey Ingram Taylor* **4**, 410–413.

Tischer, M., Bursik, M. I. & Pitman, E. B. 2001 Kinematics of Sand Avalanches Using Particle-Image Velocimetry. *J. Sediment. Res.* **71**, 355–364.

Troian, S. M., Herbolzheimer, E., Safran, S. & Joanny, J. F. 1989 Fingering instabilities of driven spreading films. *Europhys. Lett.* **10**, 25–30.

Turnbull, B., McElwaine, J. N. & Ancey, C. 2007 The Kulikovskiy–Sveshnikova–Beghin model of powder snow avalanches: development and application. *J. Geophys. Res.* **112**, F01004.

Vajravelu, K., Sreenadh, S. & Ramesh Babu, V. 2005 Peristaltic transport of a Herschel–Bulkley fluid in an inclined tube. *Int. J. Nonlin. Mech.* **40**, 83–90.

Veretennikov, I., Indeikina, A. & Chang, H. C. 1998 Front dynamics and fingering of a driven contact line. *J. Fluid Mech.* **373**, 81–110.

Wadge, G. 1981 The variation of magma discharge during basaltic eruptions. *J. Volcanol. Geotherm. Res.* **11**, 139–168.

Walker, G. P. L. 1973 Lengths of lava flows. *Phil. Trans. Roy. Soc. A* **274**, 107–116.

Wang, M. W. & Chou, F. C. 2001 Fingering instability and maximum radius at high rotational Bond number. *J. Electrochem. Soc.* **148**, G283–G290.

Wettlaufer, J. S. & Worster, M. G. 1995 Dynamics of premelted films: frost heave in a capillary. *Phys. Rev. E* **51**, 4679–4689.

Wettlaufer, J. S., Worster, M. G., Wilen, L. A. & Dash, J. G. 1996 A theory of premelting dynamics for all power law forces. *Phys. Rev. Lett.* **76**, 3602–3605.

Whitham, G. B. 1974 *Linear end Nonlinear Waves*. Wiley.

Wolfe, E. W., Neal, C. A., Banks, N. G. & Duggan, T. J. 1988 Geologic observations and chronology of eruptive events. *U.S. Geol. Surv. Prof. Pap.* **1463**, 1–97.